Shining Light Through Walls: A Search For Dark Photons

Nathan Woollett

MPhys: Physics with Astrophysics, Astronomy and Cosmology (Lancaster University)

Physics

Department of Physics

Lancaster University

March 2016

A thesis submitted to Lancaster University for the degree of Doctor of Philosophy in the Faculty of Science and Technology

Abstract

The Standard Model of particle physics, although successful, is known to be deficient both theoretically and experimentally. Many proposed extensions to the SM predict the existence of Weakly Interacting Slim Particles (WISPs). In this thesis the construction and results of the CASCADE microwave cavity light shining through a wall experiment will be presented. In addition to CASCADE, this thesis will present a novel realisation of a light shining through a wall experiment using photonic bandgap structures to probe otherwise unreachable regions of the WISP parameter space.

Like all great works, this thesis could not have been completed without the help of numerous people. In this section I would like to take some time to thank those who have helped me over the years.

First of all my wife, Eve. Over the years you have been a great source of motivation, not only with the constant prodding to do some work but also to make you admit that I'm a real scientist. That being said, the fact that this thesis is readable and actually got completed is in no small part due to your help and encouragement.

Where would a PhD student be without his supervisor? Probably in bed. Fortunately Ian was a great supervisor who could put up with my nonsense and kept me on the right track to complete this thesis. As promised, here is your dinosaur!

```
 /@\            \|/
‘-\ \  ______  - 0 -
   \ \/ ‘ /  \  /|\ _
    \_i / \  |\____//
      | |==| |=----/
------hn/--hn/--------
```

Then there are the friends I've made over the last few years. Stephen, Marcin and Anthony: thanks for the fluffies, I think they will now be a permanent feature of my office! May the church of Nathan bring you peace in the years to come. Nick, sorry about the messy desk. Luke, I think you've submitted first *shakes fist*. To all the guys in the Real Ale Society, I'd have gone crazy without such an excellent group of miscreants to go drinking with on a regular basis.

Really when it comes down to it, I've had the greatest time while working on this thesis and all I can do is thank everyone who has been involved in getting me here!

Declaration

This thesis is my own work and no portion of the work referred to in this thesis has been submitted in support of an application for another degree or qualification at this or any other institute of learning.

"Do, or do not. There is no try"

Yoda.

Contents

List of Figures

List of Tables

Commonly Used Acronyms

- SM = Standard Model
- WIMP = Weakly Interacting Massive Particles
- WISP = Weakly Interacting Slim Particle
- HSP = Hidden Sector Photon
- LSW = Light Shining through a Wall
- RF = Radio Frequency
- DM = Dark Matter
- ALP = Axion Like Particle
- TE = Transverse Electric
- TM = Transverse Magnetic

Chapter 1

Introduction

On July the 4th 2012 the ATLAS and CMS collaborations announced that they had found a particle with a rest mass of 126 GeV at CERN's Large Hadron Collider[1, 2]. This announcement marked the point at which the conventional Standard Model(SM) of particle physics was complete, with the discovery of the Higgs boson. Since then the eyes of the scientific community have moved to what is next, with many looking to higher energies to test theories such as supersymmetry. Others however, are now turning their attention to low energies in search of solutions to specific unexplained phenomena such as dark matter or the strong CP problem.

A model that has gained much attention in recent years is the Peccei Quinn axion[3, 4, 5] since it solves the strong CP problem and like the Higgs boson, it is a scalar particle arising from symmetry breaking. In addition to the Peccei Quinn axion there are generic extensions to the SM that introduce additional symmetries associated with vector bosons which are coupled to the SM photon and are free to take any coupling and mass not already excluded experimentally;

these are known by several names such as paraphotons, dark photons or as they will be called in this thesis Hidden Sector Photons(HSPs). The low mass manifestations of this family of particles are collectively known as Weakly-Interacting-Slim-Particles(WISPs) and will be discussed in Chapter 2.

The lack of any observations of WISPs indicate that they must only have faint couplings with the SM particles. This makes them difficult to search for in traditional collider based experiments and therefore dedicated experiments are required to search for their existence. One experimental method called a light shining though a wall(LSW) experiment looks for energy transmission between a source and a detector via a WISP. Understanding how these experiments work relies on a rigorous understanding of electromagnetic theory which is covered in Chapter 3 and a description of how LSW experiments work is covered in Chapter 4.

A LSW experiment can be designed to operate at any frequency range where suitable sources and detectors can be constructed. Particle accelerators use high quality RF cavities and there are commercially available low-noise amplifiers; both of which are suitable for use in a LSW experiment. The CAvity Search for Coupling of A Dark sEctor(CASCADE) experiment used the equipment and expertise at the Cockcroft Institute of Accelerator Science and Technology to carry out an experiment of this type. Its development forms a significant part of this thesis. The CASCADE experiment and its resulting exclusion of a region in the HSP parameter space is described in Chapter 5.

In recent years the development of computer simulations of dielectric lattices has made the field of photonics possible. By exploiting the band structure of lattices it is possible to make photonic cavities which are resonant with quality factors similar to those of superconducting cavities but at frequencies that are difficult to produce using metallic cavities. The PHotonic ARrays for Axions Or HSPs(PHARAOH) experiment is a proposed experiment which was designed as part of this thesis. It uses photonic cavities to facilitate LSW experiments at frequencies and couplings of the HSP that are otherwise inaccessible. A computational study of the performance of these experiments is presented in Chapter 6.

Chapter 2

Weakly Interacting 'Slim' Particles

Weakly Interacting 'Slim' Particles(WISPs)[1] are a category of low mass particles which only have feeble couplings with Standard Model(SM) particles. This chapter starts by summarising the features of the SM and the need for extensions to the SM to make it consistent with observation. The later sections of this chapter discuss specific models of WISPs and how they can satisfy astronomical observations.

2.1 The Standard Model of Particle Physics

The SM is a theory that tries to explain the interactions of the electromagnetic, strong and weak forces in terms of the exchange of gauge bosons between the fundamental particles from which all observed matter is formed. The SM began

[1]WISP can also be an abbreviation for Weakly Interacting Sub-eV Particles but there is no requirement that the mass be below an eV so both can be used.

to take shape when the quark model was developed in 1964[6, 7], although at this point it only contained the up, down and strange quarks. When this quark model was added to the theories of the electroweak interaction and quantum chromodynamics(QCD), the model resembled the modern Standard Model but without an explanation of how to give mass to the gauge bosons. The mechanism that gives rise to the Higgs boson was first proposed in 1964 by a number of scientists[8, 9, 10] to give a gauge-invariant mass acquisition mechanism for bosons and fermions. The SM was subsequently expanded with the charm quark in 1970[11] which was required to explain the suppression of weak interactions that change strangeness by 2 units. Finally, with the addition of the bottom and top quarks in 1973[12] to explain CP violation in kaon decays the SM took the form it has today.

The SM has proven to be a hugely-successful description of elementary particle physics with no experiment have conclusively shown a deviation from its predictions. For example, the strange quark was found in 1968[13, 14] at the SLAC National Accelerator Laboratory confirming the quark model. In 1974 the charm quark was discovered by both the SLAC National Accelerator Laboratory[15] and Brookhaven National Laboratory[16], completing the second generation of quarks. The third generation of quarks, the bottom and the top, were discovered at Fermilab in 1977[17] and 1995[18][19] respectively.

The success of the SM is not limited to the quark sector, it has also predicted the existence of number of bosons that have then been discovered experimentally. The gluon was discovered at DESY in 1979[20] providing strong evidence in support of QCD. The W and Z boson were both announced in 1983 with the mass ratio that was predicted by the SM [21][22]. Finally, the Higgs boson was discovered at CERN in 2012[1][2] within the mass range favoured by the SM.

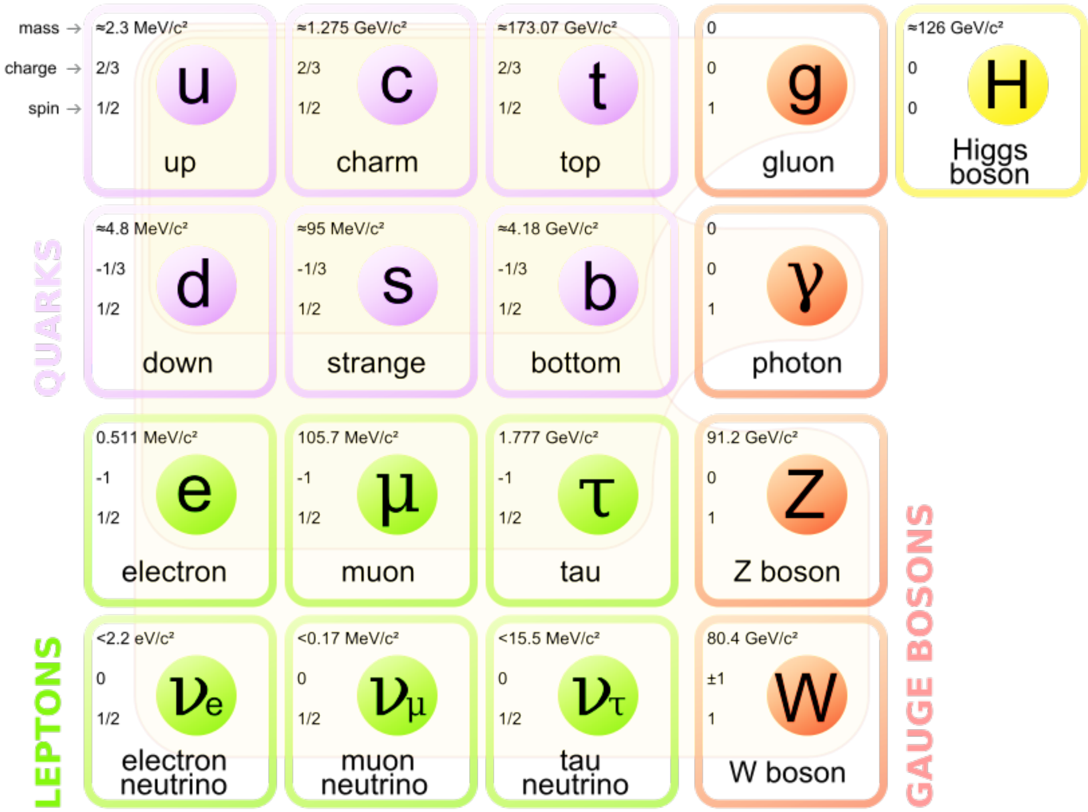

Figure 2.1: A table of particles within the Standard Model. The quarks are in purple; leptons in green; gauge bosons in red and the Higgs in yellow. *Reproduced from* [23]

The fundamental particles that are contained in the SM are commonly shown in a table like the one found in Fig 2.1, in which the particles are grouped by their spin values into fermions(spin 1/2), gauge bosons(spin 1) and the Higgs boson(spin 0). The fermions are further sub categorised into quarks, which interact via the strong force, and leptons, which do not. Quarks come in six 'flavours' and are distinguished by their quantum numbers: charge, weak isospin, charm, strangeness, topness and bottomness. Leptons come in three different flavours: electron, muon and tau lepton, but each has an electrically-charged and neutral version which form a weak isospin doublet.

Gauge bosons mediate the strong, weak and electromagnetic forces by being exchanged between other particles and thereby carrying the force. The photon mediates the electromagnetic force between charged particles. The W and Z bosons couple to weak hypercharge and thereby mediate the weak force between particles carrying weak isospin. Gluons mediate the strong force between quarks. The Higgs boson is a Nambu-Goldstone boson associated with the Higgs field which, through symmetry breaking, gives mass to the W and Z bosons, in addition to the fermions.

2.2 Beyond the Standard Model

Despite the successes of the SM it is possible to find examples of phenomena that it is unable to address, indicating that there is physics beyond the current SM that needs to be explored. For example there is no explanation of the matter dominance over anti-matter in the universe and the SM has no candidate for 'dark matter'.

2.2.1 Dark Matter

As the universe has been surveyed, it has become increasingly clear that it is dominated by 'dark' components. The most recent results from the Planck satellite have provided the best limits to date on the composition of the universe with 4.8%

being matter, 25.8% dark matter(DM)[1] and 69.4% dark energy[2][25]. Currently the SM does not describe these last two phenomena. There are many theories that aim to account for the observations and due to the 'matter-like' nature of DM it has been possible to describe the observations in terms of hypothetical particles.

The earliest evidence for DM came from studies of galactic rotation. These studies were conducted by tracking luminous objects as they rotated around the galactic centre. Naively it would be expected that the rotational velocity would be that of a gravitationally-bound, Keplerian orbit which is proportional to $1/\sqrt{r}$, where r is the radius from the galactic centre. However, when the rotation of galaxies is observed, it was found that the velocity remains approximately constant until the galactic disk becomes too dark to measure.

To produce this velocity distribution required the addition of a halo of non-luminous, *dark* matter around the galaxy with a density $\rho(r) \propto 1/\sqrt{r}$ and a sharp drop off at an unknown radius to maintain the finite mass of a galaxy. When looking at the local neighbourhood of our solar system the DM energy density would be expected to be $0.39\,\mathrm{GeV/cm^3}$[26].

The SM does provide some candidates for DM with the most obvious being the neutrino, however, the majority of DM needs to be non-relativistic to allow galaxy formation which excludes all known species of neutrinos[27]. Since there are no candidates for in the SM, an addition is needed. This addition usually takes the form of either weakly interacting massive particles or weakly interacting

[1]Dark matter refers to particles which interact gravitationally but cannot be observed via electromagnetic observations.

[2]Dark energy is currently the least understood part of the 'dark' sector and will not be dealt with here but a review of the current literature on the topic can be found in the "Review of particle physics" by the Particle Data Group[24].

slim particles which will be discussed in Section 2.3.

2.2.2 Matter Anti-Matter Asymmetry

If the early universe went through baryogenesis as theorised then the majority of SM processes would produce the same number of matter and antimatter particles leading to the annihilation of both species. To produce enough matter for it to become dominant there are three conditions that need to be met[28]:

- The existence of processes that violate conservation of baryon number.
- The existence of processes that violate conservation of C and CP symmetries.
- A deviation from thermal equilibrium.

Baryon number, charge parity and parity symmetry are all broken by at least one process within the SM[29, 30, 31, 32] and the expansion of the early universe breaks the thermal equilibrium satisfying all the conditions. The processes that provide CP violation however, are too small to explain the observed asymmetry therefore processes beyond those in the current SM are needed[33].

One method of increasing the amount of CP violation predicted by the SM is to allow strong interactions to violate CP. There is no mechanism within the framework of the SM that prevents the strong force from violating CP. However, the strongest experimental constraints on strong force CP violation come from measurements of the electric dipole moments of neutrons and these indicate that the CP-violating electric dipole moment is a factor of 10^{-10} smaller that would be expected**??**. This constrains any CP-violation in the strong force to negligible levels with no known mechanism suppressing it[34, 35]. One solution to this problem is to treat the CP violating term as a field. This solution is known as the Peccei-Quinn theory; this will be covered in detail in Section 2.3.1.

2.3 WIMPs and WISPs

The favoured solution to DM over the last few decades has been the addition of Weakly Interacting Massive Particles(WIMPs) to the SM. A WIMP is the generic name for any particle with a mass between 10's of GeV to a few TeV, that only interact through gravity and the weak force.

There are a number of candidates for WIMPs, for example a heavy neutrino would make an ideal candidate, however the relic density[1] would be too small if its mass is greater than half of the mass of the Z boson and masses below this level have been excluded experimentally[36]. The relic density can be increased by adding an additional sterile neutrino but the neutrino would still need to be stable, making a massive neutrino a disfavoured candidate[24].

Supersymmetry provides a number of WIMP candidates but the most favoured are the light supersymmetric particles, since they need to be neutral to be DM this corresponds to the sneutrino or the neutralino. The sneutrino is the spin-zero supersymmetric partner of the neutrino; other than spin and mass they share the same quantum numbers. The neutralino, is a electrically neutral mass eigenstate of the mixing between the Z boson, photon and Higgs superpartners. Current WIMP searches have ruled out normal sneutrinos as a major component of DM[37] leaving neutralinos as the favoured candidate. There are also many

[1]The relic density is the density of particles when the energy of the thermal background of the universe drops below the rest mass of the particle.

non-supersymmetric candidates for WIMPs but the specifics of these theories are beyond the scope of this thesis.

Despite their inert nature, there is the possibility of directly detecting WIMPs. If the abundance of WIMPs distributed throughout our region of the galaxy is sufficient then experiments should be able to detect the fleeting interactions between WIMPs and normal matter inside a detector. When WIMPs interact, they do so by elastically scattering from an atomic nucleus causing a nuclear recoil with energies of around 1 to 100 keV for WIMPs in the expected mass range of 10 GeV to 10 TeV. Through the appropriate choice of a target material such as xenon or germanium, the recoils become detectable through scintillation or if the material has a crystalline structure, phonons[38, 39]. The expected interaction rate is proportional to the WIMP flux and the interaction cross section. Since the WIMP density needs to be $0.39\,\mathrm{GeV/cm^3}$ to explain observations[26], and the velocity relative to the Earth is taken to be 220km/s[40][1], the flux is fixed. The interaction cross section is model dependent, however using the Minimal Supersymmetric Standard Model the interaction rate is up to 1 WIMP interaction $\mathrm{day}^{-1}\,\mathrm{kg}^{-1}$ of material[41]. Therefore, to be sensitive, WIMP experiments need to use a large target and radio-pure materials to minimise interactions in the target volume due to particles other than WIMPs.

An alternative theory to WIMP DM is WISP DM. This is the generic name for any particle which only has feeble interactions with the SM and has a mass less than a few eVs. Searches for these particles concentrate mostly on their interactions with the SM photon. Since the mass is so small, collider-based ex-

[1]The velocity is assumed to be the rotational velocity of Earth around the galactic centre, effectively making DM static with respect to the galactic centre.

periments are unsuitable to look for them using a missing mass type search to indirectly detect them[42]. This leaves much of the WISP parameter space open to be searched by dedicated small-scale experiments. Two of these particles, the Hidden Sector Photon(HSP) and the axion, have come under great interest recently as they are predicted by well-motivated extensions to the SM.

2.3.1 The Axion

The axion is a neutral scalar particle that arises from the Peccei-Quinn mechanism introduced in 1977 to solve the strong CP problem[3]. To understand the strong CP problem, the starting point is to note that the quantum chromodynamics(QCD) Lagrangian contains a CP-violating term,

$$\mathcal{L} = \frac{\alpha_s}{4\pi}\theta \mathrm{tr} G_{\mu\nu}\tilde{G}^{\mu\nu} \tag{2.1}$$

where G is the gluonic field strength tensor, $\tilde{G}$ denotes the dual field tensor, 'tr' denotes the colour trace of the gluonic fields, α_s is the strong coupling constant and θ is the CP violating term which currently needs to be determined experimentally. The indices μ and ν take the values 0, 1, 2 or 3 and repeated indices are summed over. One of the strongest bounds on θ is obtained by measuring the electric dipole moment of the neutron. The size of the neutron electric dipole moment can be calculated to be

$$|d_n| = \frac{e}{m_n}\left(\frac{m_q}{m_n}\right)|\bar{\theta}| \ = 10^{-16}|\bar{\theta}| e\,\mathrm{cm}, \tag{2.2}$$

where $m_{n,q}$ are the neutron and light quark masses respectively, e is electric charge and

$$\bar{\theta} \equiv \theta + arg\ detM, \tag{2.3}$$

where M is the quark mass mixing matrix, θ is the contribution from gluon coupling as in Eq 2.1 and $\bar{\theta}$ is the effective physical CP-violating parameter in the SM[43]. The current upper bound on $|d_n|$ is $2.9 \times 10^{-26} e\,\mathrm{cm}$[34] which consequently puts an upper limit of $|\bar{\theta}| = 10^{-10}$. This upper limit is unnaturally small for a dimensionless parameter that is made up from two unrelated parameters. The lack of an explanation for this observation is referred to as the 'strong CP problem'.

The axion is a result of introducing the Peccei Quinn mechanism to solve the strong CP problem. The mechanism works by 'promoting' $\bar{\theta}$ to be a field which is known as the axion field. The symmetry is then spontaneously broken, allowing the value of θ to relax to a low value. This provides an explanation for the observed value of $\bar{\theta}$, solving the strong CP problem and producing a pseudo Nambu Goldstone boson called the axion.

The dynamics of a system are given by minimising the 'action' $S = \int \mathcal{L} dt$ where $\mathcal{L}$ is the Lagrangian density. The axion has a coupling to the SM photon which is often exploited in experimental searches for which the Lagrangian density is

$$\mathcal{L} = \frac{G_{A\gamma\gamma}}{4} F_{\mu\nu} \tilde{F}^{\mu\nu} \phi_A = -G_{A\gamma\gamma} (\mathbf{E} \cdot \mathbf{B}) \phi_{\mathbf{A}}, \tag{2.4}$$

where ϕ_A is the axion field, $G_{A\gamma\gamma}$ is the axion-photon coupling, F is the electromagnetic field-strength tensor and $\tilde{F}$ is its dual tensor. For the Peccei Quinn axion there is a model-dependent relationship between the coupling constant and the mass of the axion which is given by

$$G_{A\gamma\gamma} = \frac{\alpha}{2\pi}\left(\eta - \frac{2}{3}\frac{4+z}{1+z}\right)\frac{1+z}{z^{1/2}}\frac{m_a}{m_\pi f_\pi}, \tag{2.5}$$

where $z = m_u/m_d$, f_π is the pion decay constant and η is a model dependent parameter which produces the yellow band shown on the axion parameter space in Fig 2.2.

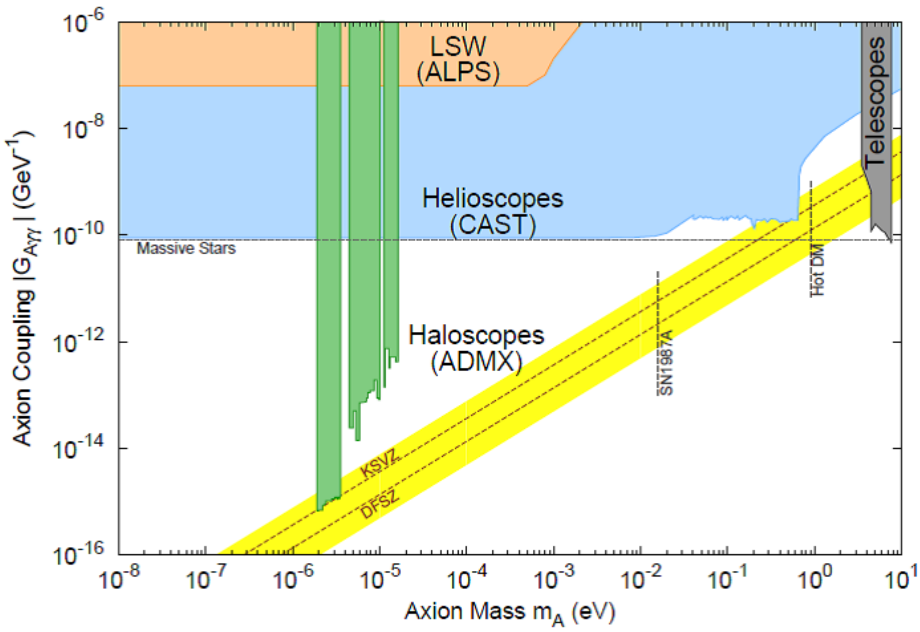

Figure 2.2: The parameter space for the axion. Experimental exclusions from ALPS is in orange, CAST in blue and ADMX in green. The prefered region for the Peccei-Quinn axion is shown as a yellow band with the KSVZ[44] and DFSZ[45] models being highlighted with dashed lines. The remaining white space is parameter space which is unconstrained. *Reproduced from* [24].

A coupling to the SM photon is typical of a pseudoscalar particle and this mechanism can therefore be generalised to other quantum numbers such as family and lepton number to make the familon and Majoron particles[46, 47]. In the most general case these particles are referred to as axion-like-particles(ALPs).

Since there is no general link between the mass of the ALP and the coupling of the ALP to photons, the ALP can be found anywhere in the parameter space. In addition since the photon coupling is not guaranteed to be non-zero, a negative search result does not exclude the existence of all ALPs with that mass.

2.3.2 The Hidden Sector Photon

The symmetry breaking of the axion field leads to the existence of the axion. However many additions to the SM predict additional U(1) gauge symmetries each with their own associated gauge boson. These bosons are referred to as Hidden Sector Photons(HSPs), Paraphotons or Dark Photons[24]. In this thesis they will be referred to exclusively as HSPs.

HSPs are well-motivated particles as the additional U(1) symmetries from which they arise are generic features that are produced for example by string compactification. If these symmetries remain unbroken down to low energies, their dominant interaction is with the photon[48]. This interaction takes the form of kinetic mixing in a process analogous to neutrino flavour mixing. The Lagrangian for the mixing takes the form

$$\mathcal{L} = -\frac{1}{4}F^{\mu\nu}F_{\mu\nu} - \frac{1}{4}B^{\mu\nu}B_{\mu\nu} - \frac{1}{2}\chi F^{\mu\nu}B_{\mu\nu} - \frac{1}{2}m_{\gamma'}^2 B_\mu B^\mu, \tag{2.6}$$

where χ is the mixing parameter, $m_{\gamma'}$ is the HSP mass, $F^{\mu\nu}$ is the SM electromagnetic field tensor, $B^{\mu\nu}$ is the HSP field tensor and B is the HSP field. The size of χ is required to be small to explain non-observation and some models predict a range of values for χ, for example string compactification models predict χ to be between 10^{-12} and 10^{-3}[48]. Current exclusions and regions favoured by models are shown on the HSP parameter space shown in Fig 2.3.

The HSP may be massless like the SM photon, however it can gain mass through the standard Higgs mechanism or through the Stueckelberg mechanism[49].

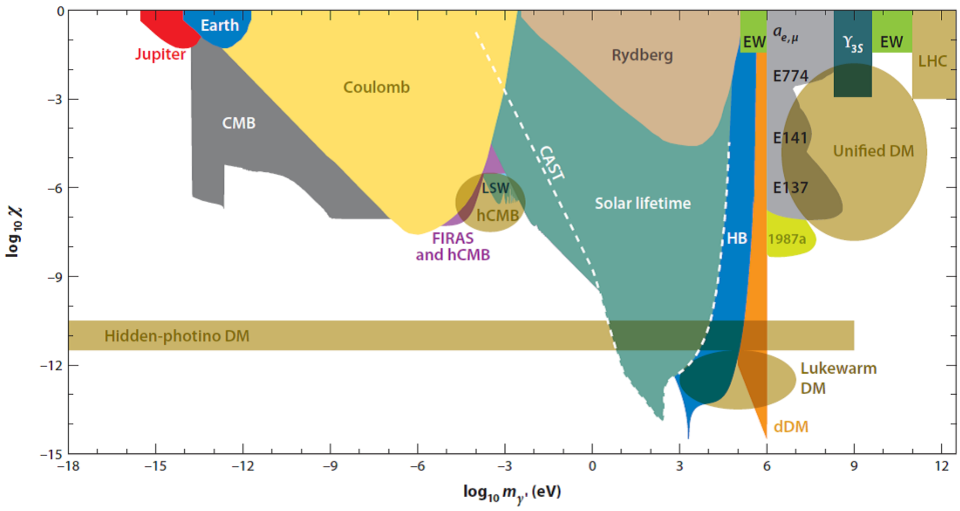

Figure 2.3: The parameter space of the HSP showing both astrophysical and experimental limits. The light orange bands indicate theoretically-interesting areas. *Reproduced from* [48]

.

2.3.3 Other WISPs

The additional symmetries that are responsible for both the axion and HSP are not the only possibilities. In fact string compactifications generally also predict additional scalar particles. These scalar fields are also often used in cosmology to explain dark energy as the accelerated expansion of the universe can be explained by the presence of a spatially homogeneous scalar field rolling down a flat potential[50].

The strength and range of interactions between light scalar fields and ordinary matter are limited through the non-observation of a fifth force[51]. From this constraint comes the theory of chameleon fields whose effective mass is a function of the local energy density of space[52]. This leads to some interesting properties, where in environments with a high energy density e.g. on Earth, the chameleon field can mediate forces over a range of 1 mm, however when in a low energy density e.g. intergalactic space, the range can increase to thousands of parsecs. Since these particles have no set mass or coupling strength they are very hard to detect.

Mini-charged particles are hypothetical particles that are electrically charged, but with only a fraction of the charge of the electron. Indications of the existence of mini-charged particles can be probed using a number of techniques including direct searches in a Light Shining through a Wall(LSW) experiment and testing for deviations from Coulomb's law[53, 54].

2.4 Experimental Searches

There are currently a number of experiments around the world looking for HSPs or axions and they can be roughly broken down into two categories: those that are assuming an astrophysical origin of the particles and those that have a laboratory-based source of particles. If an experiment with an astrophysical source is looking for DM particles they benefit from a high energy density which would be difficult to reach with a laboratory-based source. However, a laboratory-based source provides control over the signal and so greater understanding of the systematic uncertainties is achievable allowing for sensitive probes of the parameter space.

2.4.1 Astrophysical Source Experiments

When looking for an astrophysical source of WISPs there are two obvious choices: the DM background of the galaxy and WISP production in the sun. Both have their own benefits and drawbacks.

Experiments that use the galactic DM background are often known as haloscopes. They benefit from a relatively high power density of $450\,\mathrm{MeV\,cm^{-3}}$[24]. However, DM rotation rates are poorly understood so the particle flux through the experiment has a large uncertainty. In addition, the distribution of DM within the galaxy is not known, therefore both homogeneous and clumpy distributions are equally possible. This means any assumptions of the local DM environment also have large uncertainties[55].

Some experiments try and get around the challenges posed by a DM source by using the intense photon source of the sun as a signal source and are known as helioscopes. They work by looking for axions that were produced through the electron-axion coupling and generally probe axion masses corresponding to x-ray frequencies. Helioscopes benefit from a relatively strong understanding of the processes within the sun and the high particle flux that is generated. The challenges imposed by a helioscope are more practical in nature, when the solar axions are converted to photons they do so at x-ray frequencies meaning construction of a resonating cavity is a non-trivial task. In addition, since the sun is a directional source, the detector equipment needs to be manoeuvred to track the sun for optimum performance which poses an engineering challenge.

Both helioscopes and haloscopes suffer from having no set mass range for an expected signal which means that discriminating between a genuine signal and background noise can be difficult.

The dominant method of building an experiment is to build a structure which is resonant at the frequency corresponding to the mass range to be probed and have a method of recording the power deposited within the structure. The motivation for the use of a resonant structure will be discussed in Chapter 4.

The ADMX helioscope experiment[56] takes advantage of a highly-resonant microwave cavity to listen for DM axions converting to photons. It has dielectric rods in the cavity that can be moved in order to shift the resonant frequency, allowing for a range 550 to 810 MHz to be scanned[57, 58].

Another experiment which is being developed at DESY is called FUNK it uses a dish antenna as a detector[59]. The advantage of using a shielded dish antenna is that it will focus photons of all frequencies to a single spot which will allow the experiment to be sensitive to any frequency that the detector is sensitive to, whereas resonators only operate in a finite bandwidth.

The first axion helioscope was the Tokyo Axion Helioscope[60], and it was followed by CAST at CERN[61]. The successor to CAST was proposed in 2014 and is currently known as IAXO[62]. The heiloscopes themselves consist of a strong magnetic field, mounted so the field is perpendicular to the propagation direction of solar axions, and a sensitive x-ray detector. If the magnetic field is disabled, it is possible to use axion helioscopes to measure signals from HSPs.

2.4.2 Laboratory Based Experiments

Many of the limitations of using galactic and solar WISP sources can be overcome by using a laboratory-based source and detector as they allow greater control over systematic uncertainties and false signals. There are two main forms of laboratory WISP searches. The first creates a highly-polarised resonating EM mode. When a WISP is produced within the resonating mode it will affect the polarisation of the mode. The second method, known as a LSW experiment, has two resonant cavities: one powered to act as an emitter and the second shielded to act as a detector. Since LSW experiments have a specific target energy for the WISP, they allow for an even greater signal discrimination. The method behind LSW experiments is described in more detail in Chapter 4.

ALPs was one of the first LSW experiments to produce significant results; it consists of an infra-red laser cavity and an identical but unpowered cavity that acts as a detector. By operating the laser at its harmonics the ALPs collaboration have been able to make many measurements over a wide mass range. An upgrade for ALPs is in development at the time of writing which includes a longer cavity to allow more time for conversion and the ability to apply a magnetic field to the line to facilitate an axion search[63].

In addition to LSW experiments operating at near optical frequencies, it is possible to construct a LSW at any frequency where suitable containment can be achieved. One such frequency range at which suitable containment structures are routinely achieved is the microwave range. Particle accelerators use metallic cavities to support high fields that are used in the acceleration of particles. These cavities can be re-purposed as sources and detectors for HSP and axion searches. Since the technology to produce these cavities are commonplace in accelerator institutes a number have planned LSW experiments. To date the only microwave LSW to publish results is the CROWS experiment at CERN[64], however experiments are currently planned at The University of Western Australia[65] and Yale

University[66]. The CASCADE LSW experiment is in active development at The Cockcroft Institute of Accelerator Science and Technology; development and the results of the first phase of this experiment are covered in Chapter 5.

Chapter 3

Electromagnetic Theory

The experiments at the core of this thesis depend on a strong understanding of electromagnetism and therefore the first part of this chapter will recap the main points of a standard treatment of electromagnetism as can be found in many textbooks such as Classical Electrodynamics by JD Jackson[67]. The second part of this section will introduce the basics of photonic structures which will be used in Chapter 6. The approach will be based on Molding The Flow of Light by Joannopoulos, Johnson, Winn and Meade[68].

3.1 Maxwell's Equations[1]

Initially electromagnetism was described using Faraday's law, Ampere's law, Gauss's law and Gauss's law. Maxwell's step of logic was to introduce time varying fields which allowed him to combine these separate laws into a single set of equations. These equations take the form

[1]This section follows Chapter 6 in [67]

$$\nabla \cdot \mathbf{B} = 0 \tag{3.1a}$$

$$\nabla \cdot \mathbf{D} = \rho \tag{3.1b}$$

$$\nabla \times \mathbf{E} + \frac{\partial \mathbf{B}}{\partial t} = 0 \tag{3.1c}$$

$$\nabla \times \mathbf{H} = \mathbf{J} + \frac{\partial \mathbf{D}}{\partial t}. \tag{3.1d}$$

where $\mathbf{E}$, $\mathbf{H}$ and $\mathbf{D}$ are the electric, magnetic fields and the displacement field and $\mathbf{B}$ is the magnetic flux density.

For a uniform, isotropic linear medium the fields are related though the constitutive relations,

$$\mathbf{D} = \varepsilon_0 \varepsilon \mathbf{E} \tag{3.2a}$$

$$\mathbf{B} = \mu_0 \mu \mathbf{H}, \tag{3.2b}$$

where ε_0 is the vacuum permittivity, μ_0 is the vacuum permeability, ε and μ are the relative permittivity and permeability. ε and μ are complex functions of the frequency ω however when these functions are real and positive the medium is lossless. By choosing the appropriate values of ε and μ any media can described, even those that are not found naturally. Assuming solutions are harmonic with a time dependence of $e^{-i\omega t}$ and have no source, it is possible to build any solution from Fourier superposition of these harmonics. The equations for the amplitudes $\mathbf{E}(\omega, \mathbf{r})$ and $\mathbf{B}(\omega, \mathbf{r})$ where $\mathbf{r}$ is the position, become

$$\nabla \cdot \mathbf{B} = 0 \tag{3.3a}$$

$$\nabla \cdot \mathbf{D} = 0 \tag{3.3b}$$

$$\nabla \times \mathbf{E} = i\omega\mathbf{B} \tag{3.3c}$$

$$\nabla \times \mathbf{B} = -i\varepsilon\mu\omega\mathbf{E}. \tag{3.3d}$$

The free-space macroscopic Maxwell's equations were previously stated in Eq 3.1 but they can also be used to describe light propagating inside of a material such as dielectric materials which will be used in Section 3.3. When describing dielectric materials without a source of electric or magnetic field, both ρ and $\mathbf{J}$ can be set to zero. In addition, since most dielectric materials are non-magnetic $\mu = 1$. This simplifies Eq 3.1 to

$$\nabla \cdot \mathbf{H} = 0 \tag{3.4a}$$

$$\nabla \cdot (\varepsilon\mathbf{E}) = 0 \tag{3.4b}$$

$$\nabla \times \mathbf{E} + \mu_0 \frac{\partial \mathbf{H}}{\partial t} = 0 \tag{3.4c}$$

$$\nabla \times \mathbf{H} - \varepsilon_0\varepsilon \frac{\partial \mathbf{E}}{\partial t} = 0. \tag{3.4d}$$

3.2 Maxwell's Equations In A Cavity [1]

To form a resonator in the radio frequency regime metallic structures with either vacuum or rarefied gases inside a cavity are typically used. For this section all

[1] This section follows Chapter 8 in [67]

materials will be assumed to be lossless and all metals will be approximated as perfect conductors. Cavities are typically cylindrical as sharp features can lead to the concentration of electric field on the surface, and this leads to 'break down' when run at high powers. A long cavity without end caps is essentially a waveguide so it is a good place to start with understanding electromagnetic waves inside these structures.

Starting with Maxwell's equations for a time-varying electric field, Eq 3.3, by choosing the appropriate ε and μ any lossless medium in the cavities can be described. It can be shown that $\mathbf{E}$ and $\mathbf{B}$ satisfy

$$\left(\nabla^2 + \mu\varepsilon\omega^2\right)\Psi = 0. \tag{3.5}$$

where Ψ represents either the $\mathbf{E}$ or $\mathbf{B}$ field. Because of the cylindrical geometry it is helpful to separate out the variation along the major axis which is also the direction of wave propagation, z, giving Eq 3.5 the form

$$\mathbf{E}(\mathbf{r}, t) = \mathbf{E}(x, y)e^{\pm ikz - i\omega t} \tag{3.6a}$$

$$\mathbf{B}(\mathbf{r}, t) = \mathbf{B}(x, y)e^{\pm ikz - i\omega t}. \tag{3.6b}$$

The wave number k can be real or complex. With this z dependence the wave equation can be reduced to a two dimensional form

$$\left[\nabla_t^2 + (\mu\varepsilon\omega^2 - k^2)\right]\Psi = 0, \tag{3.7}$$

where ∇_t^2 is the transverse part of the Laplacian operator. It is useful at this stage to separate the fields into components parallel to and transverse to the z axis, $\mathbf{E} = \mathbf{E}_t + E_z\hat{\mathbf{z}}$. Assuming propagation in the positive z direction and the non-vanishing of either E_z or B_z, the transverse fields are given by

$$\mathbf{E}_t = \frac{i}{\mu\varepsilon\omega^2 - k^2}[k\nabla_t E_z - \omega\hat{\mathbf{z}} \times \nabla_t B_z] \tag{3.8a}$$
$$\mathbf{B}_t = \frac{i}{\mu\varepsilon\omega^2 - k^2}[k\nabla_t B_z - \omega\hat{\mathbf{z}} \times \nabla_t E_z] \quad . \tag{3.8b}$$

This gives rise to two broad categories of waves: transverse magnetic(TM) waves whose $\mathbf{B}$ component in the direction of propagation equals zero, and transverse electric(TE) waves whose $\mathbf{E}$ component in the direction of propagation is zero[1]. The transverse components of the electric and magnetic fields for both TE and TM waves are related to one another by

$$\mathbf{H}_t = \frac{\pm 1}{Z}\hat{\mathbf{z}} \times \mathbf{E}_t, \tag{3.9}$$

where Z is the wave impedance and is given by

$$Z = \begin{cases} \dfrac{k}{\varepsilon\omega} = \dfrac{k}{k_0}\sqrt{\dfrac{\mu}{\varepsilon}} & \text{(TM)} \\ \dfrac{\mu\omega}{k} = \dfrac{k}{k_0}\sqrt{\dfrac{\mu}{\varepsilon}} & \text{(TE)} \end{cases}, \tag{3.10}$$

where $k_0 = \omega\sqrt{\mu\varepsilon}$. The plus minus sign in 3.9 is determined by the sign of the z dependence.

In general a resonant cavity can be of any shape, however they can be easily

[1]There are also TEM waves which only have transverse components but they will not be discussed here.

modelled as a section of cylindrical waveguide with two plates sealing its ends. The z dependence of the field takes the form of a standing wave because of reflections at the end surfaces.

$$\Psi = \mathcal{C}_1 \sin\left(\frac{p\pi z}{d}\right) + \mathcal{C}_2 \cos\left(\frac{p\pi z}{d}\right), \tag{3.11}$$

where Ψ can represent either the $\mathbf{E}$ or $\mathbf{B}$ field, $\mathcal{C}_{1,2}$ are arbitrary amplitudes, p is the number of anti-nodes in the z direction and the boundary surfaces are at $z = 0$ and $z = d$. TM fields require that $E_z = 0$ at $z = 0$ and $z = d$ so

$$E_z = \Psi(x, y) \cos\left(\frac{p\pi z}{d}\right) \qquad (p = 0, 1, 2, ...), \tag{3.12}$$

For TE fields the same is true for H_z, so

$$H_z = \Psi(x, y) \sin\left(\frac{p\pi z}{d}\right) \qquad (p = 1, 2, 3, ...), \tag{3.13}$$

For the transverse fields to satisfy the boundary conditions, TM fields will be of the form

$$\mathbf{E}_t = -\frac{p\pi}{d\gamma^2} \sin\left(\frac{p\pi z}{d}\right) \nabla_t \Psi \tag{3.14a}$$

$$\mathbf{H}_t = \frac{i\varepsilon\omega}{\gamma^2} \cos\left(\frac{p\pi z}{d}\right) \hat{\mathbf{z}} \times \nabla_t \Psi, \tag{3.14b}$$

and TE fields,

$$\mathbf{E}_t = -\frac{i\omega\mu}{\gamma^2}\sin\left(\frac{p\pi z}{d}\right)\hat{\mathbf{z}}\times\nabla_t\Psi \tag{3.15a}$$

$$\mathbf{H}_t = \frac{p\pi}{d\gamma^2}\cos\left(\frac{p\pi z}{d}\right)\nabla_t\Psi, \tag{3.15b}$$

where γ^2 is the eigenvalue associated with a specific solution to Eq 3.7 and takes the form,

$$\gamma^2 = \mu\varepsilon\omega^2 - \left(\frac{p\pi}{d}\right)^2. \tag{3.16}$$

For each value of p the eigenvalue γ^2 determines an eigenfrequency

$$\omega_p^2 = \frac{1}{\mu\varepsilon}\left[\gamma^2 + \left(\frac{p\pi}{d}\right)^2\right], \tag{3.17}$$

and the corresponding field of the resonant mode. By choosing the dimensions of the cavity carefully the frequency of the resonant modes can be well separated, which is required for stable operation.

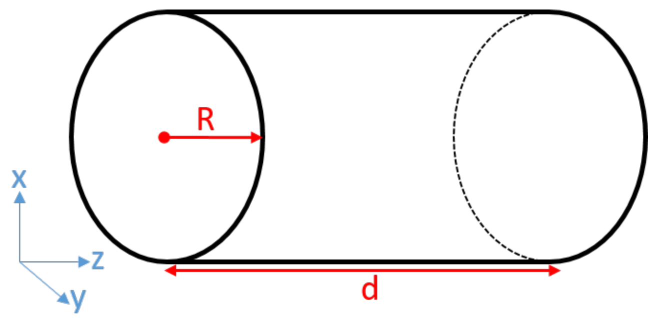

Figure 3.1: A cylindrical cavity, the radius and length are chosen for its resonant properties. If extended in the z direction it becomes a waveguide.

For a cylindrical cavity like the one shown in Fig 3.1 with a inner radius of R

and length of d, the transverse wave equation for E_z with the boundary condition $E_z = 0$ at $\rho = R$ has the TM mode solution:

$$E_z(\rho, \phi) = E_0 H_m(\gamma_{mn}\rho) e^{\pm im\phi}, \tag{3.18}$$

where

$$\gamma_{mn} = \frac{x_{mn}}{R}, \tag{3.19}$$

where x_{mn} is the nth root of the Bessel function.

This gives resonant frequencies of

$$\omega_{mnp} = \frac{1}{\sqrt{\mu\varepsilon}} \sqrt{\frac{x_{mn}^2}{R^2} + \frac{p^2\pi^2}{d^2}}. \tag{3.20}$$

The numbers m, n and p are the mode numbers and can be used to describe the general profile of a field. The first 3 modes for m and n are shown in Fig 3.2.

For TE modes Eq 3.18 is still true but the boundary condition changes to $H_z[\partial\Psi/\partial\rho|_R = 0]$. The effect of this is that γ_{mn} becomes,

$$\gamma_{mn} = \frac{x'_{mn}}{R}, \tag{3.21}$$

where x'_{mn} is the nth root of the derivative of the Bessel function, $J'_m(x) = 0$.

As in Eq 3.20, the resonant frequency corresponding to each mode is given by

$$\omega_{mnp} = \frac{1}{\sqrt{\mu\varepsilon}} \sqrt{\frac{x'^2_{mn}}{R^2} + \frac{p^2\pi^2}{d^2}}. \tag{3.22}$$

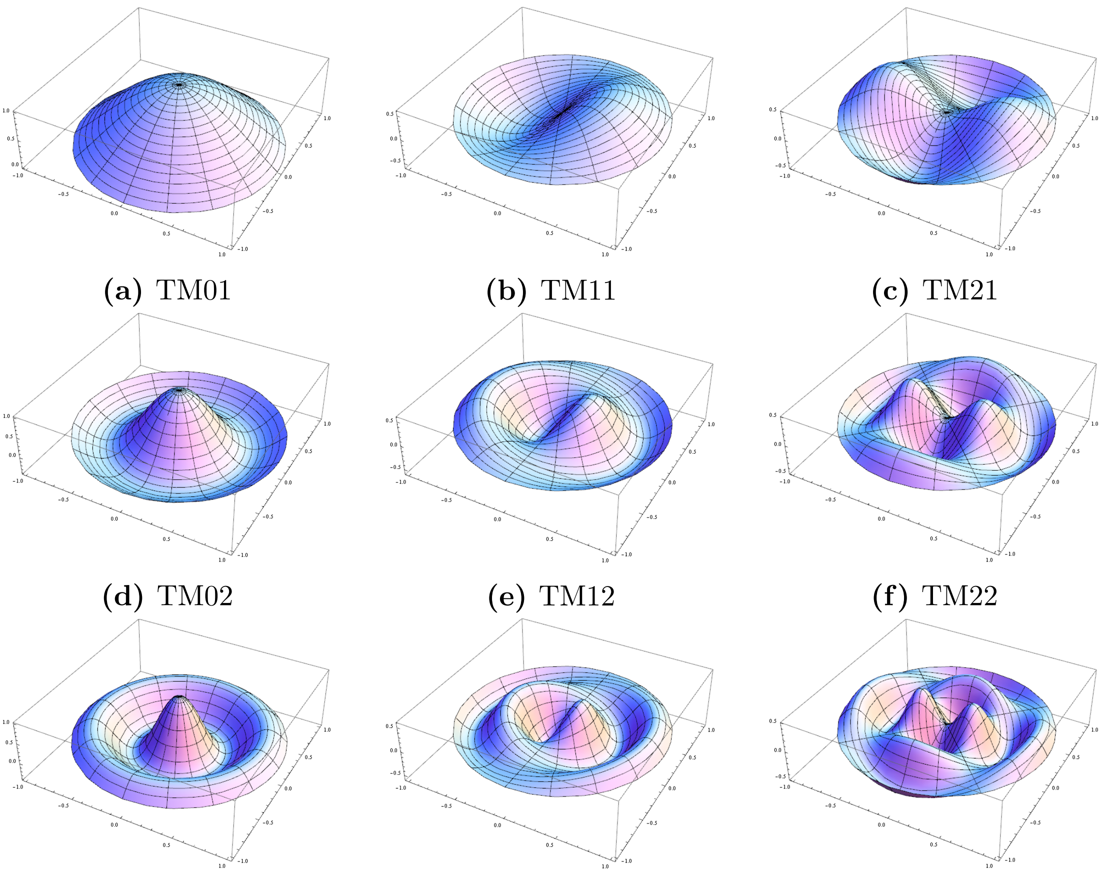

(a) TM01 **(b)** TM11 **(c)** TM21

(d) TM02 **(e)** TM12 **(f)** TM22

(g) TM03 **(h)** TM13 **(i)** TM23

Figure 3.2: Mode profiles for E_z in a cylindrical cavity. In all modes $p = 0$ so variations in the propagation direction are ignored.

3.2.1 Power in a Cavity

Up until now the mode frequencies for a cavity have been treated as delta functions, this means that to excite the resonance the signal would need to be injected with exactly the resonant frequency. In reality the analytically derived frequency is broadened. An important source of the broadening of the resonant peak is the resistive losses in the cavity walls. The broadening effect of the losses within the cavity for a resonance is measured as the Q-factor of the cavity. This is defined as 2π times the ratio of the time-averaged energy stored in the cavity U to the energy lost per cycle ΔU.

$$Q = \omega_0 \frac{U}{\Delta U}, \tag{3.23}$$

where ω_0 is the resonant frequency. This means that the energy in the cavity as a function of time is

$$\frac{dU}{dt} = -\frac{\omega_0}{Q} U, \tag{3.24}$$

where the solution takes the form of

$$U(t) = U_0 e^{-\omega_0 t/Q}. \tag{3.25}$$

The initial energy stored in the cavity, U_0, decays exponentially with the decay constant inversely proportional to the Q of the cavity. This implies that the oscillation of the fields in the cavity are damped in the form[1],

[1]The E field will be used for this calculation but the arguments can equally be applied to the B field.

$$E(t) = E_0 e^{-\omega_0 t/(2Q)} e^{-it(\omega_0+\Delta\omega)}, \tag{3.26}$$

where $\Delta\omega$ allows for an offset from the resonant frequency. This kind of oscillation doesn't consist of a single frequency but is a superposition of frequencies around the resonance and therefore,

$$E(t) = \frac{1}{\sqrt{2\pi}} \int_{-\infty}^{\infty} E(\omega) e^{-i\omega t} d\omega, \tag{3.27}$$

where

$$E(\omega) = \frac{1}{\sqrt{2\pi}} \int_{0}^{\infty} E_0 e^{-\omega_0 t/(2Q)} e^{-it(\omega_0+\Delta\omega)} dt. \tag{3.28}$$

This enables us to calculate the frequency distribution of the energy in the cavity which has the form,

$$|E(\omega)|^2 \propto \frac{1}{(\omega - \omega_0 - \Delta\omega)^2 + (\omega_0/2Q)^2}. \tag{3.29}$$

The characteristic shape produced has its full width at half of the maximum value equal to ω_0/Q. If a constant input voltage with a fixed amplitude is applied to a cavity, the stored energy as a function of frequency will follow the resonance curve in the region close to a resonance.

The Q of a cavity can be calculated by time-averaging the energy in the cavity and then determining the power loss in the walls. The method of calculating the wall losses is similar to the calculation of attenuation in cylindrical waveguides. For the mode λ, p, in a cavity, the energy stored is

$$U = \frac{d}{4}\left\{\begin{matrix}\varepsilon \\ \\ \mu\end{matrix}\right\}\left[1+\left(\frac{p\pi}{\gamma_\lambda d}\right)^2\right]\int_A |\Psi|^2 da, \tag{3.30}$$

where A is the cross-sectional area, TE modes correspond to μ and TM mode correspond to ε. For TM modes where $p = 0$ the result needs to be multiplied by a factor of 2.

It has previously been stated that the Q-factor losses are caused by the resistance of the cavity walls. These losses can be written in an intuitive manner that reflects the physical interpretation[1],

$$Q = \frac{\mu}{\mu_c}\left(\frac{V}{S\delta}\right) \times G, \tag{3.31}$$

where V is the cavity volume, S is its surface area and G is a geometric factor. This can be thought of a the ratio of the volume occupied by the cavity fields and the volume that the field penetrates into the cavity walls and generate losses.

3.3 Photonic Structures

As will be seen in Chapter 6, photonic structures may be used to perform novel HSP searches. In this section the properties of these structures will be explained.

3.3.1 Formalism of Photonic Structures[2]

Photonic structures are crystal-like structures where the periodicity of the structure and properties of the materials are used to control the flow of light. Even

[1]For a calculation of these losses see Appendix A.
[2]This section follows Chapter 1 in [68]

though much of the terminology of photonic structures is borrowed from solid state physics, the structures themselves can be macroscopic in nature with the characteristic scale or lattice constant being set by the wavelength of light that the structure manipulates. With a suitably large structure the propagation of light through the lattice is analogous to the propagation of electrons through a crystal and therefore it is possible to use similar analytical techniques. One such technique is to represent the propagating light/electron as a Bloch wave or when localised, a Bloch state.

The starting point for understanding photonics is Maxwell's equations inside dielectric materials, Eq 3.4. Since Maxwell's Equations are linear it is possible to separate the temporal and spatial dependences by breaking down the field into a set of harmonic modes. These harmonic modes can be summed up with appropriate intensities to produce any desired solution. The harmonic modes are constructed from a spatial profile multiplied by a complex exponential, $\mathbf{H}(\mathbf{r},t) = \mathbf{H}(\mathbf{r})e^{-i\omega t}$ and $\mathbf{E}(\mathbf{r},t) = \mathbf{E}(\mathbf{r})e^{-i\omega t}$, where the physical fields correspond to the real component. Substituting these into Eq 3.4a and Eq 3.4b yields the divergence conditions,

$$\nabla \cdot \mathbf{H}(\mathbf{r}) = 0 \tag{3.32a}$$

$$\nabla \cdot [\varepsilon(\mathbf{r})\mathbf{E}(\mathbf{r})] = 0. \tag{3.32b}$$

By separating the variables in Eq 3.4c and Eq 3.4d in the same way as was done for Eq 3.4a and Eq 3.4b, purely spatial curl equations are otained,

$$\nabla \times \mathbf{E}(\mathbf{r}) - i\omega\mu_0\mathbf{H}(\mathbf{r}) = 0 \tag{3.33a}$$

$$\nabla \times \mathbf{H}(\mathbf{r}) - i\omega\varepsilon_0\varepsilon(\mathbf{r})\mathbf{E}(\mathbf{r}) = 0. \tag{3.33b}$$

Dividing Eq 3.33b by $\varepsilon(\mathbf{r})$ and then taking the curl allows us to use Eq 3.33a to decouple the field equations. The constants ε_0 and μ_0 can be absorbed into a factor of the speed of light, c, yielding the master equation of photonics

$$\nabla \times \left(\frac{1}{\varepsilon(\mathbf{r})}\nabla \times \mathbf{H}(\mathbf{r})\right) = \left(\frac{\omega}{c}\right)^2 \mathbf{H}(\mathbf{r}). \tag{3.34}$$

By using the the master equation with the divergence equations Eq 3.32 it is possible to calculate the magnetic field for any given structure. This is done by taking a function which describes the permittivity of the structure, $\varepsilon(\mathbf{r})$ and then solving Eq 3.34 to find the modes of $\mathbf{H}(\mathbf{r})$ and their respective frequencies. $\mathbf{E}(\mathbf{r})$ can then be recovered by using Eq 3.33b.

It can be helpful to think of some electromagnetic problems in terms of an eigenvalue problem. This can be done by taking the master equation, Eq 3.34, and treating the left side as an operator $\hat{\Theta}$, acting on $\mathbf{H}(\mathbf{r})$:

$$\hat{\Theta}\mathbf{H}(\mathbf{r}) = \left(\frac{\omega}{c}\right)^2 \mathbf{H}(\mathbf{r}) \tag{3.35a}$$

$$\hat{\Theta}\mathbf{H}(\mathbf{r}) = \nabla \times \left(\frac{1}{\varepsilon(\mathbf{r})}\nabla \times \mathbf{H}(\mathbf{r})\right). \tag{3.35b}$$

It is important to note that the operator $\hat{\Theta}$ is linear. This means if $\mathbf{H}_1(\mathbf{r})$ and $\mathbf{H}_2(\mathbf{r})$ are both solutions of Eq 3.35 with the same frequency ω, then so is $a\mathbf{H}_1(\mathbf{r}) + b\mathbf{H}_2(\mathbf{r})$ where a and b are constants, allowing a convenient way of representing degenerate harmonic modes.

3.3.2 Electromagnetic Energy in a Dielectric Medium[1]

When looking at an electromagnetic mode in a dielectric structure it is relatively straightforward to understand some of their features. Any mode in a structure will tend to concentrate its energy into the regions of high dielectric constant while remaining orthogonal to modes of a different frequency. This can be formalised as the electromagnetic variational theorem which borrows heavily from the variational principal of quantum mechanics. This means that the lowest frequency state which corresponds with the smallest eigenvalue ω_0^2/c^2 has the field pattern that minimises the functional:

$$U_f(\mathbf{H}) = \frac{(\mathbf{H}, \hat{\Theta}\mathbf{H})}{(\mathbf{H}, \mathbf{H})}, \tag{3.36}$$

where $(\mathbf{F}, \mathbf{G})$ is the inner product of two vector fields and is defined as

$$(\mathbf{F}, \mathbf{G}) = \int d^3\mathbf{r}\mathbf{F}^*(\mathbf{r}) \cdot \mathbf{G}(\mathbf{r}), \tag{3.37}$$

and * indicates the complex conjugate. The functional U_f is known as the Rayleigh quotient and appears in a similar variational theorem for any Hermitian operator.

To see that the energy is concentrated in high dielectric field regions it is useful to write the energy functional, Eq 3.36, in terms of $\mathbf{E}$. Utilising the general

[1] This section follows Chapter 1 in [68]

properties of harmonic modes, the functional can be rewritten as,

$$U_f(\mathbf{H}) = \frac{(\nabla \times \mathbf{E}, \nabla \times \mathbf{E})}{(\mathbf{E}, \varepsilon(\mathbf{r})\mathbf{E})} \tag{3.38a}$$

$$= \frac{\int d^3\mathbf{r} \mid \nabla \times \mathbf{E}(\mathbf{r}) \mid^2}{\int d^3\mathbf{r}\varepsilon(\mathbf{r}) \mid \mathbf{E}(\mathbf{r}) \mid^2}. \tag{3.38b}$$

By concentrating the high electric field regions into the regions with high dielectric constant ε the value of U_F is minimised.

The energy functional needs to be distinguished from the physical energy in the electromagnetic field. The time-averaged physical energy can be separated into:

$$U_{\mathbf{E}} = \frac{\varepsilon_0}{4} \int d^3\mathbf{r}\varepsilon(\mathbf{r}) \mid \mathbf{E}(\mathbf{r}) \mid^2 \tag{3.39a}$$

$$U_{\mathbf{H}} = \frac{\mu_0}{4} \int d^3\mathbf{r} \mid \mathbf{H}(\mathbf{r}) \mid^2 . \tag{3.39b}$$

For harmonic modes the energy is exchanged between the electric and magnetic fields and vice-versa. The energy functional however is independent of the field strength as it has fields in the numerator and denominator, whereas the physical energy explicitly depends on the square of the field strength. This means that when working with photonic structures the fields are often normalised unless the physical energy is specifically of interest.

3.3.3 One-Dimensional Photonic Crystal[1]

The simplest form a photonic crystal can take is a multilayer film which consists of layers of alternating materials with different dielectric constants. Despite its simplicity, it can be used to create useful structures such as Bragg mirrors and to localise modes inside the structure. It is possible to analyse these kind of structures by considering a plane wave propagating through the structure and considering the sum of the reflections and refractions that occur at the interfaces between layers. Another method of analysing these structures is to construct a band diagram for the structure. This approach is generalisable to 2D and 3D arrangements and so will be explored here.

A multilayer film is defined as a structure where the material is periodic in the z direction and homogeneous in the xy plane. This means there is continuous translational symmetry in the xy plane and discrete translational symmetry in the z direction. A discrete symmetry is characterised by it's characteristic length known as the lattice constant a which is the distance between equivalent points and a primitive lattice vector which defines the direction of periodicity $\hat{z}$. In the case of a multilayer film it would be $\mathbf{a} = a\hat{\mathbf{z}}$. The symmetry means that $\varepsilon(\mathbf{r}) = \varepsilon(\mathbf{r} \pm \ell\mathbf{a})$ where ℓ is an integer. The area of the structure contained within a period of the symmetry is referred to as the unit cell and is repeated to form the bulk material.

Because of the translational symmetries, $\hat{\Theta}$ must commute with all of the translational operators in the xy plane as well as the translational operators for the lattice vectors $\mathbf{R} = \ell a\hat{\mathbf{z}}$. This means that the modes of $\hat{\Theta}$ are simultaneous eigenfunctions of both translation operators. These eigenfunctions are plane

[1]This section follows Chapter 4 in [68]

waves,

$$\hat{T}_{d\hat{\mathbf{x}}}e^{ik_x x} = e^{ik_x(x-d)} = (e^{-ik_x d})e^{ik_x x} \tag{3.40a}$$

$$\hat{T}_{d\hat{\mathbf{y}}}e^{ik_y y} = e^{ik_y(y-d)} = (e^{-ik_y d})e^{ik_y y} \tag{3.40b}$$

$$\hat{T}_{\mathbf{R}}e^{ik_z z} = e^{ik_z(z-\ell a)} = (e^{-ik_z \ell a})e^{ik_z z}, \tag{3.40c}$$

where $\hat{T}$ is the translational operator, k is the wave vector and d is the magnitude of the translation in the direction of the operator.

This allows modes to be classified by their k values but not all k values give unique solutions. Altering k_z by an integer multiple of $2\pi/a$ leaves the state unchanged and so the primitive reciprocal lattice vector is $\mathbf{b} = 2\pi/a\hat{\mathbf{z}}$.

The eigenvalue for any linear combination of degenerate eigenfunctions is the same as the eigenvalue of the any of the functions that make it up. This means any combination of the original modes can be put in the form

$$\mathbf{H}_{kx,kz}(r) = e^{ik_x x}\sum_m \mathbf{c}_{k_z,m}(y)e^{i(k_z+2\pi m/a)z} \tag{3.41a}$$

$$= e^{ik_x x}\cdot e^{ik_z z}\cdot \sum_m \mathbf{c}_{k_z,m}(y)e^{2i\pi m z/a} \tag{3.41b}$$

$$= e^{ik_x x}\cdot e^{ik_z z}\cdot \mathbf{u}_{k_z}(z,y), \tag{3.41c}$$

where the $\mathbf{c}$'s are coefficients of expansion that can be calculated from an explicit solution and $\mathbf{u}(z, y)$ is by definition a periodic function in z.[1]

[1]The choice of x in Eq 3.41 was an arbitrary decision and a similar treatment can be performed for $H_{ky,kz}(r)$.

The discrete periodicity in the z direction leads to a z dependence for $\mathbf{H}$ that is the product of a plane wave and a z-periodic function. A useful way to think about it is as a plane wave in free space that is modulated by a periodic function because of the periodic lattice:

$$\mathbf{H}(n, k_z, \mathbf{k}_{||}) = e^{i\mathbf{k}_{||}\cdot\rho} e^{ik_z z} \mathbf{u}_{n,k_z,\mathbf{k}_{||}}(z). \tag{3.42}$$

where n is the band number ordered by frequency such that the lowest frequency band corresponds to $n = 1$. At this point it can be convenient to combine k_x and k_y into $\mathbf{k}_{||}$ and denote ρ as the position in the x, y plane. In solid state physics this type of function is referred to as a Bloch state but can also be known as a Floquet mode. Since a lot of the formalism of photonics is borrowed from solid state physics these will be referred to as Bloch states in the rest of this thesis.

The function $\mathbf{u}$ takes the form $\mathbf{u}(z) = \mathbf{u}(z+R)$ where R is a integer multiple of the lattice constant a. Because of the symmetries of the system, $k_{||}$ can take any value but k_z is restricted to a finite interval known as the Brillouin zone which is the primitive cell of the reciprical lattice. Due to the crystal only having discrete translational symmetry in the z direction the Brillouin zone is one dimensional and can simply be deduced to be $-\pi/a < k_z \leqslant \pi/a$.

3.3.4 Two-Dimensional Photonic Crystal[1]

The previous section was concerned with the simplest form of photonic crystal, a one dimensional multilayer film, however these structures only have limited uses

[1]This section follows Chapter 5 in [68]

and so this section will look at expanding this formalism to include more complex two-dimensional structures. A two-dimensional crystal is periodic along two axes and homogeneous along its third. A realisable structure of this type would be a square-based lattice in the xy plane of long cylindrical rods with radius r and spacing of the lattice constant a. For simplicity the extent of the rods in the z direction is considered infinite. By tuning the lattice parameters a band gap can be achieved, preventing the propagation of waves within the periodic plane. The specifics of how band gaps form and behave is covered in Section 3.3.5.

To understand the electromagnetic modes that can exist in a two-dimensional crystal the symmetries of the system can be used to simplify the problem. In the z direction there is no limit on the value of the wave vector k_z and the mode must be oscillatory because in this direction the crystal is homogeneous. The crystal must also have discrete translational symmetry in the xy plane where $\varepsilon(\mathbf{r}) = \varepsilon(\mathbf{r}+\mathbf{R})$ where $\mathbf{R}$ is any linear combination of the primitive lattice vectors $a\hat{\mathbf{x}}$ and $a\hat{\mathbf{y}}$. Bloch's theorem can be used to analyse the $\mathbf{k}_{||}$ that are within the Brillouin zone. To distinguish between modes, they are categorised by k_z, $\mathbf{k}_{||}$ and n. The Bloch states take the form

$$\mathbf{H}_{n,k_z,\mathbf{k}_{||}}(\mathbf{r}) = e^{i\mathbf{k}_{||}\cdot\rho} e^{ik_z z} \mathbf{u}_{(n,k_z,\mathbf{k}_{||})}(\rho), \tag{3.43}$$

where ρ is the projection of $\mathbf{r}$ on the xy plane and $\mathbf{u}(\rho)$ is a periodic function, $\mathbf{u}(\rho) = \mathbf{u}(\rho + \mathbf{R})$ for all lattice vectors $\mathbf{R}$. The result of this is similar to that of the multilayer film but the roles of the plane and the z direction are reversed with $\mathbf{u}$ periodic in the plane and not the z direction.

If a state only propagates in the xy plane, the symmetry of the lattice allows us to separate the modes into their respective polarisations, transverse-electric(TE) with $E_{||}, H_z \neq 0$ and transverse-magnetic(TM) modes with $H_{||}, E_z \neq$. These are the same polarisations that are used to describe modes inside cavities and waveguides. Inside a crystal the TE and TM modes can have different band structures with features such as band gaps in one polarisation but not the other.

3.3.5 Photonic Band Gaps

By tuning the properties of the crystal through the type and dimensions of the materials used it is possible to create a band gap. A band gap is where there is a range of frequencies for which an electromagnetic wave is unable to propagate in one or more directions. If all directions are blocked it is known as a complete or total band gap and if propagation is allowed in some directions, a partial band gap.

3.3.5.1 One-Dimensional Band Gaps[1]

One-dimensional photonic structures were introduced in Section 3.3.3. These structures have periodically-alternating material in one direction z, and a homogenous distribution in the transverse xy plane. If the refractive indices of the materials were the same then all the states would lie on the light line which is given by

$$\omega(k) = \frac{ck}{\sqrt{\varepsilon}}. \tag{3.44}$$

However as the ratio of the materials permittivity increases a gap opens up

[1] This section follows Chapter 4 in [68]

between the first two bands. The gap between these bands is at its minimum at the limits of the Brillouin zone which is found at $k = \pi/a$ and corresponds to a wavelength of $2\,a$. This means that there are two positions that the nodes can take whilst maintaining the symmetry of the lattice: at the centre of the low-ε layer or the centre of the high-ε layer as can be seen in Fig 3.3.

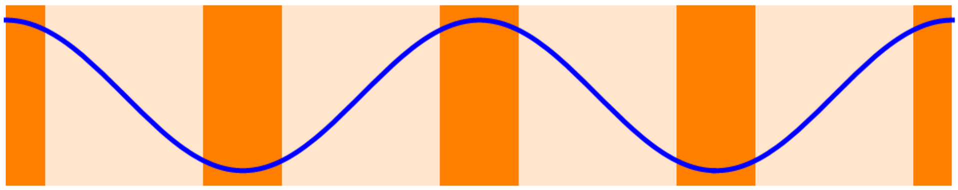

(a) Band 1

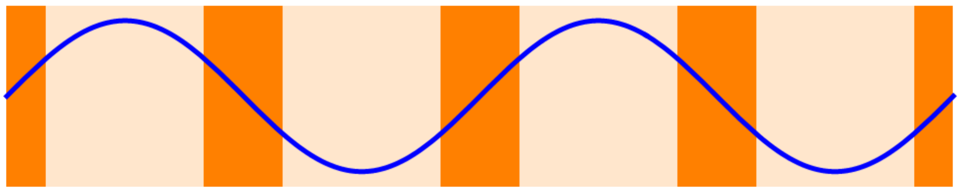

(b) Band 2

Figure 3.3: A one-dimensional photonic structure where the pale orange indicates the low permittivity region and the bright orange indicates high permittivity. The first two bands of the structure are shown in blue.

By applying the variational theorem it is found that the low frequency modes concentrate their energy in high-ε regions and as the frequency increases more of the energy is stored in the the low-ε region. When systems have large dielectric contrasts, both bands can concentrate their energy in the high-ε regions but have orthogonal energy distributions.

The size of a band gap is described by its frequency width $\Delta\omega$, however due to the scaling properties of Maxwell's Equations this is not the most practical way to talk about a band gap's size. If the lattice constant is scaled by a factor of s, the band gap size would be scaled by $1/s$. It is therefore more convenient to use a ratio of the width of the band gap and the central frequency of that gap, $\Delta\omega/\omega_m$, this is usually expressed as a percentage and known as the gap-midgap ratio. This measurement is also useful as it remains valid even when the frequency and wave vector are plotted in dimensionless units. For example the dimensionless frequency is equivalent to $a\omega/2\pi c$.

3.3.5.2 Two-Dimensional Band Gaps[1]

A two-dimensional photonic structure can also be used to create band gaps. Consider a two-dimensional square lattice which consists of cylindrical rods with a lattice constant of a. With a sufficiently high dielectric contrast this type of structure will open a complete band gap between its $n = 1$ and $n = 2$ TM bands. When plotting the band structure of two dimensional structures the $\mathbf{k}_{||}$ along the edge of the Brillouin zone is plotted. This is a suitable approximation to covering the entire zone as the maxima and minima of a band usually occur at the zone edges and corners.

A square lattice has a triangular irreducible Brillouin zone which can be related to the rest of the Brillouin zone through rotation. The three corners of the zone are found at $\mathbf{k}_{||} = 0$, $\mathbf{k}_{||} = \pi/a\hat{\mathbf{x}}$ and $\mathbf{k}_{||} = \pi/a\hat{\mathbf{x}} + \pi/a\hat{\mathbf{y}}$.

The band diagram in Fig 3.4 is for a two-dimensional square lattice with a scatterer radius of $r = 0.2\,a$ and a scatterer permittivity of $\varepsilon = 8.9$. In this case there is a complete band gap between the first and second TM modes with a gap-midgap ratio of 31.4%. The TE bands however, have no complete gap and the reason for this can be understood by considering how the polarisations behave

[1] This section follows Chapter 5 in [68]

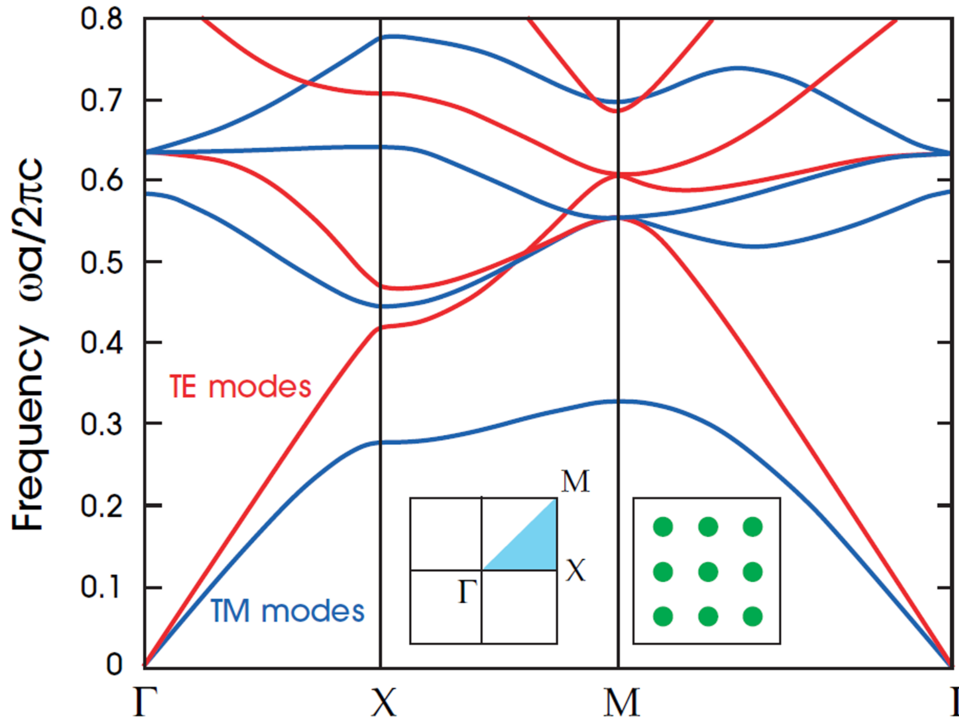

Figure 3.4: The band diagram of a square based photonic lattice of cylindrical scatterers of $\varepsilon = 8.9$ and $r = 0.2\,a$. *Reproduced from [68]*

at the material interface. When moving from the high-ε material to the low-ε material, the energy density $\varepsilon|\mathbf{E}|^2$ will decrease discontinuously when $\mathbf{E}$ is parallel to the interface but will increase discontinuously when $\mathbf{E}$ is perpendicular to the interface. This means that for TM bands where $\mathbf{E}$ is parallel to all the dielectric interfaces it is possible to have a high field concentration in the ε material, whereas in the case of TE bands, the electric field must cross a boundary which forces the electric field energy out of the high-ε material preventing a high field concentration and therefore the first two bands are much closer in frequency.

3.3.5.3 Evanescent Modes

Despite the crystal not being able to support extended modes with frequencies within the band gap there may be situations where these frequencies are injected from an external source. In this situation the wave vector of the mode becomes complex rather than purely real and the amplitude of the wave decreases exponentially as it extends into the crystal. This kind of mode is described as being evanescent and has the form

$$\mathbf{H}(\mathbf{r}) = e^{ikz}\mathbf{u}(z)e^{-\kappa z}, \tag{3.45}$$

where the complex wave vector is given by $k + i\kappa$. Due to the imaginary component of the wave vector the decay length is $1/\kappa$. The value of κ can be determined by analysing the modes above and below the gap. Expanding the upper band $\omega_2(k)$ in powers of k around the zone limit and this band takes the form $\Delta\omega = \alpha(\Delta k)^2$ where α is a constant that depends on the second derivative of the band.

For frequencies slightly higher than the top band, $\Delta\omega > 0$ which means Δk is purely real. However when the frequency fully enters the gap $\Delta\omega < 0$ and Δk become purely imaginary. As the frequency approaches the centre of the gap the size of Δk increases and since $\Delta k = i\kappa$, the rate of decay increases too. At the mid-gap frequency, κ reaches a maximum. As the frequency approaches the lower band, Δk decreases until it becomes purely real at the lower band.

Evanescent modes are valid solutions to Eq 3.35a, but they diverge as z goes to $\pm\infty$. If a crystal was perfect and infinite in size it would be impossible to physically excite these evanescent modes however with the inclusion of edges or defects it is possible to terminate the exponential growth and sustain an evanescent mode. A crystal defect can be resonant with one or more evanescent modes allowing the localisation of modes within the crystal. This will be elaborated on in the next section.

3.3.6 Localising Modes[1]

By using knowledge of the band structure of a photonic crystal it is possible to manipulate a structure to localise a mode to a specific location within the lattice. The way this is done is by introducing a defect into the lattice. This is usually achieved by altering the dimensions of a scatterer within the lattice or by removing a scatterer. To explore the effect of defects it is convenient to first consider the one dimensional example of a multilayer film. Suppose the thickness of the low-ε layer is altered, breaking the symmetry of the lattice. The defect will act like the interface between two films but when many wavelengths away from the defect the modes will look similar to those found in a perfect crystal.

[1]This section follows Chapter 5 in [68]

To understand what is happening inside a defect it is only necessary to look at the in-plane propagation and limit the frequency to those that are within the photonic band gap. Inside the crystal there are no extended states within the band gap but there can be evanescent states in the immediate vicinity of the defect. The band structure of a lattice is only valid inside a defectless lattice however knowledge of it allows us to split the frequency range into regions of extended and localised states.

The defect may permit localised modes to exist that have frequencies within the band gap. The film on either side of the defect acts like a frequency specific mirror and since the films are parallel to one another any light propagating in the z-direction will be reflected back and forth. As with any system of this nature such as those discussed in Section 3.2, the modes become quantised into discrete resonant frequencies. By increasing the thickness of the defect layer the frequency of the resonant modes is reduced and so can be lowered till they are inside the band gap range. A similar effect can be achieved by maintaining the size of the layer and altering the ε of the material. By tuning the parameters carefully the resonant mode can be pushed to the centre of the gap where the degree of localisation will be the strongest.

When looking at two-dimensional structures it is possible to produce a number of different defect types: surface, line and point defects. A surface defect is the easiest to produce as it is where the lattice terminates and therefore all practical designs must contain this kind of defect. A line defect is where a row of scatterers in the directions of one of the primitive lattice vectors are altered or removed. Finally, a point defect is when an individual scatterer is altered or removed.

As with a one-dimensional structure, introducing a defect in the lattice invalidates the band diagram for the lattice's in-plane wave vector but the symmetry remains intact for $k_z = 0$ and therefore looking at the in-plane propagation is still valid as the TE and TM modes remain decoupled.

The removal or alteration of a row or part of the row can be used as a waveguide as the defect will split the lattice into two regions, both of which act as a mirror. Having two parallel mirrors allows the structure to support modes that are resonant within the defect but are inside the band gap of the lattice. By removing or altering a single rod a cavity like structure is produced as all the surrounding lattice will act as a mirror that, with carefully tuned parameters, can support a resonant mode within the band gap.

The removal of the scatterer will reduce the permittivity of the bulk material in the vicinity of the defect and this enables us to use perturbation theory to calculate the effect of the change, $\Delta\varepsilon$. By applying a small perturbation to

$$\nabla \times \nabla \times \mathbf{E}(\mathbf{r}) = \left(\frac{\omega}{c}\right)^2 \varepsilon(\mathbf{r})\mathbf{E}(\mathbf{r}), \tag{3.46}$$

it can be shown that

$$\Delta\omega = -\frac{\omega}{2}\frac{\int d^3\mathbf{r}\Delta\varepsilon(\mathbf{r})|\mathbf{E}(\mathbf{r})|^2}{\int d^3\mathbf{r}\varepsilon(\mathbf{r})|\mathbf{E}(\mathbf{r})|^2} + O(\Delta\varepsilon^2). \tag{3.47}$$

The result of Eq 3.47 is that if the permittivity is reduced the frequency of the band is reduced. The effect on the band diagram is that it pushes a frequency state that usually exists below the band gap up into the gap.

If the frequency of the mode that is localised to the defect is slightly above or below the band gap it is able to leak into the continuum states that form the bands of the perfect lattice. This means that the mode is no longer localised to only the defect and it is known as a leaky mode or resonance. The defect can now lose energy to the continuum state.

All the lattices considered so far have been infinite, such an idealised defect is capable of perfectly confining a mode, however if a finite and therefore realisable structures is considered, it is found that the localised state can leak energy into the surrounding medium. Within the lattice the defect modes decay exponentially and therefore increasing the number of lattice periods surrounding the defect the rate of leakage can be reduced. This means that with a sufficiently large lattice the losses to the surroundings become secondary to losses within the dielectric itself. A structure using this principal is described in detail in Chapter 6.

Chapter 4

Light Shining Through a Wall Experiments

There are a number of techniques to search for WISPs, many of the experiments that exploit photon-WISP interactions draw from ideas first proposed in the early 1980's by Lev Okun[69] and Pierre Sikivie[70]. One of the most popular techniques has been to create a resonating structure that can make the small electromagnetic field created by galactic or solar WISPs detectable. This technique has limitations imposed by the uncertainties in the properties of the source which were discussed in Section 2.4. Light shining through a wall(LSW)experiments overcome this limitation by having a dedicated source. This chapter will introduce the theory that underpins LSW experiments that search for HSPs.

4.1 Modified Maxwell's Equations

The first step to understanding how a LSW experiment works is to understand the impact of an additional field which is invariant under a local U(1) transformation on the electromagnetic field U(1). This is done by performing a Lagrangian variation to find the equations of motion for the field which will produce equations which are approximately Maxwell's equations. The starting point is the Lagrangian density that describes the interaction between the SM photon and the HSP field, Eq 2.6 which is repeated here for convenience:

$$\mathcal{L} = -\frac{1}{4}F^{\mu\nu}F_{\mu\nu} - \frac{1}{4}B^{\mu\nu}B_{\mu\nu} - \frac{1}{2}\chi F^{\mu\nu}B_{\mu\nu} - \frac{1}{2}m_{\gamma'}^2 B_\mu B^\mu. \tag{4.1}$$

Recall that F is the SM electromagnetic field tensor and B is the HSP field tensor where μ and ν are the summation indices, χ is the mixing parameter and $m_{\gamma'}$ is the mass of the HSP. The Lagrangian density can be transformed by applying

$$B^\mu \to B'^\mu - \chi A^\mu, \tag{4.2}$$

applied to it where ' denotes the transformed HSP field. For simplicity it is easier to apply the transform to each term in the Lagrangian individually as shown:

$$\begin{aligned}
-\frac{1}{4}F^{\mu\nu}F_{\mu\nu} &\rightarrow \text{Unchanged} && \text{(4.3a)}\\
-\frac{1}{4}B^{\mu\nu}B_{\mu\nu} &\rightarrow -\frac{1}{4}\left(B'^{\mu\nu}B'_{\mu\nu}+\chi^2F^{\mu\nu}F_{\mu\nu}-2\chi F_{\mu\nu}B'^{\mu\nu}\right) && \text{(4.3b)}\\
-\frac{1}{2}\chi F^{\mu\nu}B_{\mu\nu} &\rightarrow -\frac{\chi}{2}\left(F^{\mu\nu}B'_{\mu\nu}-\chi F^{\mu\nu}F_{\mu\nu}\right) && \text{(4.3c)}\\
-\frac{1}{2}m^2_{\gamma'}B_\mu B^\mu &\rightarrow \frac{1}{2}m^2_{\gamma'}\left(B'^{\mu}B'_{\mu}+\chi^2A^\mu A_\mu-2\chi A^\mu B'_\mu\right). && \text{(4.3d)}
\end{aligned}$$

where A_μ is the EM four vector and B_μ is the four vector representing the HSP field. Normalising Eq 4.1 by redefining the electron charge $e^2 \rightarrow e^2/(1-\chi^2)$ gives

$$\mathcal{L} = -\frac{1}{4}F^{\mu\nu}F_{\mu\nu} - \frac{1}{4}B^{\mu\nu}B_{\mu\nu} + \frac{1}{2}m^2_{\gamma'}B'^{\mu}B'_{\mu} + \frac{1}{2}m^2_{\gamma'}\chi^2A^\mu A_\mu - m^2_{\gamma'}\chi A^\mu B'_\mu. \quad (4.4)$$

The Lagrangian variation $A^\mu \rightarrow A^\mu + \varepsilon\delta A^\mu$ can be applied to obtain the equations of motion. Again taking each term individually for ease:

$$\begin{aligned}
-\frac{1}{4}F^{\mu\nu}F_{\mu\nu} &\rightarrow -\frac{1}{4}F^{\mu\nu}F_{\mu\nu}+\varepsilon F^{\mu\nu}\partial_\nu\delta A_\mu && \text{(4.5a)}\\
-\frac{1}{4}B^{\mu\nu}B_{\mu\nu} &\rightarrow \text{Unchanged} && \text{(4.5b)}\\
\frac{1}{2}m^2_{\gamma'}B'^{\mu}B'_{\mu} &\rightarrow \text{Unchanged} && \text{(4.5c)}\\
\frac{1}{2}m^2_{\gamma'}\chi^2A^\mu A_\mu &\rightarrow \frac{1}{2}m^2_{\gamma'}\chi^2(A^\mu A_\mu+2\varepsilon A^\mu\delta A_\mu)+\mathcal{O}(\varepsilon^2) && \text{(4.5d)}\\
-m^2_{\gamma'}\chi A^\mu B'_\mu &\rightarrow -m^2_{\gamma'}\chi A^\mu B'_\mu - m^2_{\gamma'}\varepsilon\chi\delta A^\mu B'_\mu. && \text{(4.5e)}
\end{aligned}$$

The Lagrangian density with the variation is therefore

$$\begin{aligned}\mathcal{L} = &-\frac{1}{4}F^{\mu\nu}F_{\mu\nu} + \varepsilon F^{\mu\nu}\partial_\nu \delta A_\mu - \frac{1}{4}B^{\mu\nu}B_{\mu\nu} + \frac{1}{2}m_{\gamma'}^2 B'^{\mu}B'_\mu \\ &+ \frac{1}{2}m_{\gamma'}^2\chi^2(A^\mu A_\mu + 2\varepsilon A^\mu \delta A_\mu) + \mathcal{O}(\varepsilon^2) - m_{\gamma'}^2\chi A^\mu B'_\mu - m_{\gamma'}^2\varepsilon\chi\delta A^\mu B'_\mu. \end{aligned} \tag{4.6}$$

To find the equations of motion from the Lagrangian density its action needs to be minimised with respect to small variations of the fields resulting from small variations in ε, giving

$$\delta S = \int \frac{d\mathcal{L}}{d\varepsilon}\bigg|_{\varepsilon=0} d^4x = 0 \tag{4.7}$$

where

$$\frac{d\mathcal{L}}{d\varepsilon} = \partial_\nu(F^{\mu\nu}\delta A_\mu) + (-\partial_\nu F^{\nu\mu} + m_{\gamma'}^2\chi^2 A^\mu - m_{\gamma'}^2\chi B'_\mu)\delta A_\mu + \mathcal{O}(\varepsilon). \tag{4.8}$$

By removing the terms that will integrate to become 0, the action becomes

$$\delta S = \int -\partial_\nu F^{\nu\mu} + m_{\gamma'}^2\chi^2 A^\mu - m_{\gamma'}^2\chi B'_\mu \delta A_\mu = 0. \tag{4.9}$$

Therefore the field equations becomes

$$\partial_\nu F^{\mu\nu} = m_{\gamma'}^2\chi(\chi A^\mu - B'^\mu). \tag{4.10}$$

The implication of Eq 4.10 is that any electromagnetic field acts as a source for HSPs and vice versa. This means that it is possible to search for HSPs by either looking for the EM field that they generate or by looking for the energy 'lost' from an EM field. The loss mechanisms of EM fields can be complicated making the detection of small deficits in the power difficult. Thermal noise however, is relatively well understood and this makes detecting any excess to the thermal noise in an otherwise 'radio silent' environment relatively easy. Due to these reasons the majority of experimental searches have concentrated on looking for the generated EM field from the HSP.

4.2 Shining Optical Light Through a Wall

As previously stated, a consequence of Eq 4.10 is that any electromagnetic field acts as a source of HSPs and vice versa; it has also been previously stated that the HSP does not couple directly to electric charge. Due to these two reasons, it is possible for the HSP to transmit an electromagnetic signal to a region which a photon is otherwise unable to reach. Experiments using this approach are commonly known as light shining though a wall experiments.

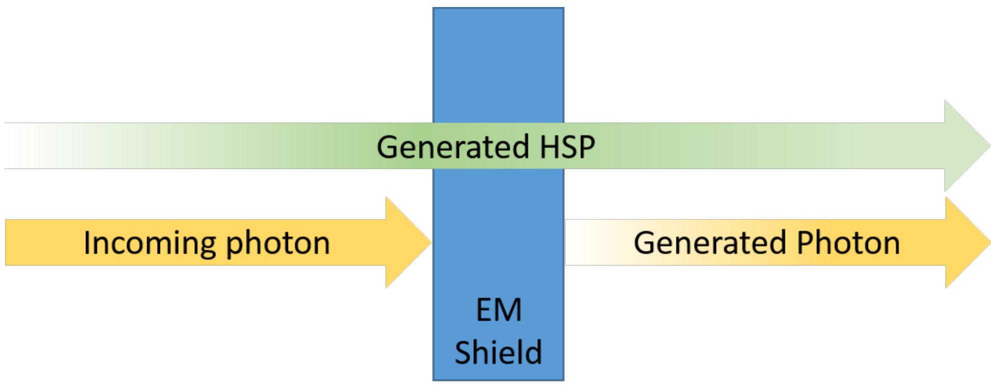

Figure 4.1: A simplified diagram of a light shinging through a wall experiment. On the left is an incoming photon which generates a HSP. The HSP passes through shielding relatively unaffected and then generates a photon.

The simplest way to think about a LSW experiment is to think about how energy flows through the experiment. Figure 4.1 shows a simplified schematic of a LSW experiment. As a EM wave travels, some of the energy of the EM wave transfers into a HSP wave. When both waves reach the shielding, the EM wave is terminated and it's energy is either absorbed or reflected while the HSP wave continues through the shield. Once the HSP wave has passed the shield some of the energy of the HSP wave transfers to a EM wave. This whole process can be simply written as

$$\mathcal{P}_{out} = P_{trans}\mathcal{P}_{in}, \tag{4.11}$$

where $\mathcal{P}_{out}$ is the detectable power, $\mathcal{P}_{in}$ is the power put into the experiment and P_{trans} is the probability that a photon will transition to a HSP and then generate a detectable photon. The starting point to calculate P_{trans} is the probability of a photon in free space transitioning into a HSP,

$$P_{\gamma\rightarrow\gamma'} = 4\chi^2 \sin^2(\frac{\Delta kl}{2}) \tag{4.12}$$

where l is the distance travelled by the photon and Δk is the momentum difference between the photon and the HSP[53], and the use of natural units can be assumed throughout this chapter.

$$\Delta k = \omega - \sqrt{\omega^2 - m_{\gamma'}^2} \tag{4.13}$$

For the probability of a HSP transitioning to a photon is the same process in reverse which has the same probability. The probability of a photon making the transition to HSP and back again in free space is therefore,

$$P_{trans} = 16\chi^4 \sin^2\left(\frac{\Delta k l_1}{2}\right) \sin^2\left(\frac{\Delta k l_2}{2}\right) \tag{4.14}$$

where l_1 is the length travelled by the photon before reaching the shielding and l_2 is the length the HSP has to travel before transitioning to a photon and being detected[53].

Since χ and Δk are expected to be small, the distance over which the experiment takes place needs to be as long as possible. When this approach was first conceived the use of astronomical objects was suggested to get suitable distances and high power photon sources such as super-novae. However to detect a signal within the ambient light of these objects would be extremely difficult[69].

One method of extending the distance travelled by a photon without requiring an increase in the length of the experiment is to place the photon beam inside a resonant cavity. For optical light, cavities are created by placing mirrors at either end of the beam. However, as mirrors are not perfect, the losses cause the beam to have a finite life span in the cavity. The increase in the life of a photon inside a cavity is given the finesse, $\mathcal{F}$ of the cavity. Whilst resonating in the cavity, the flux in the direction of the detector contributes to the HSP field which it generates and therefore the probability of transition is increased by a factor of $(\mathcal{F}+1)/2$. It is fairly obvious that there will be an improvement in the 'source' side of the experiment but the enhancement seen from the addition of a resonator can also be applied to the detector, a further discussion of this can be found in Section 4.3.1. The size of this resonant amplification is the same as that for the source and therefore the probability of transmission is [71]

$$P_{trans} = 16\chi^4 \left[\frac{\mathcal{F}_1 + 1}{2}\right] \left[\frac{\mathcal{F}_2 + 1}{2}\right] \times \left[\sin\left(\frac{\Delta k l_1}{2}\right) \sin\left(\frac{\Delta k l_2}{2}\right)\right]^2 . \qquad (4.15)$$

4.3 Shining Microwaves Through a Wall

A metallic cavity can be used to support a resonating mode in much the same way as the Fabry-Pérot resonator used in optical LSW experiments enabling the method to be used at microwave frequencies and therefore opening up the possibility of searches in the μeV to meV mass range. Even though qualitatively there is little difference between an optical and microwave LSW a different formalism is generally used which will be introduced in Section 4.3.1. Early microwave LSW experiments[64, 66] followed the optical experiments by only considering the transverse polarisation of the HSP. However, the mass of the HSP allow it to sustain a longitudinal polarisation which is not available to the photon. Recent astrophysical exclusions which have considered the longitudinal mode have been able to obtain more sensitive limits than those which only considered the transverse polarisation[72, 73]. Utilising the longitudinal polarisation in an optical LSW experiment is non-trivial but for microwave LSW experiments only the geometry of the experiment needs to be adapted as will be discussed in Section 3.3.6.

4.3.1 Transverse Coupling

The approach taken at optical frequencies can be easily adapted to RF structures. The number of passes of a photon through an optical cavity which is given by the cavity's finesse $\mathcal{F}$, is conceptually the equivalent of the quality(Q) factor of an RF cavity:

$$\frac{\mathcal{F}+1}{2} \approx Q. \tag{4.16}$$

Therefore by taking Eq 4.15 and Eq 4.16 the maximum probability of transmitting a photon from the source to the emitter via a HSP can be said to be,

$$P_{trans}^{max} \sim \chi^4 Q_1 Q_2. \tag{4.17}$$

To calculate the actual probability of transmission of EM power from the emitter cavity to the detector in detail, the first step is understanding how the field in the emitter generates the HSP field. The starting point for this is the equations of motion for the system that are derived from Eq 4.10:

$$(\partial^\mu \partial_\mu + m_{\gamma'}^2)B' = \chi m_{\gamma'}^2 A, \tag{4.18a}$$

$$(\partial^\mu \partial_\mu + \chi^2 m_{\gamma'}^2)A = \chi m_{\gamma'}^2 B' \tag{4.18b}$$

where A is the EM four-vector and B' is the HSP four-vector. The EM field distribution in the cavity can be solved analytically for simple cavity geometries as was discussed in Section 3.2, but numerical simulations are often used for complicated structures. The mode inside the cavity is separated into its spatial and temporal components:

$$\Psi(\mathbf{r}, t) = \psi(t)\Psi(\mathbf{r}), \tag{4.19}$$

where Ψ can represent either the E or B field and ψ is the purely temporal component of the field. Since the HSP doesn't interact with normal matter its field permeates the space around the source freely. The solution is then found from the retarded massive Green's function [74],

$$\Xi(\mathbf{r}, t) = \chi m_{\gamma'}^2 \int_V d^3\mathbf{y} \frac{\exp(ik|\mathbf{r} - \mathbf{y}|)}{4\pi|\mathbf{r} - \mathbf{y}|} \psi(t)\Psi(\mathbf{y}), \tag{4.20}$$

where Ξ represents either the electric-like or magnetic-like component HSP field, V is the volume of the emitter cavity and

$$k^2 = \omega^2 - m_{\gamma'}^2. \tag{4.21}$$

If $m_{\gamma'} > \omega$, the HSP cannot be radiated but can be virtual within a distance of approximately $1/m_{\gamma'}$ of the emitter cavity. In the detector the Ξ field now acts as a source to excite the EM field inside. The wave equation inside the detector can be solved by separating the spatial and components as in Eq 4.19, $\Psi'(\mathbf{r}, t) = \psi'(t)\Psi'(\mathbf{r})$,

$$\left(\frac{d^2}{dt^2} + \frac{\omega_0'}{Q'}\frac{d}{dt} + \omega_0'^2\right)\psi'(t) = \xi(t) \tag{4.22}$$

where the primed variables indicate they are associated with the detector. The driving force $\xi(t)$ is obtained by separating the spatial and temporal components of Eq 4.18a, multiplying by the EM solution to the cavity $\Psi'(r)$ and integrating over the volume of the cavity V',

$$\xi(t) = \chi^2 m_{\gamma'}^4 \psi(t) \int_{V'}\int_V d^3\mathbf{r} d^3\mathbf{y} \frac{\exp(ik|\mathbf{r} - \mathbf{y}|)}{4\pi|\mathbf{r} - \mathbf{y}|} \Psi(\mathbf{y})\Psi'(\mathbf{r}) \tag{4.23}$$

where **r** and **y** are the co-ordinate systems of the detector and emitter respectively. To gain the full benefits of resonant enhancement the cavities are designed so that $\omega_0' = \omega_0$. This can be simplified to

$$\xi(t) = \psi(t)\frac{\chi^2 m_{\gamma'}^4}{\omega_0^2} G(k/\omega_0), \tag{4.24}$$

where G is a dimensionless geometric factor. The G-factor encodes the physical set-up of the experiment, the cavity shapes, sizes and relative separation and is given by [74]

$$G(k/\omega_0) \equiv \omega_0^2 \int_{V'} \int_{V} d^3\mathbf{x} d^3\mathbf{y} \frac{\exp(ik|\mathbf{x}-\mathbf{y}|)}{4\pi|\mathbf{x}-\mathbf{y}|} \Psi(\mathbf{x})\Psi'(\mathbf{y}). \tag{4.25}$$

Since the cavity has a finite Q-factor, it takes some time to reach its maximum amplitude. This is referred to as the filling time. After allowing the experiment to run for a minimum of the filling time, the amplitude of the EM field becomes constant and is given by

$$\psi_0' = iQ' \frac{\chi^2 m_{\gamma'}^4}{\omega_0^4} G\psi_0. \tag{4.26}$$

where the subscript $_0$ denotes the constant amplitude. To describe a physical set-up, this constant amplitude needs to be related to the power inside the emitter and also the power which is extractable from the detector. For a RF cavity the stored power in a cavity based on the power put in or taken out is,

$$\mathcal{P} = \frac{\omega_0}{Q_e} U, \tag{4.27}$$

where U is the stored energy of the cavity, Q_e is the external Q-factor of the cavity and $\mathcal{P}$ is the power in/out the cavity. From this it is clear that after the filling time the probability of a photon passing through the shielding and being detected in the second cavity is approximately

$$P_{\text{trans}} = \frac{\mathcal{P}_{det}}{\mathcal{P}_{em}} = \frac{Q|a^0_{det}|^2}{Q'|a^0_{em}|^2} = \chi^4 QQ' \frac{m^8_{\gamma'}}{\omega^8_0}|G|^2.^1 \tag{4.28}$$

4.3.2 Exclusions From Transverse Coupling

Just as with any particle physics experiment the goal of a HSP LSW experiment is to discover the existence of the HSP or to set limits on the parameter space for the HSP. When a negative result is found the limits that are set are dictated by the sensitivity of the experiment. To calculate the sensitivity of the experiment, the first stage is to re-arrange the probability of transmission between the cavities, Eq 4.28, and make the coupling factor χ the subject,

$$\chi = \sqrt[4]{\frac{P_{\text{Trans}}\omega^8_0}{QQ'm^8_{\gamma'}|G|^2}}, \tag{4.29}$$

Following from Eq 4.29 the probability P_{Trans} can be thought of as the ratio of the number of signal photons in the emitter and the detector,

$$P_{\text{Trans}} = \frac{N_{\text{Det}}t}{N_{\text{Em}}t}, \tag{4.30}$$

where $N_{\text{Det,Em}}$ is the number of photons in the detector and emitter per unit

[1]When the differences between the ohmic and external Q-factors are included fully in the treatment, a factor of 1/4 is introduced for regularly conducting cavities. However, when superconducting cavities are considered, this equation holds true due to the need to detune the cavities.

time respectively, and t is the running time of the experiment. To be detectable N_{Det} has to be large enough to be distinguished from fluctuations in the background noise. This condition is set by using standard Poisson statistics on the noise such that

$$N_{\mathrm{Det}} t = n\sqrt{N_{\mathrm{Bg}} t}, \tag{4.31}$$

where n is the number of standard deviations of significance desired, t is the run time of the experiment and N_{Bg} is the number of background photons per unit time. The probability of transmission therefore must be

$$P_{\mathrm{Trans}} = \frac{n\sqrt{N_{\mathrm{Bg}} t}}{N_{\mathrm{Em}} t}, \tag{4.32}$$

or higher if a HSP signal is to be detected.

After the experiment has been running for sufficient time, a steady state is reached when the power in the emitter and detector are constant. When this point has been reached it is valid to say that the probability of transmission is equal to the ratio of the power in the emitter to the power in the detector and hence the smallest detectable value of χ is given by

$$\chi = \sqrt[4]{\frac{n^2 N_{Bg} \omega_0^{16}}{Q^2 Q'^2 N_{Em}^2 t m_{\gamma'}^{16} |G|^4}}. \tag{4.33}$$

The background can be estimated by the number of thermal photons inside the detector cavity in a finite bandwidth Δf to be

$$N_{Bg} = \frac{k_B T \Delta f}{\omega} \tag{4.34}$$

where it is assumed that Δf is small enough that variations in the black body spectrum are negligible over the range. Since the detector consists of a cavity and amplifiers it is possible to combine their noise contributions using the Friis equation,

$$T_{eq} = T_1 + \frac{T_2}{G_1} + \frac{T_3}{G_1 G_2} + ... \tag{4.35}$$

where T_1 is the temperature of the cavity, $T_{2,3}$ are the electrical noise temperatures of the respective amplifiers and $G_{1,2}$ is the gain of the amplifiers. Therefore the smallest detectable χ is

$$\chi = \sqrt[4]{\frac{n^2 k_B (T_1 + T_2/G_1 + ...)\Delta F \omega_0^{15}}{Q^2 Q'^2 N_s^2 t m_{\gamma'}^{16} |G|^4}}. \tag{4.36}$$

4.3.3 Longitudinal Coupling

When an electrical current excites a HSP it excites both the longitudinal and transverse components. A convenient place to start is to think about the intuitive difference between operating in the transverse and longitudinal modes. As the HSP enters the shielding the EM field it generates will interact with the charges in the wall, moving them in such a way that generates a photon that will oppose the incident HSP. Since the photon cannot generate a longitudinal component, this cancellation only takes place with the transverse mode.

To understand the effect of the longitudinal polarisation on the observable result of the experiment the natural starting point, as in the transverse case, is by describing the E and B fields of the chosen cavity mode. Again, as in the transverse case the spatial and time components are separated to give

$$\mathbf{E}(\mathbf{r}, t) = \mathbf{E}(\mathbf{r})e^{i\omega t}, \tag{4.37}$$

$$\mathbf{B}(\mathbf{r}, t) = \mathbf{B}(\mathbf{r})e^{i\omega t}, \tag{4.38}$$

where ω is the operational frequency of the cavity. Since the length of time that the experiment runs is much longer than the length of an RF cycle it can be assumed that a steady state exists and the time variation can be neglected. This mode then generates a HSP field which is given by Eq 4.20. Any effects of the shielding on the HSP is supressed by a factor of χ, this means the HSP field penetrates the shielding and is able to excite the matching mode inside the detector cavity. The excited field is given by

$$\Psi(\mathbf{r}) = -\frac{Q}{\omega}\frac{\int_{rec} d^3\mathbf{x}\mathbf{E}^*_{\text{cav}}(\mathbf{x}) \cdot \mathbf{J}_{\text{eff}}(\mathbf{x})}{\int_{rec} d^3\mathbf{x}|\mathbf{E}_{cav}(\mathbf{x})|^2}\Psi_{cav}(\mathbf{r}), \tag{4.39a}$$

$$\mathbf{J}_{\text{eff}}(\mathbf{x}) = -\frac{i\chi}{\omega}\left[m^2_{\gamma'}\Xi_E(\mathbf{x}) - \vec{\nabla}(\vec{\nabla} \cdot \Xi_E(\mathbf{x}))\right], \tag{4.39b}$$

where d^3x is the volume element of the detector cavity[75]. The effective current $\vec{J}_{\text{eff}}$ represents how the HSP field excites the electric field in the detector. This is where the difference between the longitudinal and transverse mode takes effect. If the HSP field is purely transverse then $\vec{\nabla} \cdot \xi_E = 0$ but if the field is purely longitudinal then $\vec{\nabla}(\vec{\nabla} \cdot \Xi_E) = -k^2\Xi_E$. This simplifies $\vec{J}_{\text{eff}}$ to [75]

$$\mathbf{J}_{\text{eff}}(\mathbf{x}) = -\frac{i\chi}{\omega}\Xi_E(\vec{x}) \times \begin{cases} m^2_{\gamma'} & \text{(Purely transverse)} \\ \omega^2 & \text{(Purely longitudinal).} \end{cases} \tag{4.40}$$

Comparing the polarisations in Eq 4.40 it is clear to see that the strength of the transverse mode is proportional to the mass of the HSP which is being probed whereas the longitudinal mode is proportional to the frequency of the cavities. Due to this difference in the behaviour of the longitudinal and transverse polarisations, as the mass of the HSP decreases the longitudinal mode will lead to a higher field strength in the detector as it approaches the low mass limit. This leads to a probability of transmission of the form

$$P_{\text{trans}} = \chi^4 Q Q' \frac{m_{\gamma'}^4}{\omega_0^4} |G|^2. \tag{4.41}$$

In this chapter so far both the purely transverse and purely longitudinal couplings have been considered. In reality any experiment will couple through a combination of both transverse and longitudinal modes and therefore a full treatment would be required. However, for the exclusions presented in Chapter 5 and Chapter 6 the far-field approximations of the pure polarisations has been considered.

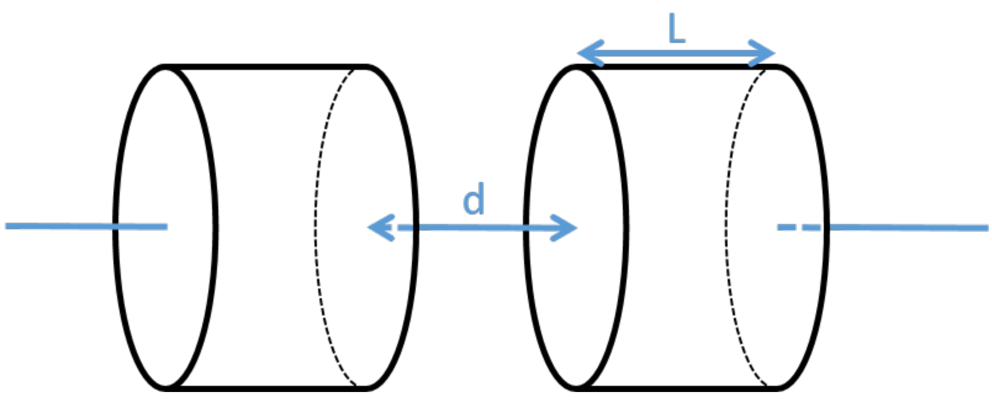

Figure 4.2: A schematic diagram of a longitudinally coupled light shining through a wall experiment. The cavities are stacked around a common axis which would form a waveguide it the cavities were connected.

To take advantage of the longitudinal mode, the cavities needs to be orientated such that the longitudinal polarisations share a common axis as shown in Fig 4.2. Due to the shielding required to operate a LSW experiment the separation between the cavities d, is usually greater than the length of the cavity L. When this condition is met, the HSP field can be approximated as a longitudinal plane wave meaning the electric like component of the HSP field becomes

$$\Xi_E = -\frac{1}{2} i\chi \frac{m_{\gamma'}^2 L}{\omega^2 d} \alpha_{01} J_1(\alpha_{01}) \left(\frac{2\sin(\frac{kL}{2})}{kL} \right) \Psi_{em}. \tag{4.42}$$

where $\alpha_{01} = \omega R$ and J is the Bessel function as described in Section 3.2 [75]. By following from this point in the same manner as before, the probability of transmission bewteen two cavities via the longitudinal polarisation of the HSP is found to be

$$P_{\text{det}} = Q\chi^2 \frac{m_{\gamma'}^2 L}{\omega^2 d} \left(\frac{2\sin(\frac{kL}{2})}{kL} \right)^2, \tag{4.43}$$

where P_{det} is the probability of detecting the incoming HSP for cylindrical cavities operated in the TM010 mode[75].

4.3.4 Exclusions From Longitudinal Coupling

As in Section 4.3.2, when a longitudinally coupled LSW experiment returns a negative results, the exclusion which that result represents is calculated from the probability of transmission between the cavities via the hidden sector P_{trans}.

$$\chi = \sqrt[4]{\frac{P_{\mathrm{trans}}\omega^2 d^2}{Q^2 m_{\gamma'}^2 L^2}\left(\frac{kL}{2\sin\frac{1}{2}kL}\right)^2}. \tag{4.44}$$

The condition for detection which was described in Section 4.3.2 can again be applied here so by applying Eq 4.32, Eq 4.44 becomes

$$\chi = \sqrt[4]{\frac{n\sqrt{N_{\mathrm{Bg}}t}\,\omega^2 d^2}{N_{\mathrm{Em}}tQ^2 m_{\gamma'}^2 L^2}\left(\frac{kL}{2\sin\frac{1}{2}kL}\right)^2}. \tag{4.45}$$

4.4 Experimental Exclusions

In Section 4.3.2 and Section 4.3.4 the performance of an experiment was calculated based on the key figures of the experiment. For an actual experiment however, the exclusions need to be calculated directly from the recorded data. To do this Eq 4.33 and Eq 4.45 are used, with N_{Em} being the recorded power inside the emitter and N_{Bg} the recorded power inside the detection cavity. When the recorded frequency window is wide enough to allow the expected signal window to be isolated from the background noise, the standard deviation of the measured background can be used instead of applying Poisson statistics. By using the measured noise, it is possible to produce exclusions which are stronger than would be expected from looking at the key figures alone.

Chapter 5

The CASCADE Experiment

5.1 CASCADE Overview

The Cockcroft Institute of Accelerator Science and Technology and Daresbury Laboratory regularly test RF cavities for upcoming accelerators, light sources and industrial projects. Many of these cavities are superconducting and therefore have a high quality factor and need to be tested at high power to be properly characterised. Characterisation takes place in the vertical test facility which is capable of accommodating multi-cell superconducting cavities. The cavities can be cooled to 2 K and the cryogenic system is capable of handling 1 W of thermal load[76]. For example it has been proposed to use this system to test multi-cell 1.3 GHz cavities with the goal of achieving Q-factors of 10^{10}. This means the cavities being tested have properties well-suited to be emitters for a LSW experiment.

The CASCADE experiment is planned to take place over multiple phases with the eventual goal being the design of a detector that is suitable to take data parasitically while cavities are being tested in the vertical test facility. The first phase of CASCADE was a proof of principle experiment which aimed to show that it was possible to make an exclusion measurement using off-the-shelf components operated at room temperature. This has now been completed as part of this thesis work. The low temperature measurement were originally planned but were not able to be completed but the results of preliminary investigations can be found in Appendix C.

For the first phase it was desirable to have full control of the emitter and detector cavities and hence, it was decided that two 1.3 GHz cavities would be built. In a later phase both cavities could then be used as detectors for runs with an external source. The use of multiple cavities has the potential to allow a stronger control on the systematic uncertainties in the measurement for example by exploiting differing G-factors. A schematic of a possible geometry is shown in Fig 5.1.

5.2 Estimated Performance

The probability of a photon passing from a source to a detector via the transverse component of the HSP field is given Eq 4.28 which was calculated from in Section 4.3.1. By multiplying P_{trans} by the input power, the expected signal power can be estimated.

Consider the case of a generic pillbox cavity. The Q of a copper cavity at room temperature is typically $\mathcal{O} \sim 10^4$ and the G-factor for microwave cavity LSW experiments is typically $\mathcal{O} \sim 1$. In the most optimistic case, the HSP will have a mass such that $m_\gamma/\omega = 1$ and have the highest unexcluded value of

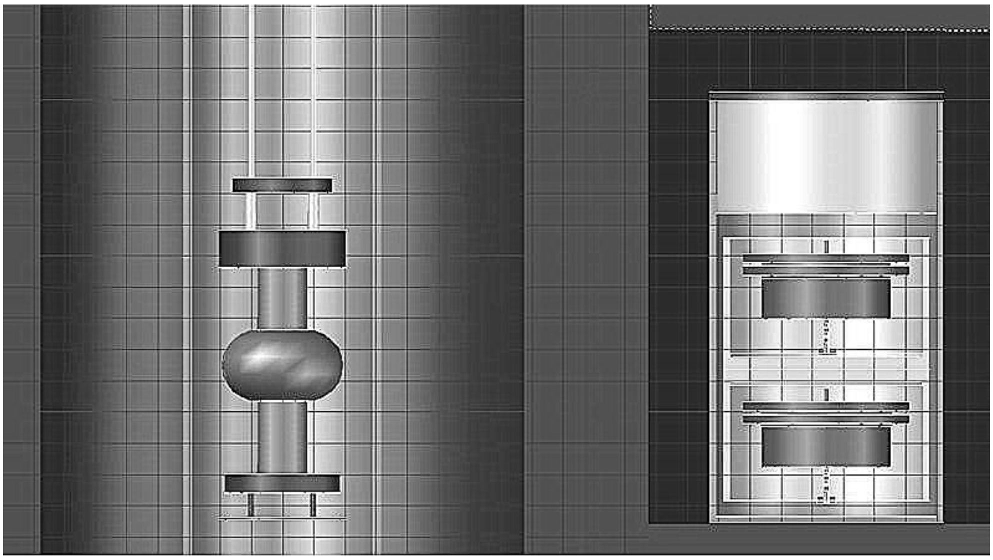

Figure 5.1: A mock-up of a CASCADE measurement utilising two detector cavities on the right side, and a superconducting cavity being tested in the vertical test facility on the left.

the coupling factor χ, which in the $m_{\gamma'}$ range of 10^{-6} to 10^{-4} eV corresponds to $\mathcal{O} \sim 10^{-7}$. If the emitter was powered with 1 W, the expected signal power would be $\mathcal{O} \sim 10^{-20}$ W[1]. Given that at room temperature the thermal noise is expected to be $\mathcal{O} \sim 10^{-21}$ W, the signal from HSPs should in principal be detectable above the noise.

The expected exclusion for a microwave LSW can also be calculated by using Eq 4.28 and the properties assumed in the previous paragraph but keeping χ as the free parameter and considering the smallest detectable power, which is assumed to be limited by the thermal noise. The expected exclusion of an experiment with these characteristics is $\mathcal{O} \sim 10^{-8}$ and can be seen highlighted in Fig 5.2.

[1]With the signal power being small enough that it may be within the sub-quantum regime it may be a concern that resonant regeneration will not works with less than one photon in the resonator however it have been shown that resonant regeneration is still effective[77].

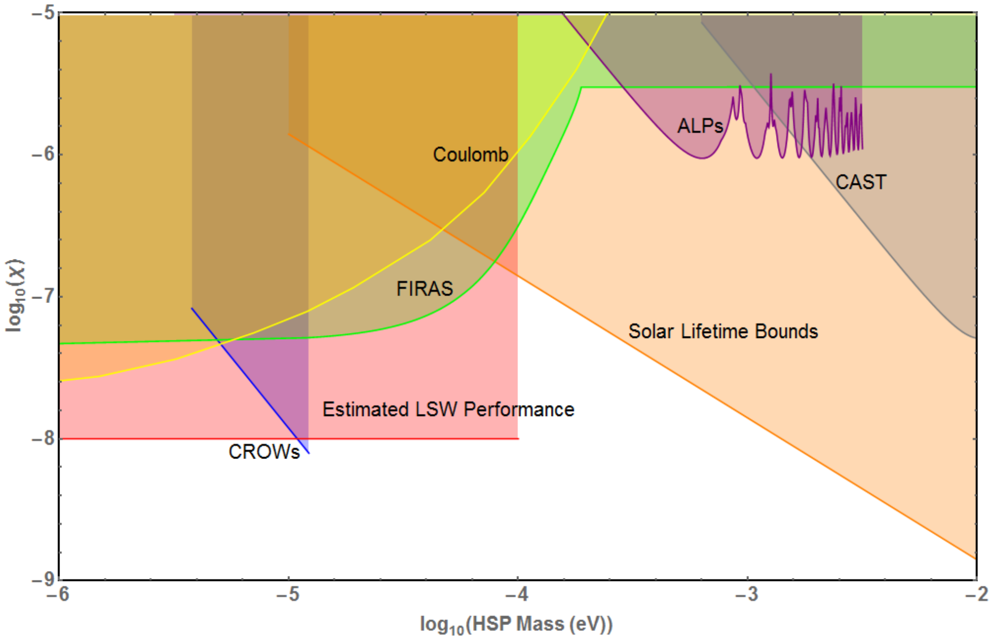

Figure 5.2: The low-mass region of the parameter space of the HSP. The green exclusion is based on far infra-red astronomy, yellow is from tests of the Coulomb force, purple is from the ALPs experiment, grey is from the CAST experiment, orange is from stellar lifetimes, blue is from the CROWs experiment and red the is potential exclusion for a microwave LSW based on the assumptions made in Section 5.2.

5.3 Cavity Design

There are a number of design decisions when it comes to designing a cavity: the operational mode, frequency, material and the cavity shape. The decision over material and shape were made on a financial basis limiting the design to a pillbox and the material to copper without any special treatments. The frequency was chosen to be 1.3 GHz to match upcoming testing of superconducting cavities developed for the International Linear Collider. The TM010 mode was chosen as it maximise the volume of the cavity for HSP generation and detection at the desired frequency. This large volume is reflected in the high G-factor for this mode as can be seen in Fig 5.3 where different modes are shown to have optimal G-factors at different HSP masses. When integrating across the mass range the TM010 mode has the highest G-factor, and a summary of the other modes can be found in Table 5.1.

TM mode	$\int$G
010	0.737
110	0.567
011	0.508
111	0.301
020	0.447
120	0.359
220	0.276

Table 5.1: Integral of the G-factor for analytic cavity modes.

The cavities were designed using CST Microwave Studio to optimise the TM010 mode at 1.3 GHz. The internal dimensions were simulated using CST as a void in an infinite metal block as the mode will only see the internal surfaces and the external dimensions of the cavity were designed based on engineering needs. Since the operational frequency was known the inner radius of the cavities

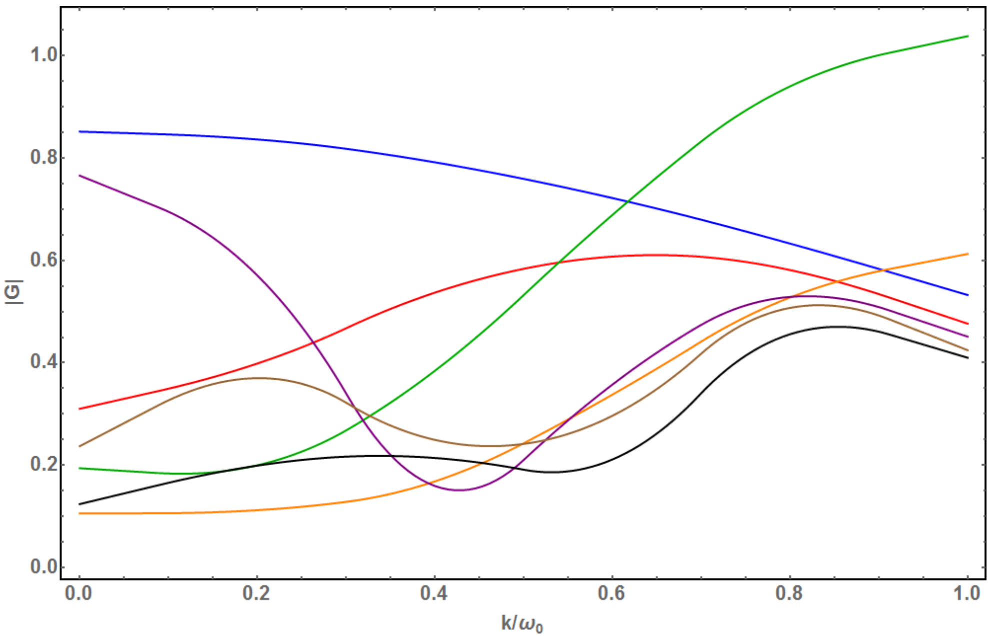

Figure 5.3: The G-factor as defined in Eq 4.25 for the TM010(blue), TM110(red), TM011(green), TM111(orange), TM020(purple), TM120(brown) and TM220(black) modes. The higher the G-factor the more sensitive the experiment is to HSPs at the given mass.

was optimised at 88.3 mm through simulations using CST Microwave Studio. In RF engineering there is an empirical rule that the radius and length of the cavity should be approximately equal otherwise the fundamental mode may not be the TM010(too long) or will suffer from multipactor effects[1](too short). Taking this into account, the inner height was set to 80 mm. Using loss parameters which correspond to pure copper a maximum Q of 22905 at room temperature was calculated.

When the cavities were manufactured a number of holes for instrumentation ports were included to allow vacuum and couplers to be fitted: their positions can be seen in Fig 5.5. Since the ports would already introduce RF leaks into the cavities, it was deemed unnecessary to include the appropriate fittings for a sacrificial seal or ‘spring fingers’ to seal the cavity lids.

A brass screw was fitted in the top plate of the cavity. Turning the screw varied the amount that it penetrated the cavity and therefore the amount that the field is distorted to be altered. The distortion shifts the resonant frequency of the cavity allowing the cavities to be tuned to the same frequency. To achieve the maximum Q factor a firm metal-to-metal contact between the screw and the cavity plate was needed. A brass nut was fitted to the screw so it could be held under tension.

The tuning range for the cavities was measured by taking a $S_{1,1}$ measurement which measures the voltage reflection from the input port. It was found that both cavities had approximately a 15 MHz range and the results are summarised in Table 5.2.

[1]The multipactor effect occurs between two metal surfaces where a resonance between the electron flight time and the RF field causes an exponential multiplication of electron emission and can cause damage to the surface of the metal.

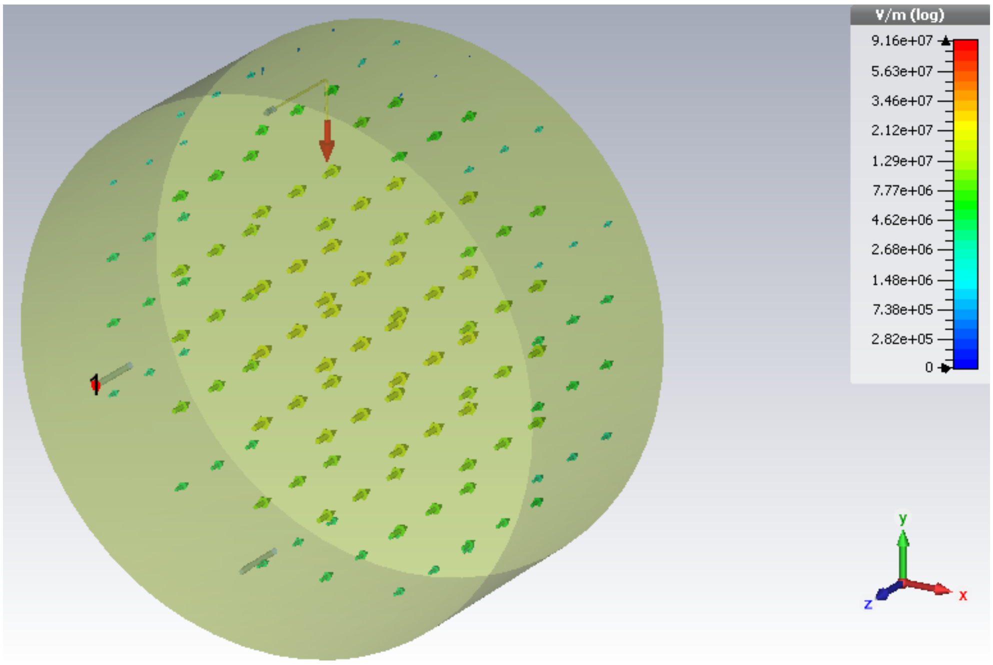

Figure 5.4: A screen capture of a CST Microwave studio simulation of the CASCADE cavities. The direction of the arrows shows the direction of the electric field. The colour and size of the arrows indicates the field strength.

	Minimum Frequency(GHz)	Maximum Frequency(GHz)	Range(MHz)
Emitter Cavity	1.2842	1.2994	15.2
Detector Cavity	1.2848	1.2998	15

Table 5.2: Tuning range of the cavities used in phase 1 of the CASCADE experiment.

5.3.1 Initial Cavity Layout

The positions of the ports in the cavity can be seen in Fig 5.5. In the initial arrangement of the cavity the coupler was fitted to Port 1, the input cable was connected to Port 3 and the cable to the readout chain was connected to Port 4. With the coupler port having been chosen the coupler was designed to maximise the loaded Q factor Q_l, of the cavity and various coupler designs were tested with both probe and loop designs. Due to the unusual placement of the coupler, the optimum solution was to use a large loop which coupled to the magnetic

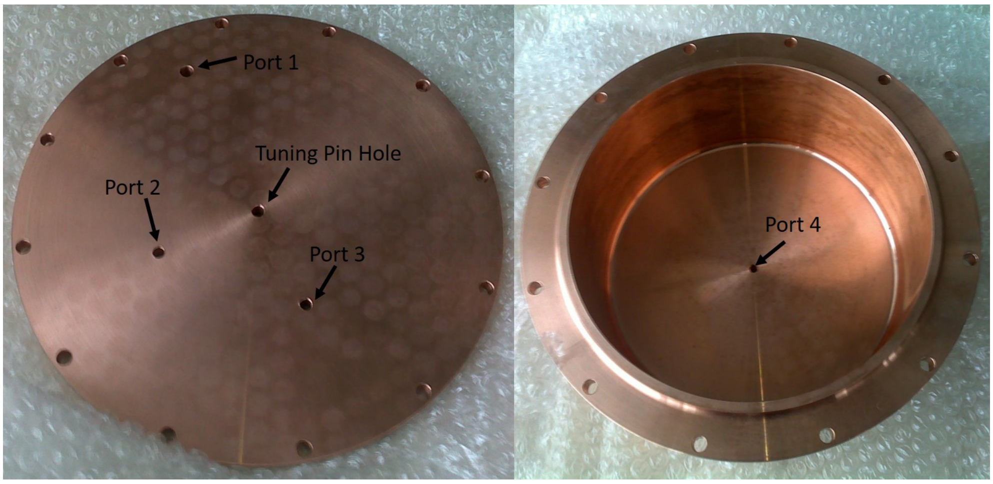

Figure 5.5: The copper cavities used in CASCADE phase 1 with the ports labelled. Since they are all of the same dimensions their use can be changed. The tuning pin hole was threaded so that a brass bolt could be used to tune the cavity.

component of the resonant mode. The coupler design was completed in CST Microwave Studio. Due to the coupler placement a large loop coupler gave the optimum solution. A cross-section of the cavity simulation including the coupler can be seen in Fig 5.6. When the Q-factor for the cavities was measured Q_l was found to be approximately 4000, this was much less than should have been achievable with the cavities. Further investigation showed that the cavity was over-coupled which leads to a reduced Q_l. To achieve the maximum Q-factor, critical coupling was required[1] and this necessitated moving the coupler to a location where either the electric or magnetic field is maximal.

5.3.2 Final Cavity Layout

The final design was based primarily on the coupling needs. The first decision was whether to couple through the electric or magnetic fields. In the TM010 mode the

[1]A further discussion of this can be found in Appendix **??**

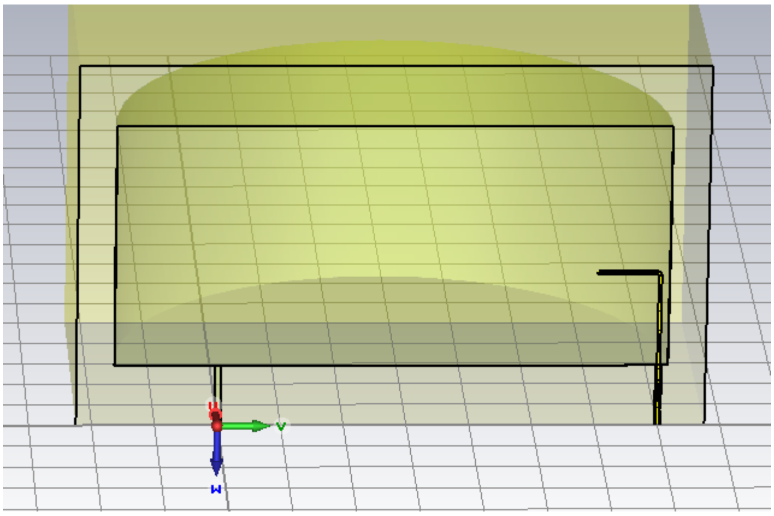

Figure 5.6: A CST Microwave Studio simulation of a CASCADE cavity with the loop coupler on the right. The yellow area is copper with the void inside being vacuum.

electric field is concentrated in the centre of the cavity and the magnetic field is around the edge; this means either a loop coupler on or near to the wall or a probe coupler in the centre of either the lid or the base could be used. The loop couplers used for magnetic fields tend to be larger and need to penetrate further into the cavity making them less stable than the probe couplers used for the electric field. Port 4 was in a central location which allowed strong coupling to the electric field and so a probe coupler was designed for this port. The central positioning was not an issue as there was a 700 MHz frequency separation between the fundamental mode and the next mode so there was no chance of exciting unwanted modes.

Off-the-shelf SMA panel mounts[78] were suitable to be used as probes and could be trimmed to the required length. CST was used to simulate probes of various lengths, however since the exact material properties of the copper used in the cavities and the brass pin were not known the result only gave an approximate guide to the length required. The panel mounts in their original form were over-

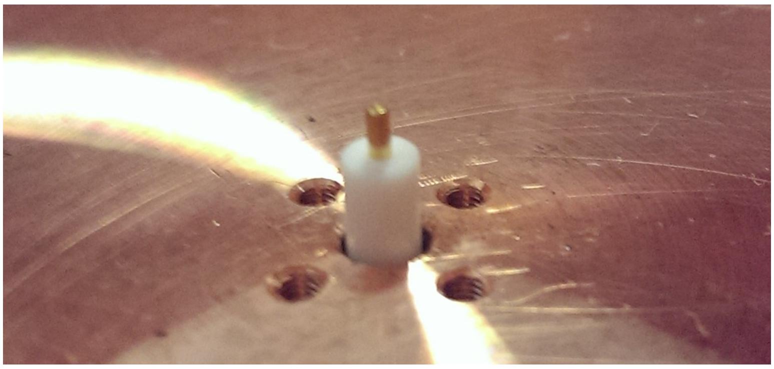

Figure 5.7: The critically-coupled coupler in the base of the CASCADE cavity. It was produced using off-the-shelf SMA panel mounts.

coupled to the cavity. The coupling was reduced by shortening the length that the coupler protruded into the cavity. The mounts were of standard dimensions which permitted multiple tests to find the correct length for the coupler. Fig 5.8 shows the results of multiple coupler tests. The $S_{1,1}$ measurement is at a minimum when the cavity is critically coupled because the power enters the cavity and is then lost to heating in the walls.

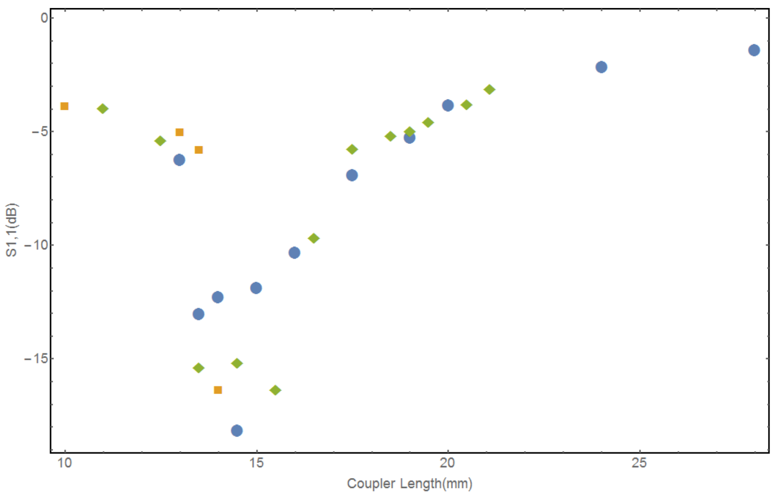

Figure 5.8: A graph of the reflection coefficient measured by the $S_{1,1}$ measurement from a network analyser for different length couplers in the CASCADE cavities. The different symbols represent the results from multiple tests but all show a minimum between 14 mm and 15 mm.

Finally to minimise RF leakage the number of ports needed was re-assessed:

- By moving the coupler to the port through which the power was injected rather than coupling through the surface currents in the walls of the cavity. This left one of the ports unused.

- The port for the vacuum system was also reconsidered but there were concerns over liquified gasses when the cavity was cooled to 77 K. The volume of the cavity is $1.96 \times 10^{-3}\,\mathrm{m}^3$. Assuming that the gas inside the cavity is all nitrogen corresponds to $2.82\,\mathrm{cm}^3$ of liquid nitrogen. The relative permittivity of liquid nitrogen is 1.538 at microwave frequencies[79] making its effect on the resonant modes of the cavity negligible. Pumping down the vacuum box would leach air from the cavities further reducing the amount of liquid gas in the cavity. Due to these reasons it was decided that the vacuum port was no longer needed.

- To monitor the resonance of the cavity while the cavity cools and the frequency shifts due to contraction without interacting with the amplifiers at cryogenic temperatures a second coupler was needed. This second coupler needed to be strongly under-coupled so any power produced from HSP interactions would be be picked up by the readout chain rather than the resonance monitoring port.

- Any unused ports were covered with a copper plate.

The layout of the cavity and changes made to it are summarised in Table 5.3.

Port Number	Initial Use	Final Use
1	Loop coupler	Under-coupled coupler
2	Vacuum valve	Blocked
3	SMA Power In	Blocked
4	SMA Power Out	Critically-coupled coupler

Table 5.3: The use of CASCADE cavity ports in the initial and final states. Blocked ports were covered with copper plates.

5.4 Signal Analyser

To collect the data from CASCADE an Agilent Technologies EXA Signal Analyzer, model N9010A[80] with the VSA 89601 software installed[81] was used. The EXA was capable of recording both time and frequency domain signals. The sensitivity of the EXA was quoted as $2.00 \times 10^{-18}\,\mathrm{W\,Hz^{-1}}$[81], this was confirmed by the noise floor observed when testing the EXA. A sample of the noise is shown in Fig 5.9 which corresponds to a noise power of $6.31 \times 10^{-19}\,\mathrm{W\,Hz^{-1}}$.

Using the VSA software a time-domain signal can be recorded for up to 3000 s which once Fourier-transformed gives a maximum frequency resolution of 0.5 mHz. In Section 5.2 the signal strength was estimated to be 10^{-20} W and therefore for a frequency resolution of 0.5 mHz, 50 dB of amplification was required to bring the signal strength above the internal noise of the EXA. Since longer data runs would reduce the effect of random fluctuations in the noise, data from multiple runs was combined by taking the root mean squared for each frequency bin.

5.5 Amplifier Testing

Two Miteq ASF3 amplifiers(Fig 5.10)[82] were used as part of the read out chain. A Mini-Circuits ZHL-1217HLN(Fig 5.11)[83] amplifier was used as a power am-

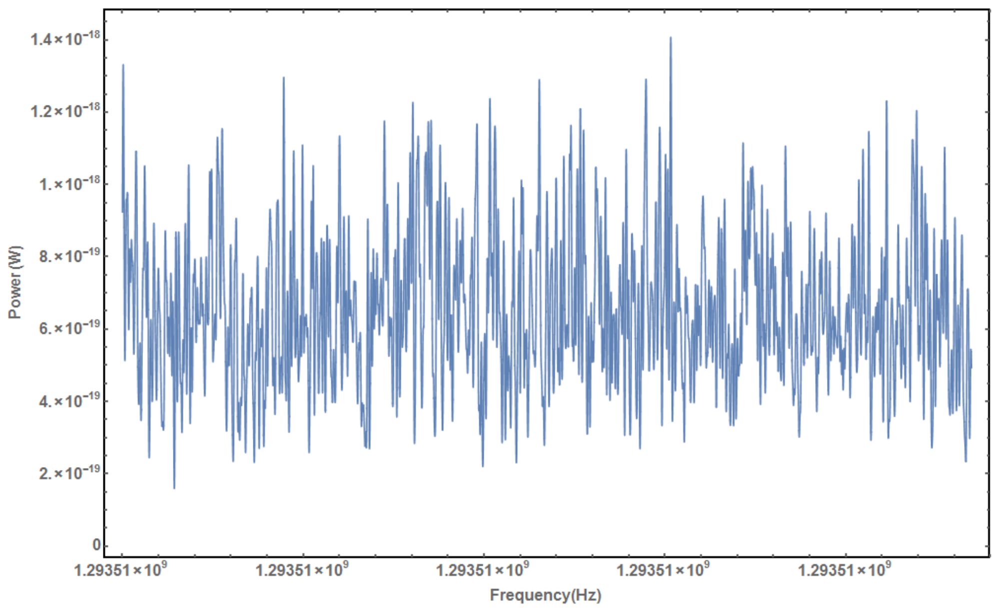

Figure 5.9: A sample of the internal noise power of the EXA signal analyser used in the CASCADE experiment.

plifier for the emitter. The amplifiers all needed to be characterised and since the amplifiers all needed to be tested in the same manner a standard set-up was used as shown in Fig 5.12.

Two measurements needed to be performed for the amplifiers: amplification flatness against frequency and input power against output power. The frequency response of the amplifiers was only of interest over the operational frequency of the cavity. Since the frequency range of interest is only 15 MHz, differences in the frequency response was found to be undetectable within the noise of the network analyser.

The amplification with respect to input power was perhaps the most important feature to characterised as it not only showed that the amplifiers were behaving as expected but also showed that the readout chain is capable of detecting signals as small as 10^{-20} W. To test this, the input power was started at an easily-observable

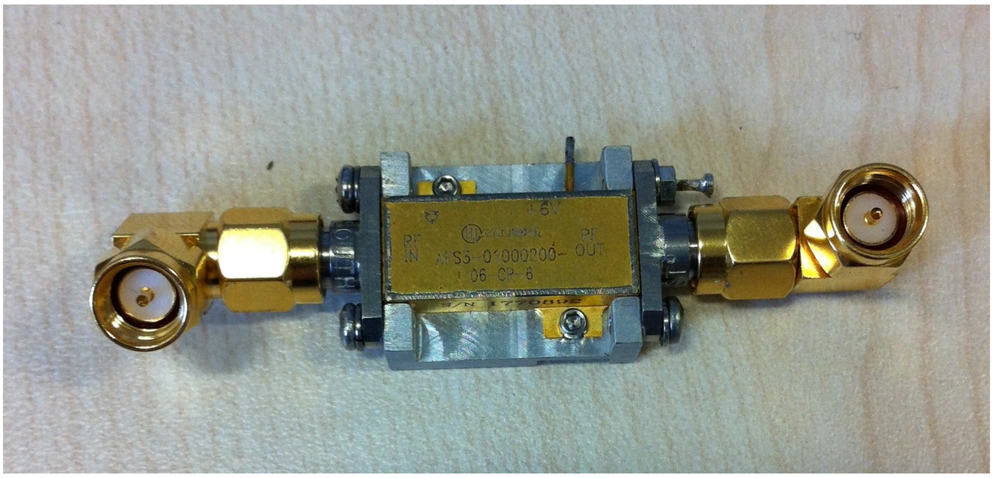

Figure 5.10: One of the Miteq ASF3 amplifiers which were used as a amplifiers in the readout chain for CASCADE.

Figure 5.11: The Mini-Circuits ZHL-1217HLN which was used as a power amplifier between the signal generator and the emitter cavity of CASCADE.

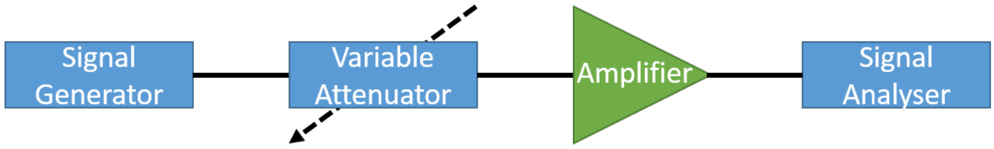

Figure 5.12: A schematic of the order of components used to test the amplifiers for CASCADE.

power and reduced by 10 dB at a time with the amplification results being shown in Fig 5.13. Both amplifiers showed an increase in the amplification at low powers which could in part be due to leakage between the signal generator and the EXA, therefore the minimum observed amplification was used for calculations. To reach the expected signal strength two amplifiers were needed so both amplifiers in series were tested in the same manner. In Fig 5.14 it can clearly be seen that the amplifiers operated at the target signal power of 10^{-20} W with 70 dB amplification taking the signal power above the internal noise of the EXA.

5.6 Experimental Set-Up

Due to the expected signal power being very low, great care needed to be taken to ensure there was no conventional coupling between the emitter and the detector sections of the experiment. To do this the experiment was set up in such a way that the two parts were entirely separate as can be seen in Fig 5.15.

On the emitter side is a Rohde & Schwarz SM300 Signal Generator[84] which was connected through the emitter's aluminium Faraday cage to the Mini-Circuits ZHL-1217HLN[83]. This was then connected using semi-rigid coaxial cables through a copper shielding box to the cavity. The output of the Mini-Circuits amplifier provided 30 dB of amplification but saturated at a maximum power

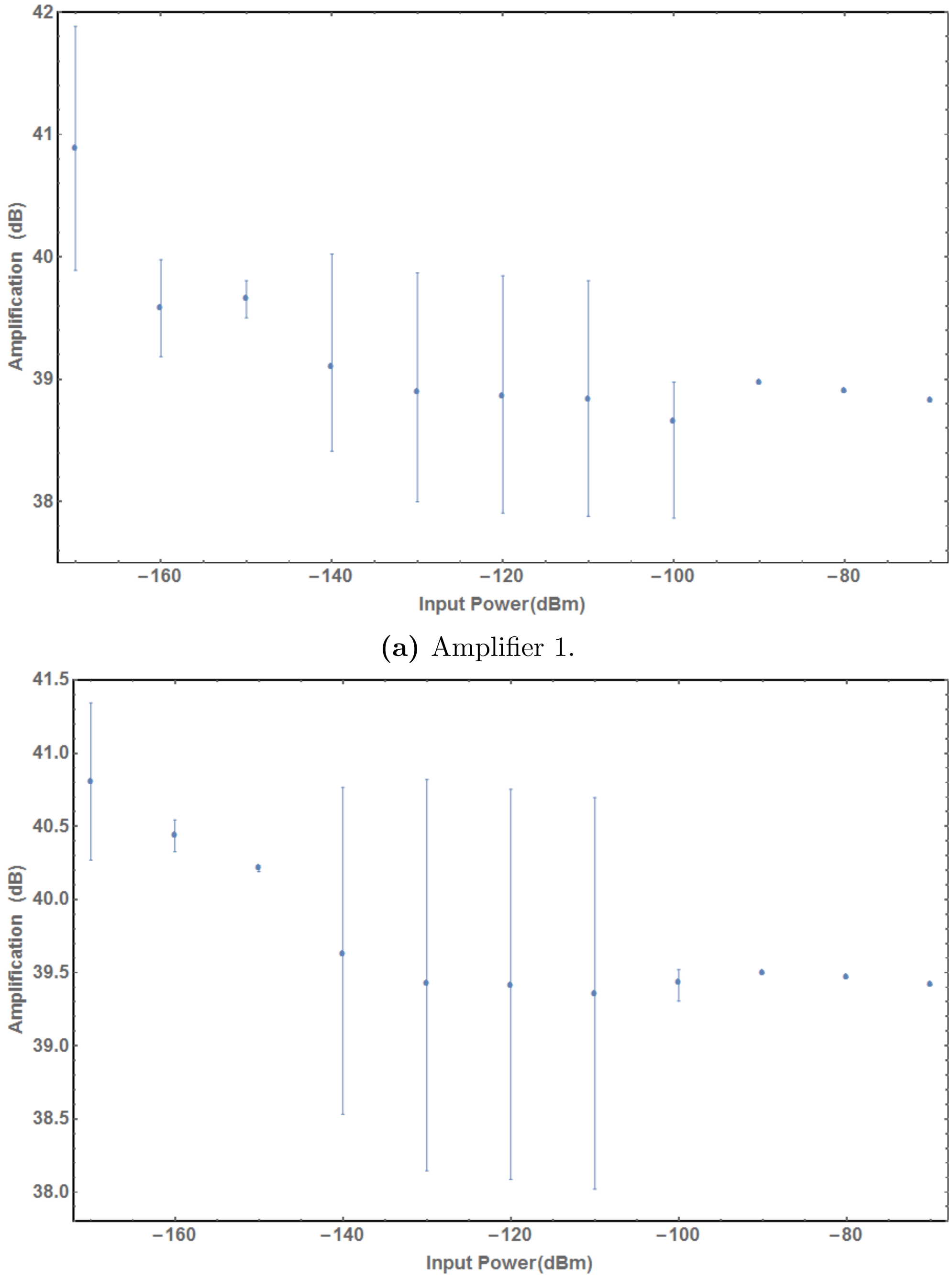

(a) Amplifier 1.

(b) Amplifier 2.

Figure 5.13: The detector side amplifiers responses to different input powers. The power is measured in dBm where 1 dBm=1 mW. The error bars show the full range of results from multiple measurements.

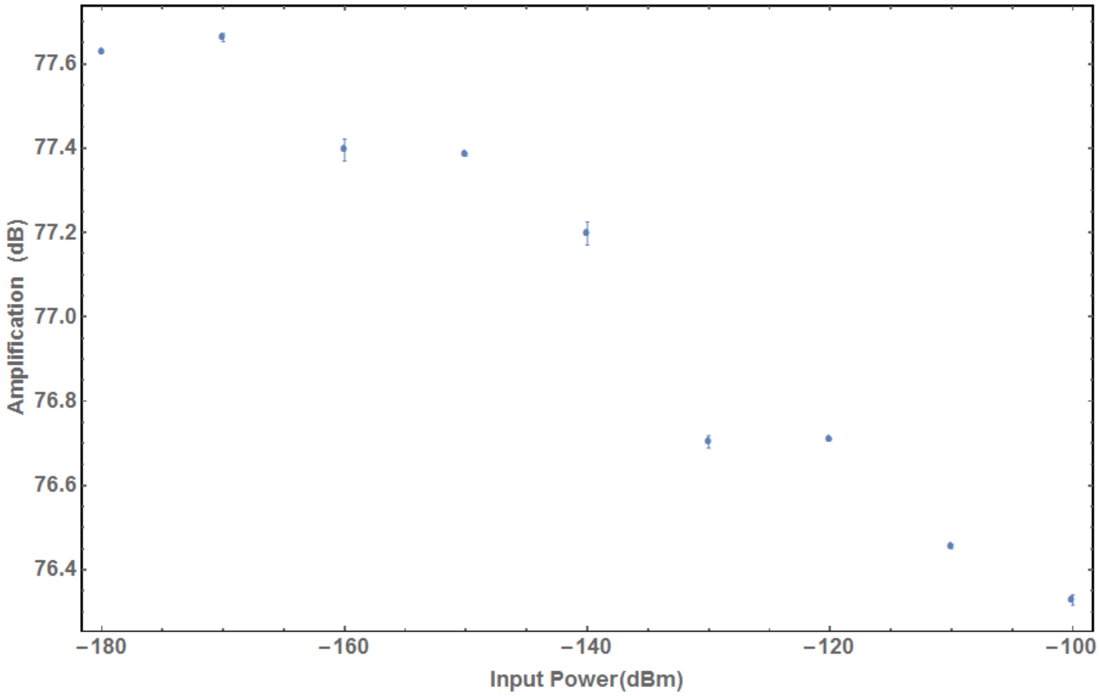

Figure 5.14: The response of both detector side amplifiers in series to different input powers.The power is measured in dBm where 1 dBm=1 mW. The error bars show the full range of results from multiple measurements.

output of 0.40 W. Due to this, the signal generator was operated at 4×10^{-4} W so that the power outside of the Faraday cage was kept to a minimum while still providing the cavity with the maximum possible power.

On the detector side of the experiment the cavity was connected though a copper shielding box to the Miteq ASF3 amplifiers, each of which were held in their own copper shielding boxes. The amplifiers were then connected to a vacuum feed-through and then to the EXA. This whole arrangement was wrapped in aluminium foil to reduce the possibility of the cables picking up any interference. All the seals on the vacuum box were covered with copper tape on the outside of the gasket to minimise RF leakage.

Photographs taken during the construction and operation of the CASCADE experiment can be found in Appendix B.

Anything which can affect the dimensions of the cavity will have an effect on the resonant frequency of the cavities. When the cavity changes temperature, the internal cavity dimensions will alter. Therefore it was important to control the environment in which the experiment took place. The laboratory had a simple climate control system but it was unable to create a stable temperature so an Arduino mirco-controller[85] was used to monitor the temperature and act as a veto when the temperature change would de-tune the cavities. It was found that maintaining a cool temperature would produce a stable environment since the experiment took place over the winter. Fig 5.16 shows a trial run which was performed from 23/12/14 to 07/01/15 in which a stable temperature of 17 ± 1^{o}C was reached.

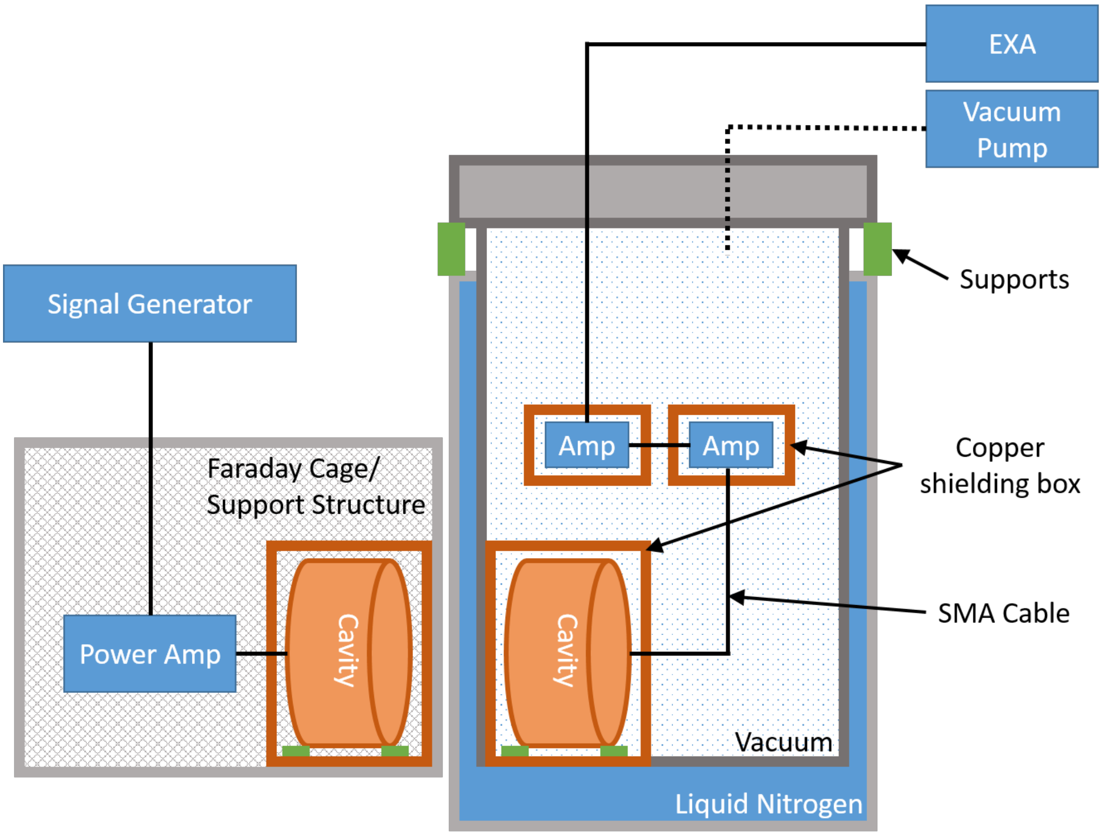

Figure 5.15: A schematic diagram of CASCADE. The emitter section is on the left and the detector on the right. The orientation of the cavities shown here is the same as that which was used in the physical experiment.

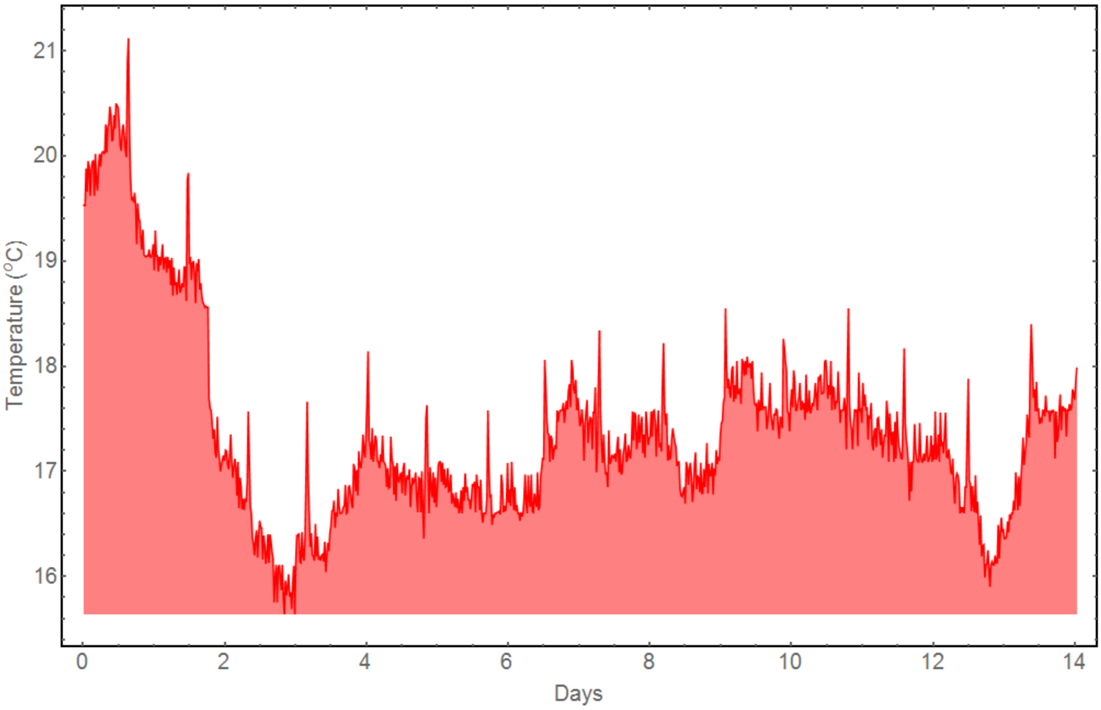

Figure 5.16: A sample of the temperature log for the laboratory housing the CASCADE experiment from 23/12/14 to 07/01/15. The temperature of the climate control was set to 17^{o}C and it can be seen that after a stabilisation period, the temperature remained stable within $\pm 1^o$C.

5.7 Data Acquisition

Anticipating the need to run the experiment multiple times to ensure there were no RF leaks in the shielding, a standard measurement procedure was established.

1. Put tuning screw into central position and secure to ensure metal to metal contact.

2. Fit the detector cavity into its shielding box utilising a spacer to avoid affecting the tuning screw. Pad edges with foam to minimise movement within the shielding box. Secure the lid in place with copper tape to limit leakage.

3. Position the detector cavity in the base of the vacuum box and take a $S_{1,1}$ measurement to find the resonant frequency of the cavity.

4. Connect up the amplifier chain and attach to the vacuum box feed-through.

5. Seal the vacuum box and cover the seals with copper tape.

6. Set emitter frequency to that of the detector cavity and seal in its shielding box.

7. Position on the Faraday cage mount and take a $S_{1,1}$ measurement to ensure the resonance hasn't shifted.

8. Connect the power amplifier to the emitter cavity and seal the Faraday cage using copper tape to minimise leakage.

9. Set the signal generator to the resonant frequency.

10. Set the vector signal analyser to the resonant frequency and the resolution bandwidth to its minimum value of 0.5 mHz.

Before a data-taking run was performed, checks were needed to test that the detector chain was working correctly and that there were no RF leaks. The detector chain was tested by intentionally leaking signal through the vacuum box by opening a flange and recording 3 ks of 0.5 mHz resolution data.

In Fig 5.17a it can clearly be seen that there is a spike at the signal frequency. The signal generator was left unchanged but the vacuum box was sealed to test the shielding. Fig 5.17b shows that the signal spike from Fig 5.17a has been reduced to the point that it is indistinguishable from noise.

Following successful checks, a data run was completed on 8th of January 2015 for 10 hours with a temperature variation within an acceptable range as shown in Fig 5.18. with a signal frequency of 1.29353940 GHz and is displayed in Fig 5.19. This data shows no obvious peak, and so can be used to set an exclusion on the HSP parameters as explained in Section 5.8.

5.8 Data Analysis

To set an exclusion based on the 08/01 run the sensitivity of CASCADE needed to be calculated. The limit on CASCADE's sensitivity comes from the noise in the signal region. In Section 5.2 the noise in the cavity was estimated by using Eq 4.34; however since the signal region only takes up a small section of the recorded data, the side-bands can be used to estimate the noise inside the signal region.

To ensure that no signal was included in the noise calculation a 2 Hz window

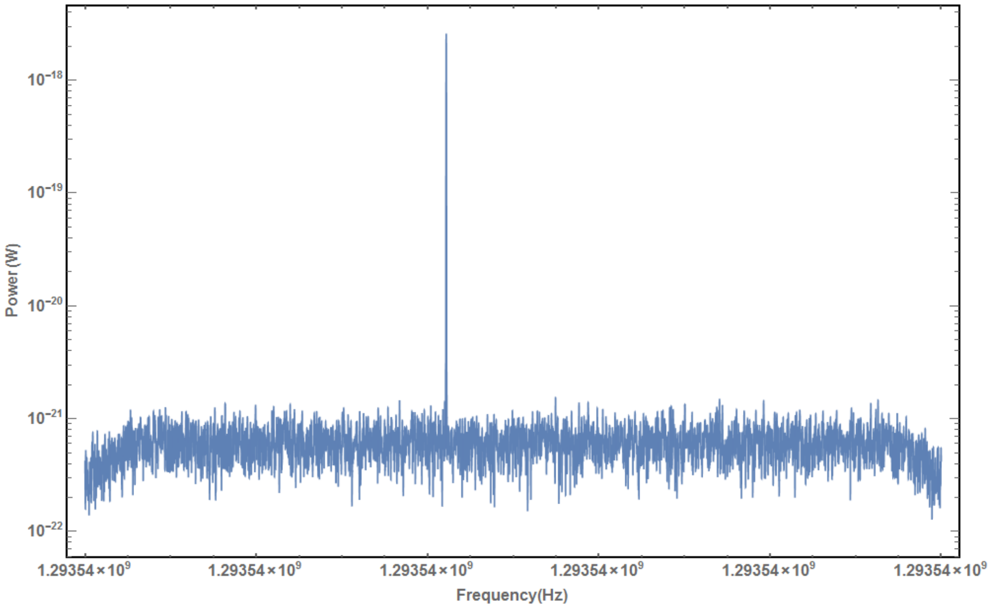

(a) Open vacuum box.

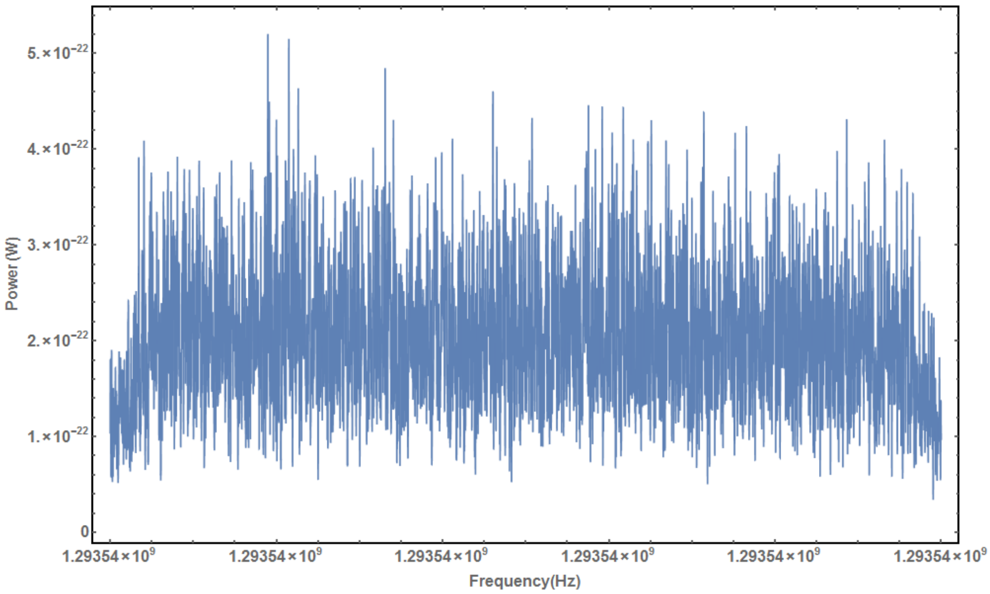

(b) Sealed Vacuum box.

Figure 5.17: The results from pre-run tests of the CASCADE experiment. The sensitivity test was conducted by opening a vacuum flange and therefore removing a layer of shielding and a signal spike can clearly be seen. The shielding test was performed by sealing the vacuum box to complete the shielding for which no signal can be seen.

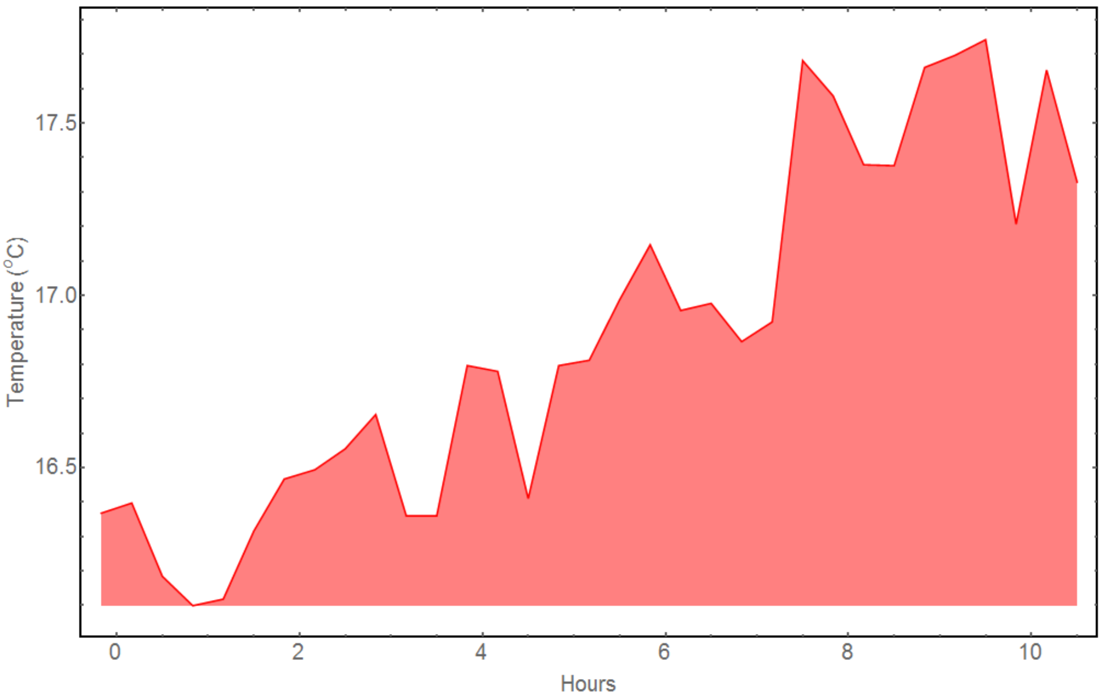

Figure 5.18: The temperature of the laboratory at 20 minute intervals taken during the CASCADE data run.

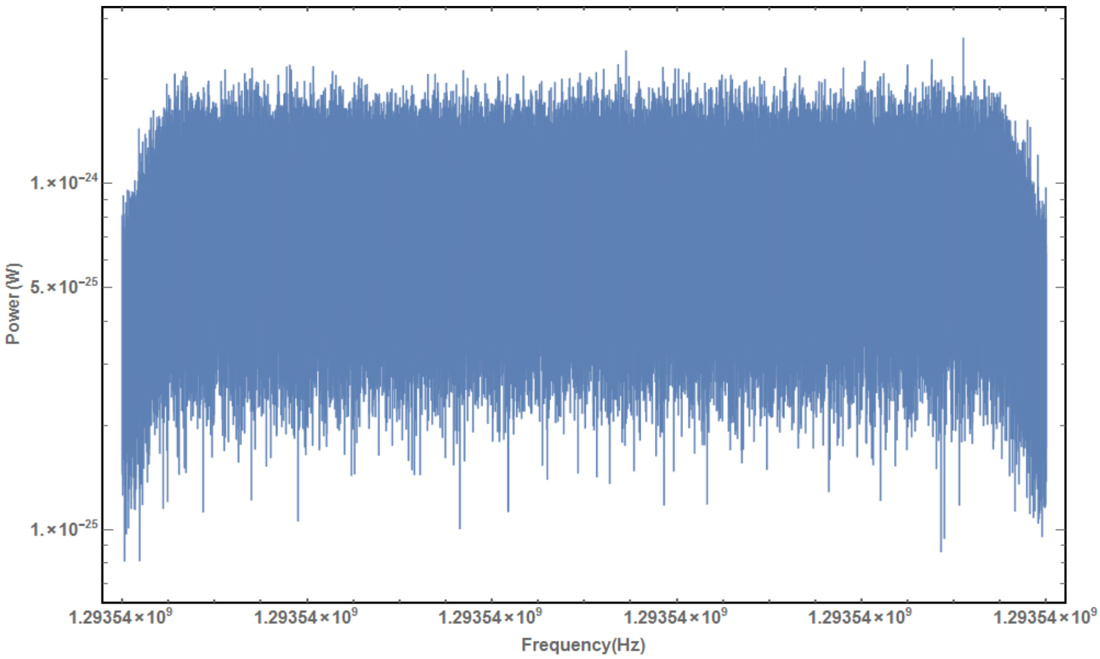

Figure 5.19: The power recorded in the frequency window of interest during the CASCADE data run.

around the signal frequency was removed. This corresponded to the removal of 4000 frequency bins from the data set which is 414187 bins in total. Since the number of bins is very high, if the uncertainty on the noise is set at 3σ standard deviations above the average, 1242 bins would exceed the uncertainty which corresponds to approximately a 2% chance of there being an excess in the signal window. This was deemed to be too high and so only an excess greater than 5 standard deviations above the mean was considered as a signal candidate. To calculate this power level the noise first needed to be binned based on the power, Fig 5.21 shows the resulting histogram. By selecting the appropriate quantile of the distribution the $5\,\sigma$ level was found to be 2.5×10^{-24} W.

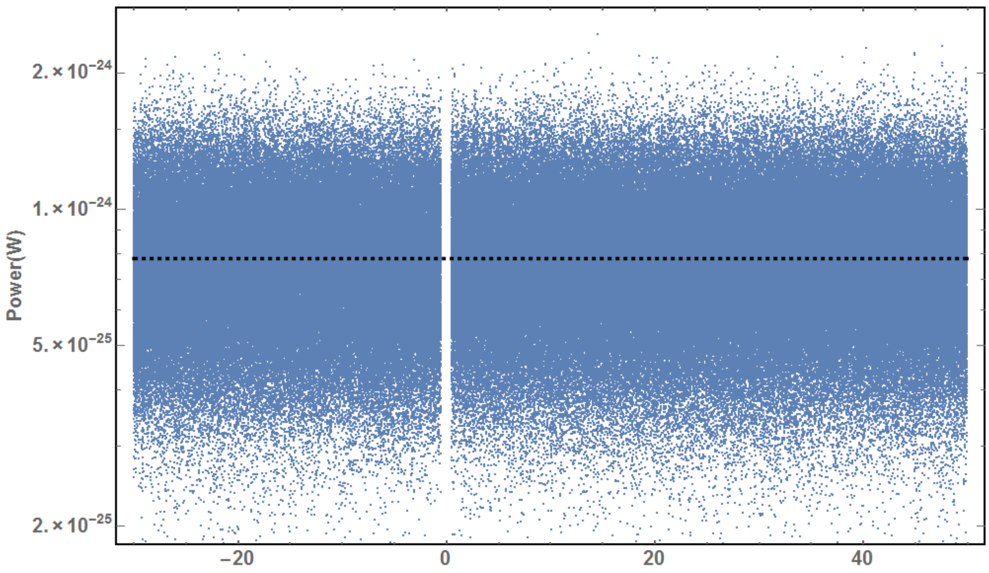

Figure 5.20: The recorded noise power in the frequency window of interest from the CASCADE data run. A 2 Hz window around the expected signal frequency has been removed and the mean power of 7.8×10^{-25} W is marked with the dashed line.

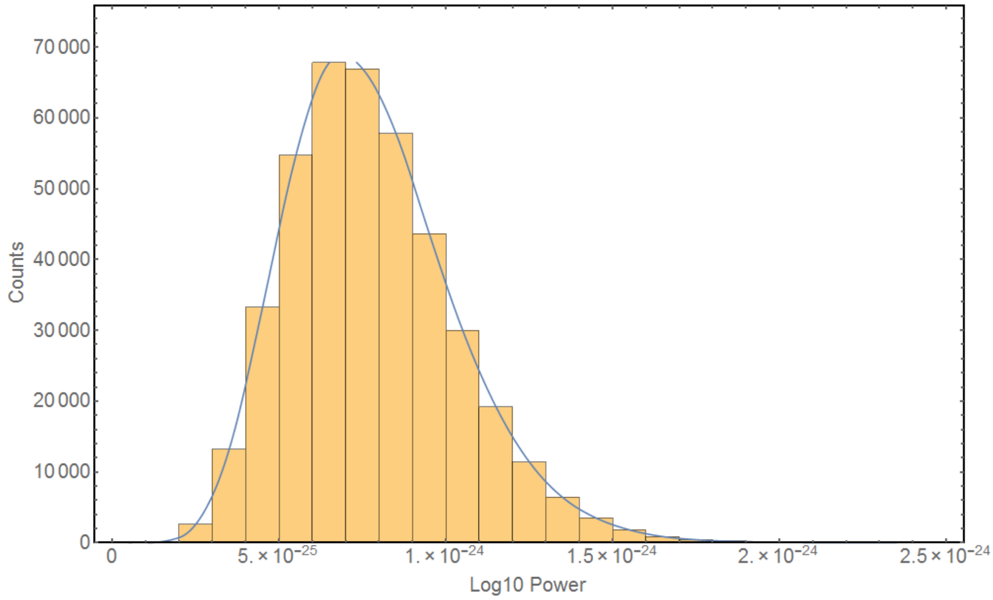

Figure 5.21: Histogram of the noise power recorded from the CASCADE data run.

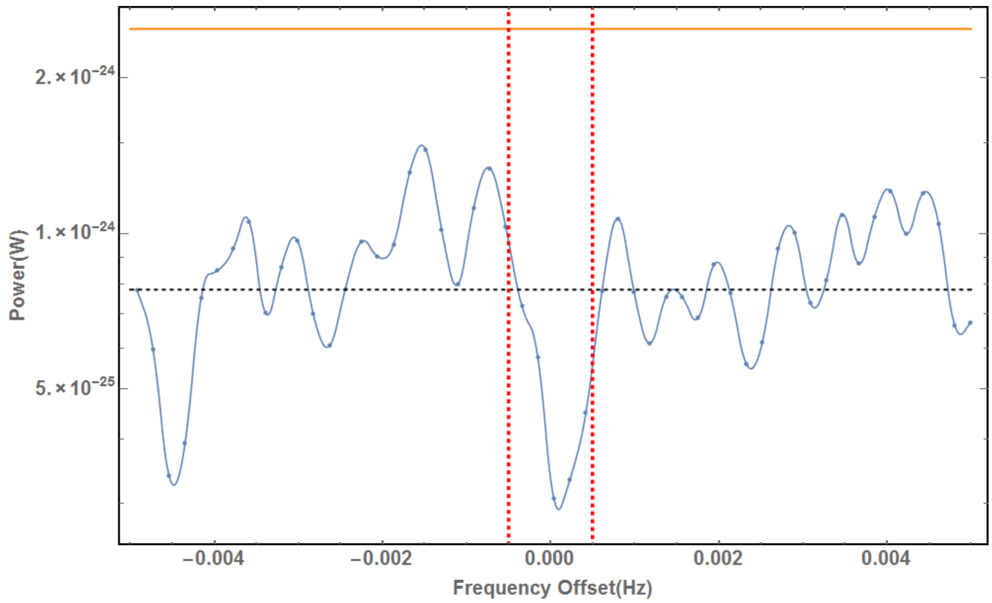

Figure 5.22: The recorded power in the signal window recorded during phase 1 of the CASCADE experiment. The black dashed line is the mean power, the orange line is the five σ level and the red dashed lines bound the signal window by 2 resolution bandwidths.

Fig 5.22 shows the signal window and it can clearly be seen that there is no excess of power 5 σ greater than the mean indicating a negative outcome for the experiment. This means the result of the experiment is an exclusion in the HSP parameter space.

In the transverse mode the expected power can be calculated by multiplying Eq 4.33 by the power of the source. Re-arranging this equation for the coupling factor gives Eq 4.29. By using the calculation of the G-factor for the TM010 as was performed for Fig 5.3 but setting the separation to 0.1 m as it was in the experiment. The exclusion for the transverse mode was calculated and is shown in Fig 5.23.

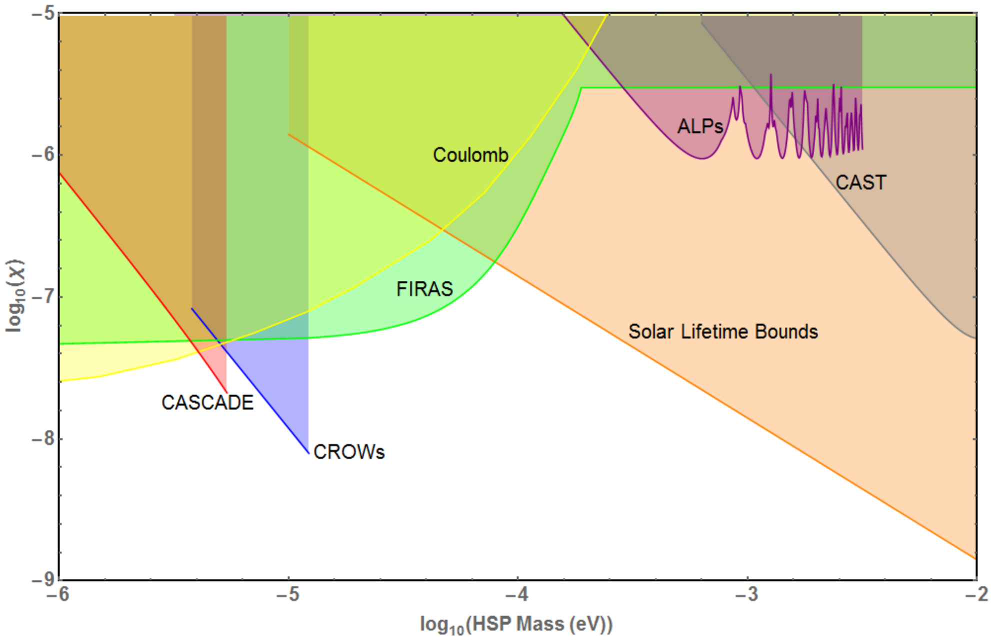

Figure 5.23: The low mass parameter space of the HSP. The green exclusion is based on far infra-red astronomy, yellow is from tests of the Coulomb force, purple is from the ALPs experiment, grey is from the CAST experiment, orange is from stellar lifetimes, blue is from the CROWs experiment and red is the CASCADE exclusion based on the transverse mode.

To calculate the longitudinal exclusion a similar approach to that of the transverse mode is taken where the ratio of the power in the signal to the power observed is used to calculate the minimum coupling that the experiment is sensitive too. For this a modified version of Eq 4.44 that uses a far field approximation of the longitudinal coupling was used. The results from longitudinal coupling are shown in Fig 5.24.

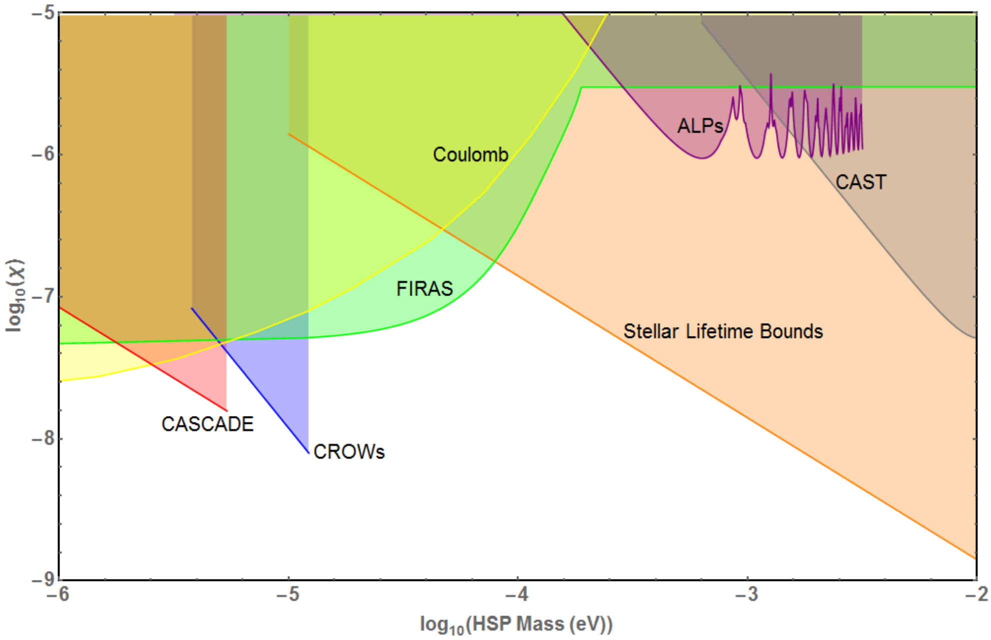

Figure 5.24: The low mass parameter space of the HSP. The green exclusion is based on far infra-red astronomy, yellow is from tests of the Coulomb force, purple is from the ALPs experiment, grey is from the CAST experiment, orange is from stellar lifetimes, blue is from the CROWs experiment and red is the CASCADE exclusion based on the longitudinal mode.

Chapter 6

The PHARAOH Experiment

6.1 PHARAOH Overview

As discussed in section 2.3.2, the hidden sector photon has no preferred mass region meaning that any mass range that can be probed, should be. By using the light shining through a wall technique with existing laser and RF technologies it is possible to probe the HSP-photon coupling within the optical and microwave regimes respectively. Due to limitations in the Q-factor of microwave cavities with frequencies beyond 10 GHz it is difficult to produce a conventional LSW experiment which is capable of probing the 10^{-5} to $10^{-4}\,$eV mass range. In section 3.3.6 it was shown that photonic structures possess the ability to form cavity-like structures, making the 10^{-5} to $10^{-4}\,$eV mass range accessible to LSW experiments.

6.2 Photonic Structures

The first step in designing a photonic structure is to decide the unit cell of the lattice in which the structures will be formed. There are as many different designs of photonic lattices as there are uses, however the cavity for a LSW experiment needs to be bound in 3 dimensions and therefore only 2D or 3D lattices were considered. This requirement led to four basic options: a woodpile, a diamond-like structure, square-based lattice or triangular-based lattice. Due to difficulties in coupling a signal in and out of the photonic cavities the diamond and woodpile lattices were discarded. To choose between a square and triangular lattice the reduced Brillouin zone of the lattice needed to be considered. A square-based lattice has 4-fold symmetry whereas a triangular lattice has 6-fold symmetry leading to it having a smaller irreducible Brillouin zone as shown in Fig 6.1. This means that there are fewer unique directions of propagation in the triangular lattice and therefore it is easier to produce confinement[68].

6.3 Maximising The Quality-factor

With the basic design of the structure decided the next step was to tune the lattice parameters to create a complete bandgap. Since Maxwell's equations are scale invariant the lattice constant a, was set to a value that was convenient for meshing of the simulation and to avoid non-physical negative frequencies being observed. To do this the MIT Photonic-Bands, MPB, package was used[86]. MPB works by computing the definite-frequency eigenstates for dielectric structures of infinite periodicity. This is a good approximation of a real finite structure provided the

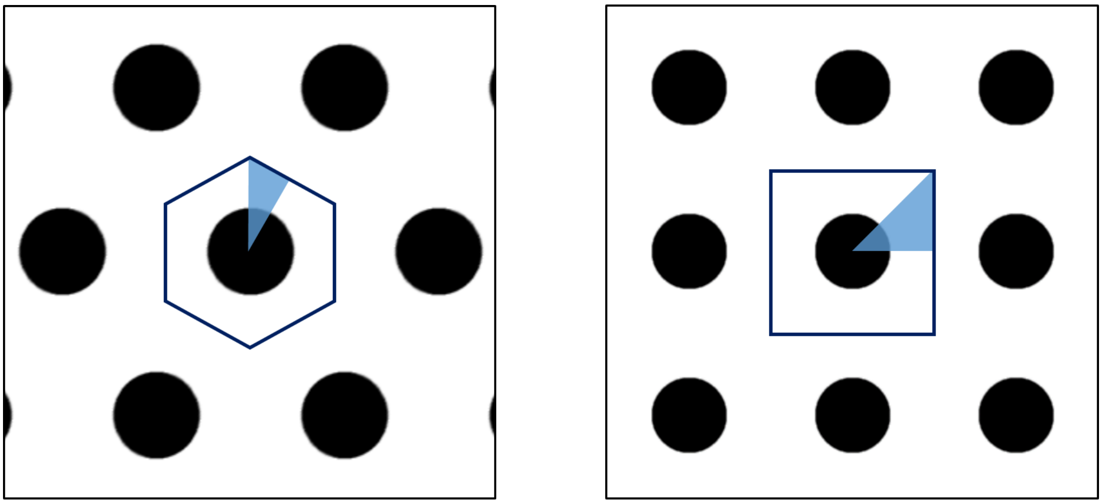

Figure 6.1: *Left*: Triangular-based reciprocal lattice with the irreducible Brillouin zone outlined in dark blue. By exploiting symmetries only the regions highlighted in light blue need to be calculated.
Right: Square-based reciprocal lattice with the irreducible Brillouin zone outlined in dark blue. By exploiting symmetries only the regions highlighted in light blue need to be calculated

size of the lattice is 10 or more lattice constants across.

Since the style of lattice had been decided based on the basic lattice properties and the lattice constant was free to scale, there were two variables that could be varied to create a bandgap: the ratio of the scatterers radius to the lattice constant(the fill-factor), and the permittivity of the dielectric ε. To investigate the bandgap of a lattice, a band-diagram was used. The band-diagram for a trangular lattice of cylindrical scatterers with a radius of 0.1 a and relative permittivity, ε, of 9 is shown in Fig 6.2. It can be seen that this has already opened up a small total bandgap slightly below 0.6 ca^{-1} and a large bandgap in the TM bands in blue. Due to the increased size of the bandgap, the TM-like states of the lattice were focused on. Fig 6.6 shows the effect of varying the permittivity and fill-factor. It shows that for small radius scatterers, between 0.1-0.2 a, a bandgap opens up as the permittivity increases. In reality the choice of material will dictate the permittivity contrast so in the rest of this section a relative permittivity of 9 will be used, which corresponds to artificially grown sapphire against an air background.

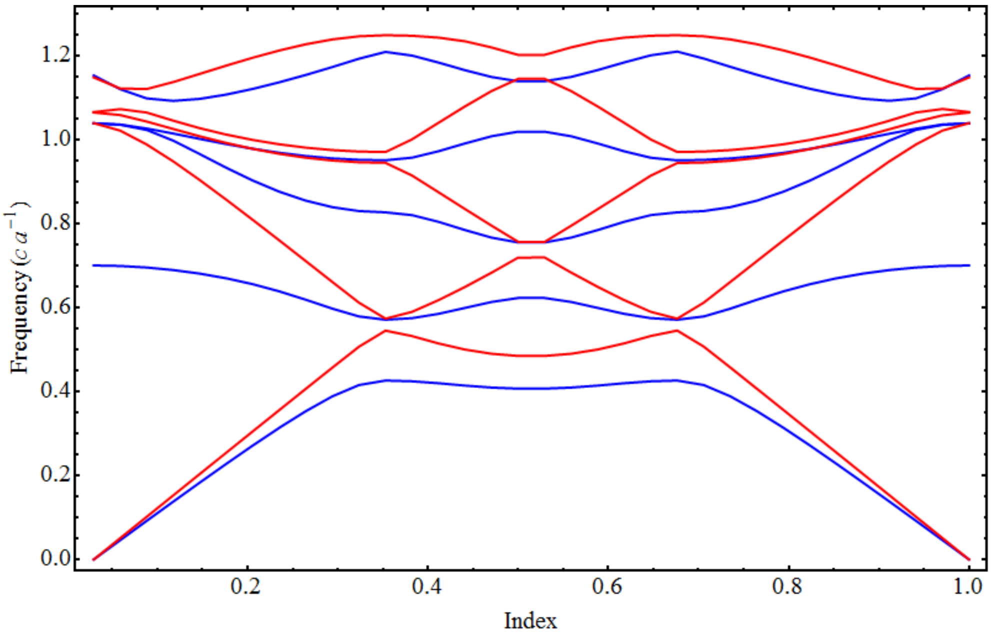

Figure 6.2: The band-diagram for a trangular based lattice of cylindrical scatterers with a radius 0.1 a and a ε of 9, simulated using MPB[86]. The TM bands are shown in blue and the TE bands in red.

The removal of a scatterer creates a resonator but there is no requirement for the resonant mode to be within the total bandgap of the structure. Since the removal of a scatterer breaks the symmetry of the lattice, eigenmode solvers are not suitable to calculate the resonant mode so a full finite-difference time-domain(FDTD) simulation of the structure was needed. The MIT Electromagnetic Equation Propagation, MEEP[87], package was used as it met our requirements and is widely used for the simulation of 2-dimensional photonic cavities[1].

[1]See papers citing [87].

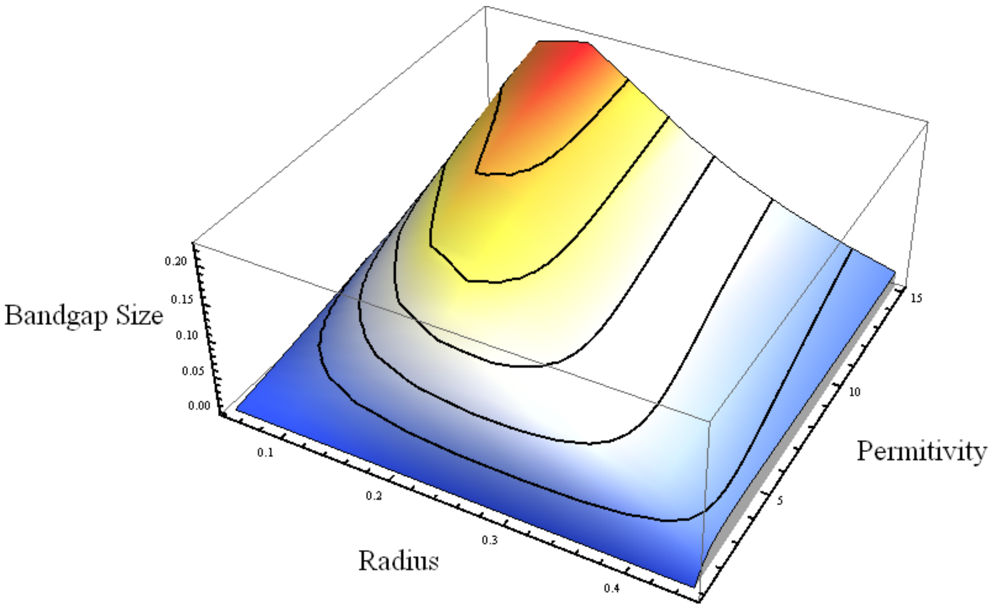

Figure 6.3: The size of the bandgap for a triangular based lattice with respect to varying the scatterer radius in units of the lattice constant a, and relative permittivity, simulated using MPB[86]. The colour varies with the bandgap size with blue being 0 and red at 0.6 in frequency units of c/a.

MEEP has an integrated spectral analysis algorithm which records the field at any given location in the simulation over a period of time and decomposes it into a series of frequencies within a user-defined bandwidth. In addition to the amplitude of a given frequency component, the evolution of the amplitude is characterised and given as a quality-factor, Q. For a resonant state in a defect, the Q-factor of the state should be of an order greater than 10^4. Fig 6.6 showed that there should be a large bandgap in a lattice with a scatterer radius of $0.2\,a$, this lattice was then probed with a range of frequencies and the maximum Q achieved is shown in Fig 6.4. There were two regions that showed resonant behaviour, the first centred on $0.42\,ca^{-1}$ and the second at $0.84\,ca^{-1}$. The first corresponded to the fundamental mode of the defect. An equivalent conventional cylindrical cavity would show a resonance at $0.5\,ca^{-1}$ which was close to the value observed.

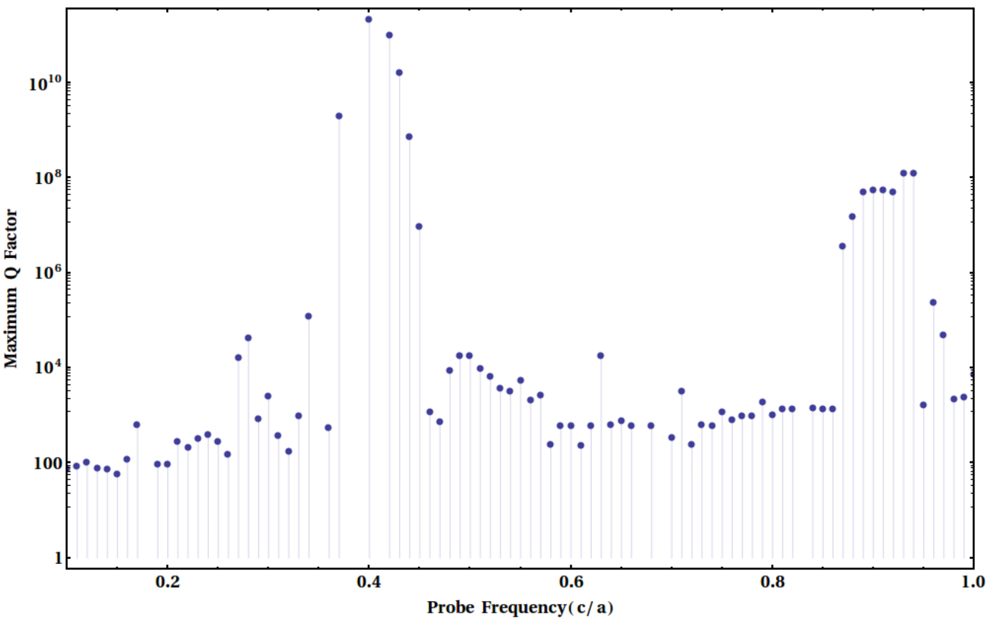

Figure 6.4: The Q-factor of the highest Q state that is excited when power is injected into the defect in a narrow frequency band around the probe frequency, simulated using MEEP[87]. There are clearly two modes visible with the first centred at 0.42 corresponding to the fundamental mode and the second centred at 0.86 being the first higher order mode.

In addition when the field profile was imaged as shown in Fig 6.5a it was clearly a localised state. The second is the first higher order state and when the field pattern is imaged in Fig 6.5b it is clear to see that despite being resonant, this state was not localised.

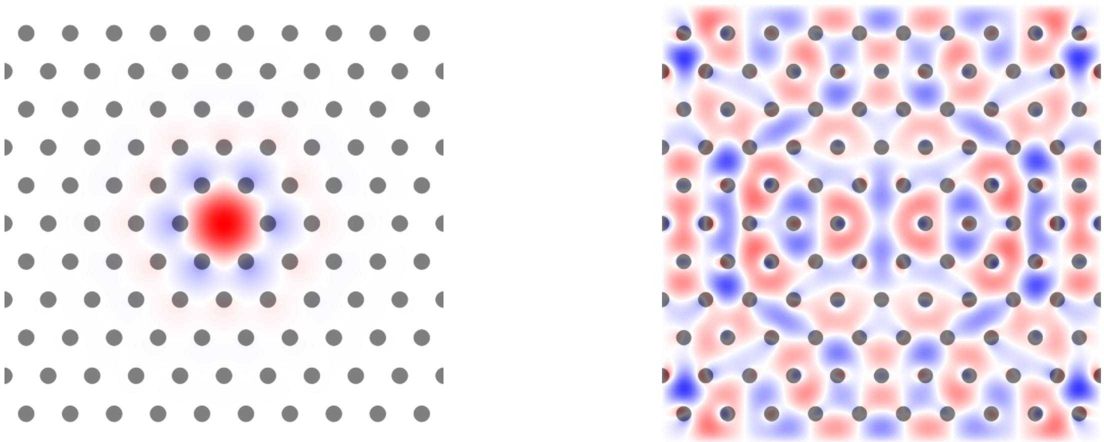

(a) Resonance at $0.42\,ca^{-1}$ **(b)** Resonance at $0.84\,ca^{-1}$

Figure 6.5: The field profiles of resonant modes in a photonic defect at high Q frequencies using MEEP[87]. The resonance at $0.42\,ca^{-1}$ is clearly a highly spatially localised state which would be expected from existing in the bandgap of the lattice. The resonance at $0.84\,ca^{-1}$ extends across the lattice indicating that it is a state over the extended lattice making it unsuitable for use in a LSW experiment.

As with the size of the bandgap, the Q-factor of the resonant mode can be tuned by changing the fill-factor of the lattice. Changing the radius of the scatterers reduces the volume of the defect and therefore increase the frequency of the resonance. In Fig 6.8 the fill-factor was varied and then the probe frequency was varied around the original resonant frequency. The maximum Q value showeds two broad maxima centred around 0.19 and 0.32 with the first corresponding to the fundamental mode of the defect and the second being a higher order mode as can be seen in Fig 6.7.

A photonic cavity with finely tuned parameters can produce Q-factors which

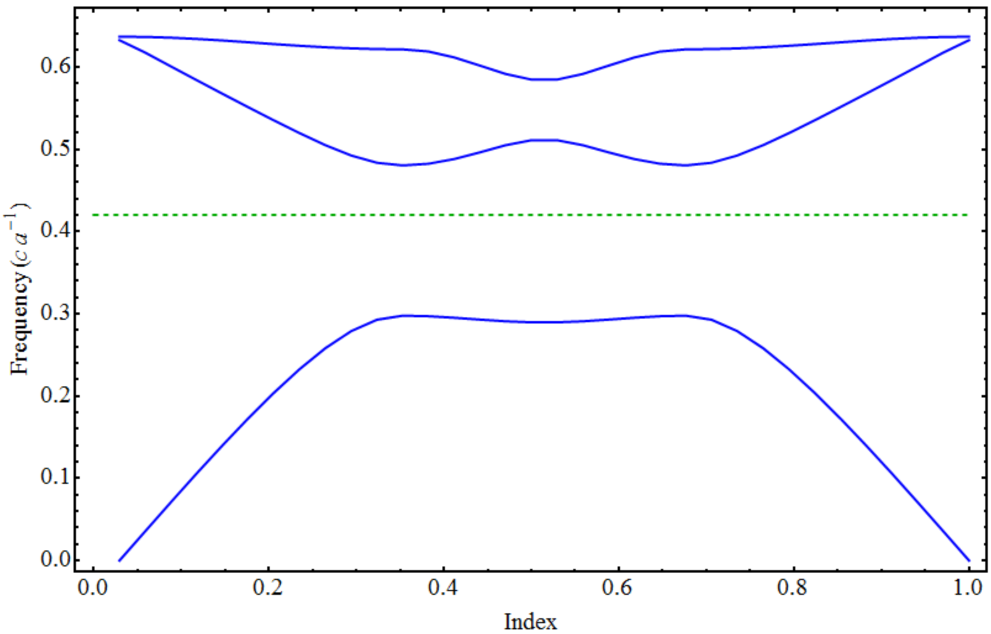

Figure 6.6: The TM band diagram of a triangular based photonic lattice with the resonant frequency highlighted at $0.42\,ca^{-1}$ with a green dashed line, simulated using MPB[86].

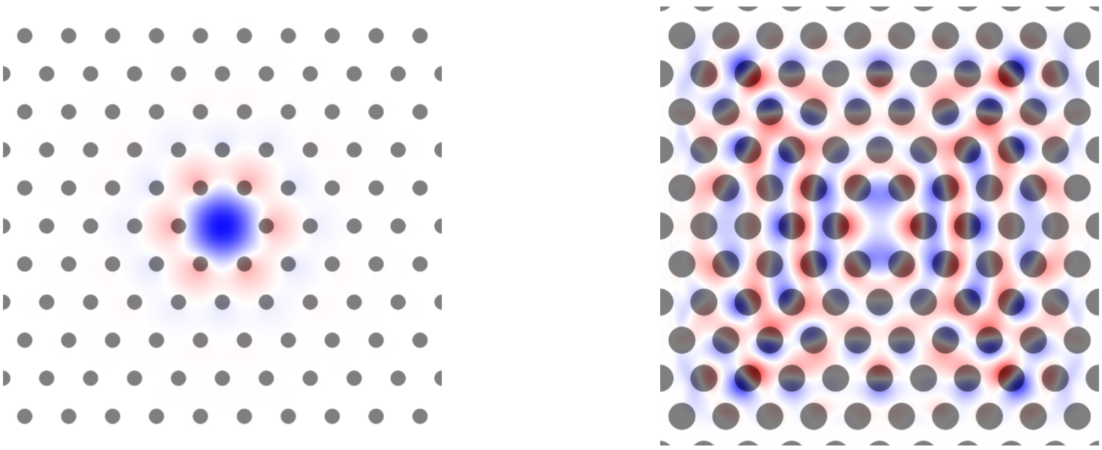

(a) Resonance at a fill-factor of 0.19.

(b) Resonance at a fill-factor of 0.32.

Figure 6.7: The field profiles of resonant modes in a photonic defect at high Q fill-factors, simulated using MEEP[87]. The resonance at a fill-factor of 0.19 is the localised fundamental state of the lattice. The resonance at a fill-factor of 0.32 extends across the lattice indicating that it is a state over the extended lattice making it unsuitable for use in a LSW experiment.

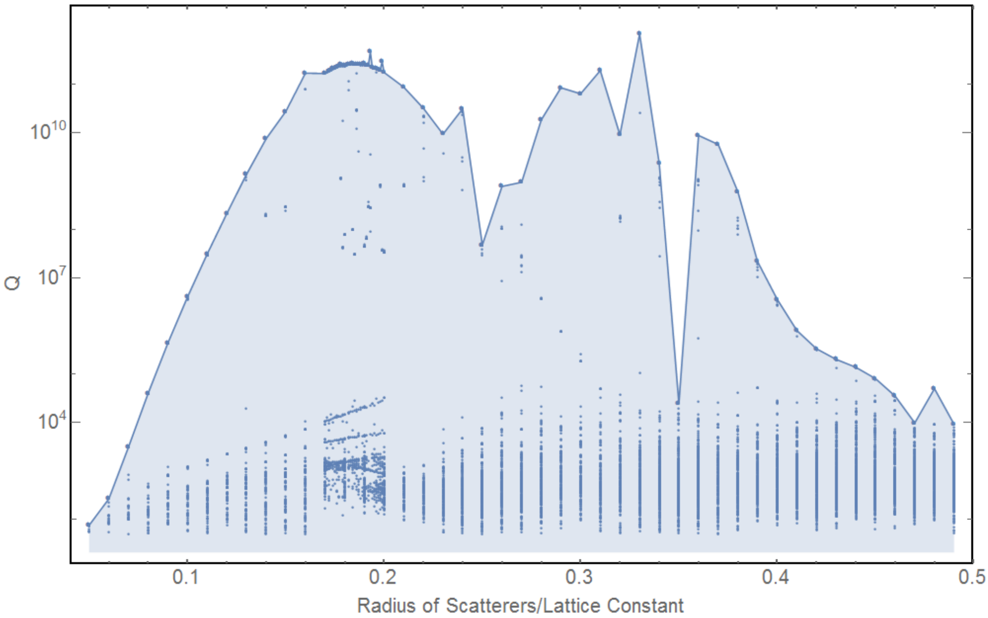

Figure 6.8: The Q-factor for all components are recorded as blue dots and the blue region outlines the maximum Q for each fill-factor, simulated using MEEP[87].

match those of cavities with relatively small structures as demonstrated in Fig 6.9. With a lattice of only 5 scatterers in each direction a Q of 10^5 can be achieved, this is equivalent to copper cavities. By increasing the size of the lattice further Q-factors equivalent to those of superconducting cavities, 10^{10}, can be met. At these high Q-factors, the dielectric losses become an important factor and therefore only materials with extremely low loss tangents of order 10^{-7} are suitable[88][89].

6.4 Experimental Design

To successfully conduct a LSW experiment, hig- Q cavities are not all that is needed as a radio-quiet environment for the detector is also required. This is because the signal which would be produced through HSP interactions is small enough to be hidden within the uncertainties of the background noise of the de-

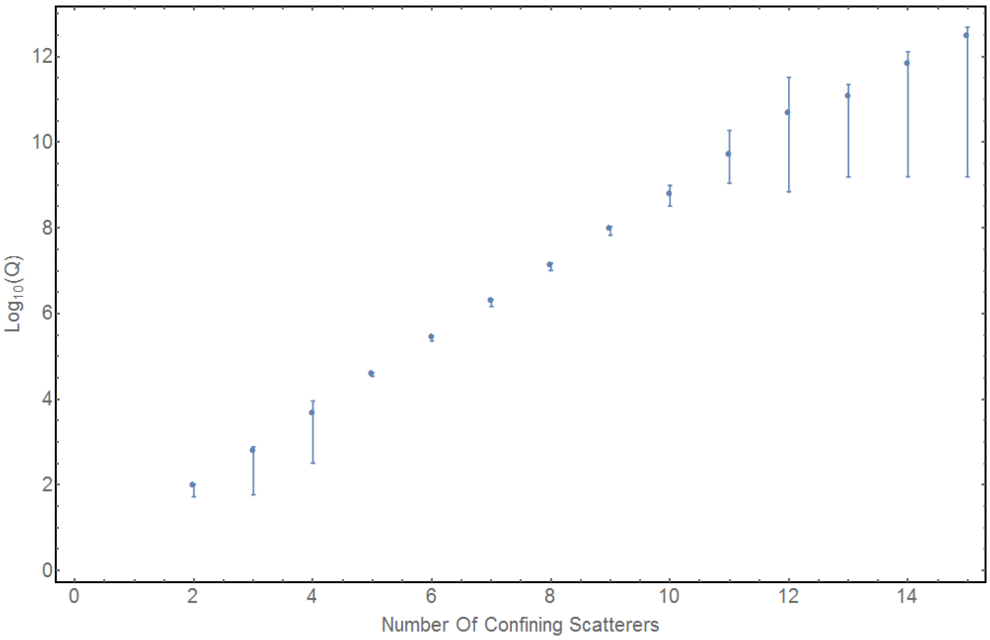

Figure 6.9: The maximum achievable Q-factor for a defect surrounded by an increasing the number of scatterers along the lattice vectors that makes up the lattice, simulated using MEEP[87]. The resolution of the underlying simulation was varied to produce systematic uncertainties for the simulations.

tector. In this regard photonic cavities have a natural advantage over traditional cavities as the expected signal frequency is within the bandgap of the lattice and therefore simply by extending the lattice further, more shielding is added. This feature allows the defect to be easily shielded from external sources but also from one another as two closely-located defects can create a coupled system allowing energy transmission between the two. To counteract this the two defects can be moved further apart and the intermediate lattice acts as shielding between the defects allowing a LSW experiment to be constructed entirely within a photonic crystal. Fig 6.10 shows how such a set-up would look with defects placed so they couple in Fig 6.10a and decoupled in Fig 6.10b.

When considering a realisable structure, propagation outside of the plane must be considered. To analyse this the defect was approximated to be a cylindrical wave-guide with a radius equal to the lattice constant. This means that the state decays evanescently in the 'z' direction leading to a smaller high-field volume for a photonic cavity than for that of a conventional cavity. This restriction on the volume of the cavity caused a significant reduction in the geometric-factor for the experiment. While still maintaining sufficient separation to ensure isolation, the defects can be separated by smaller distances than would be expected for conventional cavities which gave a compensatory increase in the geometric-factor. By taking into account the limited size of the defect and the smaller distance required for isolation, the geometric-factor is expected to be of order 10^{-3} rather than that of order 1 for microwave cavities.

A single photonic crystal can contain many defects, opening up the possibility of having multiple sources and detectors. By maintaining sufficient lattice spacings between the defects, they can all be considered as independent defects.

The use of multiple powered defects increases the flux of HSPs without increasing the power within or quality-factors of the defects, overcoming some of the physical limitations of the defects. In the most simple case, exploiting the lattices' symmetries, 6 powered defects can be used to provide signal to a single detector defect however more complicated arrangements are possible. [1]

6.5 Potential Reach

So far in this chapter a has been left as a free parameter. To set a potential exclusion the lattice constant needed to be set so that the resonance corresponded to the desired physical frequency. Since MEEP uses natural units the frequency is given by

$$F = \frac{\mathcal{F}c}{a}, \tag{6.1}$$

where F is the real world frequency and $\mathcal{F}$ is the frequency in natural MEEP units. Once the appropriate lattice constant had been found Eq 4.33 was used to estimate the sensitivity of the experiment. Taking the 10-100 GHz range which conventional microwave cavities struggle with Fig 6.12 shows the expected exclusion.

The parameters were chosen based on practical considerations. The Q was set to 10^8 as Fig 6.9 shows this can be achieved with less than 10 confining scatterers and therefore having 30 between the defects allows for some loss due to misplacement of, or defects within, the scatterers. The run time was set to a year, the

[1] Having multiple defects opens up the possibility of using interference effects to maximise the signal to noise ratio in the detector defect but initial investigations drew no clear conclusions.

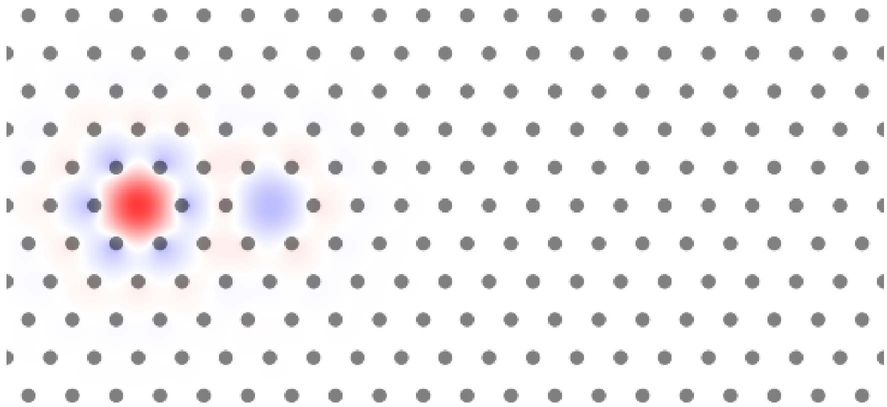

(a) Two closely-positioned defects

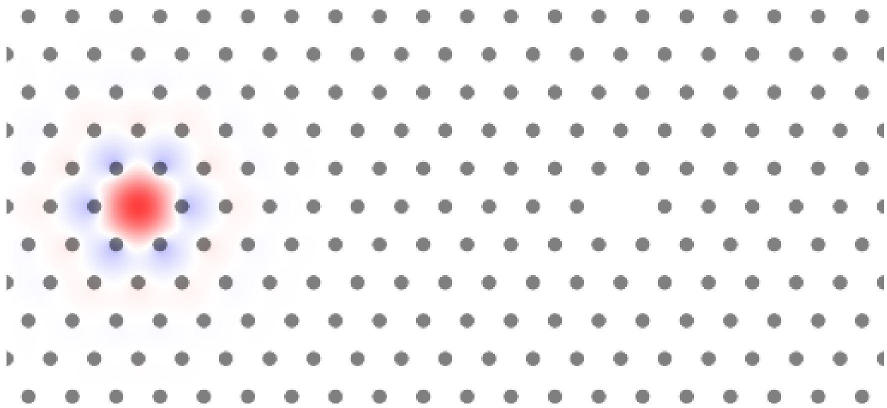

(b) Two well-separated defects

Figure 6.10: The field profile for two coupled and two decoupled defects in a triangular-based photonic lattice. In both cases the left defect was powered and the simulation was allowed to run for 50 oscillations of the field to ensure the field had time to propagate across the lattice, simulated using MEEP[87]. In the coupled case it is easy to see that although attenuated, there has been energy transmission between the defects. In the decoupled case it can be seen that a separation of 10 scatterers is sufficient to prevent any noticeable energy transmission on this energy scale.

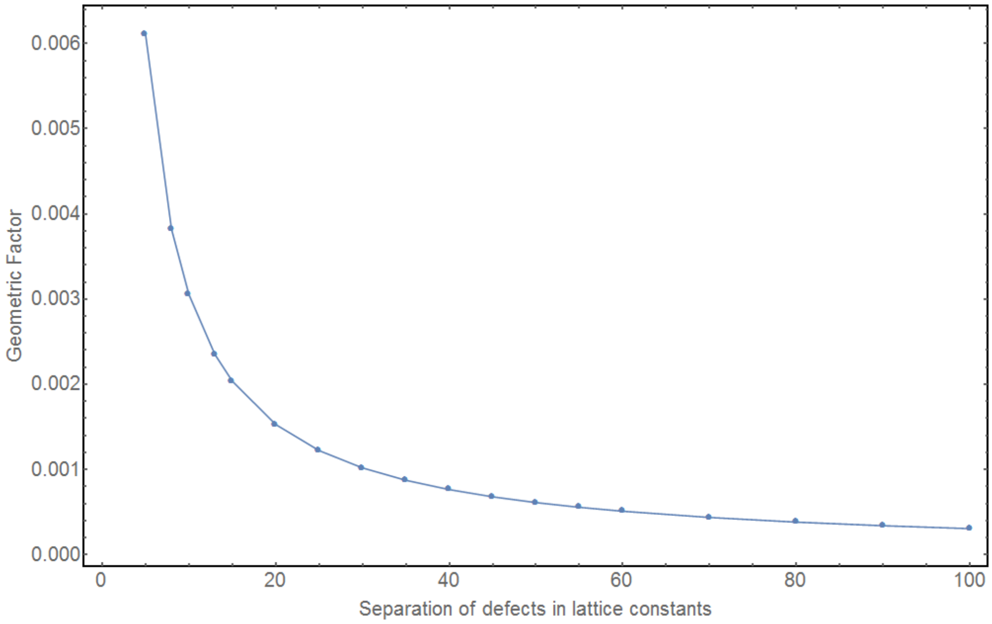

Figure 6.11: The G-factor of a two-defect lattice at 10 GHz with respect to increasing the number of scatterers between the defects.

significance level of exclusion to 3, the temperatures were set to 77 K, the power in the source defects to 1 kW, the amplification to 20 dB and the bandwidth to 1 Hz. The geometric-factor G required more care as this changes as the frequency changes. Fig 6.11 shows the exponential decay of the geometric-factor of a two-defect lattice as the separation between the defects increases. Fitting the data finds the relation

$$G = 0.000434878 + \frac{0.329949}{\mathcal{S}^2}, \tag{6.2}$$

where $\mathcal{S}$ is the integer number of lattice constants between the defects. To ensure isolation of the detector a separation of 30 a was used for the estimation. The total geometric-factor can be increased by using multiple defects as discussed at the end of Section 6.4. It was estimated that this would increase the geometric-

1504 factor by a factor of 6.

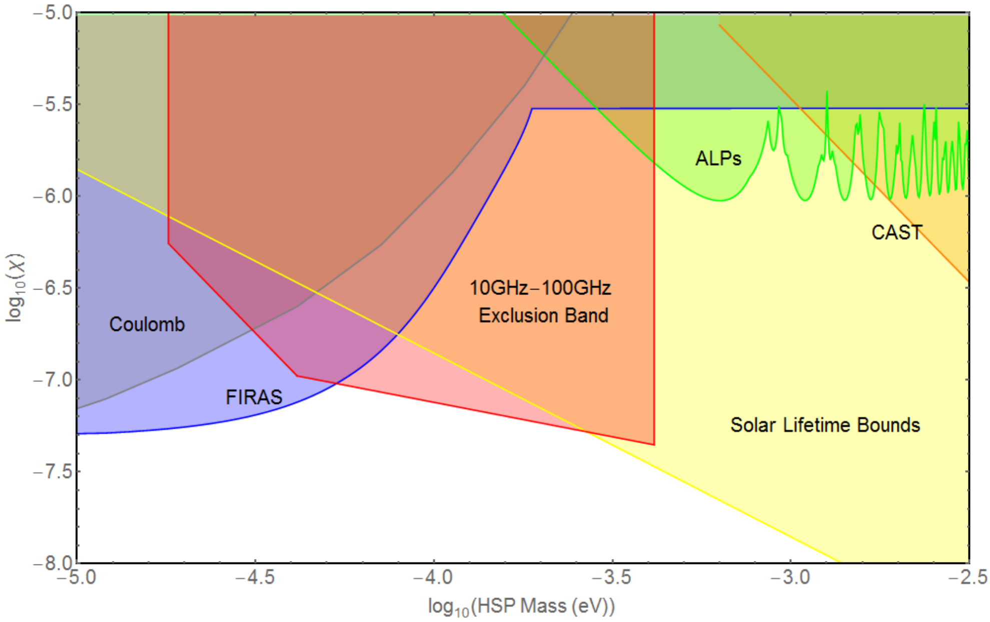

Figure 6.12: The expected exclusion produced by a photonic lattice based LSW experiment in the 10-100 GHz frequency range shown in the black dashed line. The greyed out areas in the background are associated with existing exclusions; FIRAS is Far Infra-Red Astronomy, Coulomb is from fundamental tests of the coulomb force, LSW is from optical LSW experiments, CAST is from the Cern Axion Solar Telescope and Lifetime Bounds is from the effect of HSP's on the lifetime of stars.

Chapter 7

Conclusion

The SM has been a great success of modern particle physics but it has been shown that despite the successes it still needs additions to make the theory match with the full range of observations. In Chapter 2 it was shown how the addition of extra fields associated with WISPs can solve problems such as the strong CP problem and provide compelling candidates for dark matter. Both axions and HSPs have couplings with the SM photon, providing an avenue to search for them experimentally.

In Chapter 4 it was shown that through the use of RF technology it was possible to construct experiments that had the potential to discover HSPs with masses between 1 μeV and 1 meV. By using well-understood copper microwave cavities and off-the-shelf parts it was possible to exclude HSP parameter space between $10^{-5.42}$ and $10^{-5.27}$ eV with a peak exclusion of $\chi = 10^{-7.75}$ utilising the transverse coupling of the CASCADE experiment. In addition to the transverse coupling, CASCADE was the first LSW experiment to make use of the longitudinal mode of the HSP which increased the excluded region to $10^{-5.60}$ and $10^{-5.27}$ eV with a peak exclusion of $\chi = 10^{-7.8}$. This was competitive with that which was achieved by the CROWs experiment which had a peak exclusion of 10^{-9} but benefited from both higher Q-factors and a higher power emitter. In future phases of the CASCADE experiment the use of superconducting cavities for the emitter would improve the sensitivity by several orders of magnitude. In addition running a cryogenic detector cavity and amplifier would improve performance further.

The PHARAOH experiment takes advantage of recent advances in the understanding of how dielectric lattices interact with EM fields to create a new way of producing a LSW experiment. This new experimental set-up would allow the probing of mass ranges between $10^{-4.47}$ and $10^{-3.38}$ eV with exclusions that are competitive with those set experimentally in different mass ranges, effectively bridging the gap between RF and optical frequency experiments. A proof of principle experiment based on PHARAOH using relatively inexpensive materials such as glass would have the potential to not only show the use of photonic structures in LSW experiments but also to exclude new regions of the HSP parameter space.

Appendix A

Resistive Cavity Losses

The resistive power loss of an EM field with a magnetic field **H**, oscillating in a cavity of length l, can be calculated by,

$$P_{\text{loss}} = \frac{1}{2\sigma\delta}\left[\oint_C dl \int_0^d dz|\mathbf{n}\times\mathbf{H}|^2_{\text{sides}} + 2\int_A da|\mathbf{n}\times\mathbf{H}|^2_{\text{ends}}\right], \tag{A.1}$$

where σ is the conductivity, C is the circumference of the cavity, A is the cross-sectional area of the cavity, $\mathbf{n}$ is the unit normal to the surface and δ is the skin depth that is given by

$$\delta = \sqrt{\frac{2}{\mu_c\omega\sigma}}, \tag{A.2}$$

where μ and μ_c are the permittivity of the void and the cavity walls respectively. It can then be shown that

$$P_{\text{loss}} = \frac{\epsilon}{\sigma\delta\mu}\left[1+\left(\frac{p\pi}{\gamma_\lambda d}\right)^2\right]\left(1+\xi_\lambda\frac{Cd}{4A}\right)\int_A |\psi|^2 da \tag{A.3}$$

for TM modes where $p \neq 0$, ξ_λ is a dimensionless parameter of order unity that encodes the cross-sectional geometry of the cavity. For modes where $p = 0$, ξ just gets changed to 2ξ. Substituting Eq A.3, Eq 3.30 and Eq A.2 into the definition of Q, Eq 3.23, gives

$$Q = \frac{\mu}{\mu_c}\frac{d}{\delta}\frac{1}{2\left(1 + \xi_\lambda \frac{Cd}{4A}\right)} \tag{A.4}$$

For $p = 0$ TM modes, the whole solution needs to be multiplied by 2 and ξ becomes 2ξ.

Appendix B

Photographs Of CASCADE Phase 1

Figure B.1: Photograph of the signal generator used in the CASCADE experiment.

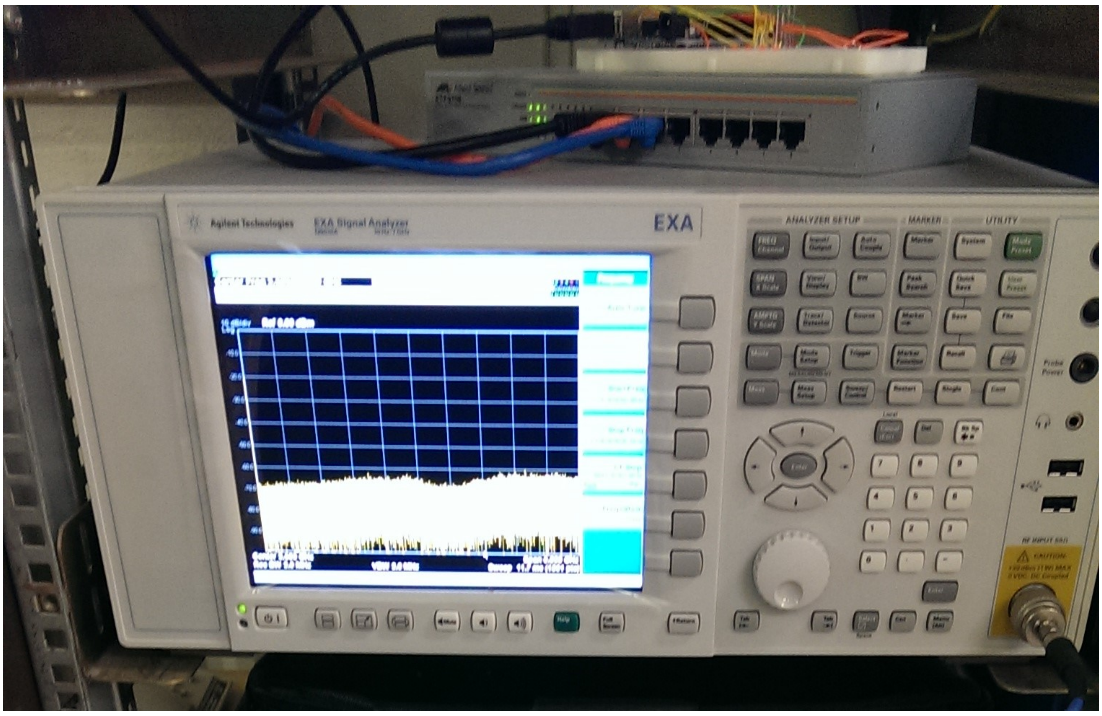

Figure B.2: Photograph of the signal analyser used in the CASCADE experiment.

Figure B.3: Photograph of the cavity shielding boxes used in the CASCADE experiment.

Figure B.4: Photograph of the interior of the cavity shielding boxes used in the CASCADE experiment.

Figure B.5: Photograph of the Faraday cage housing the emitter of the CASCADE experiment.

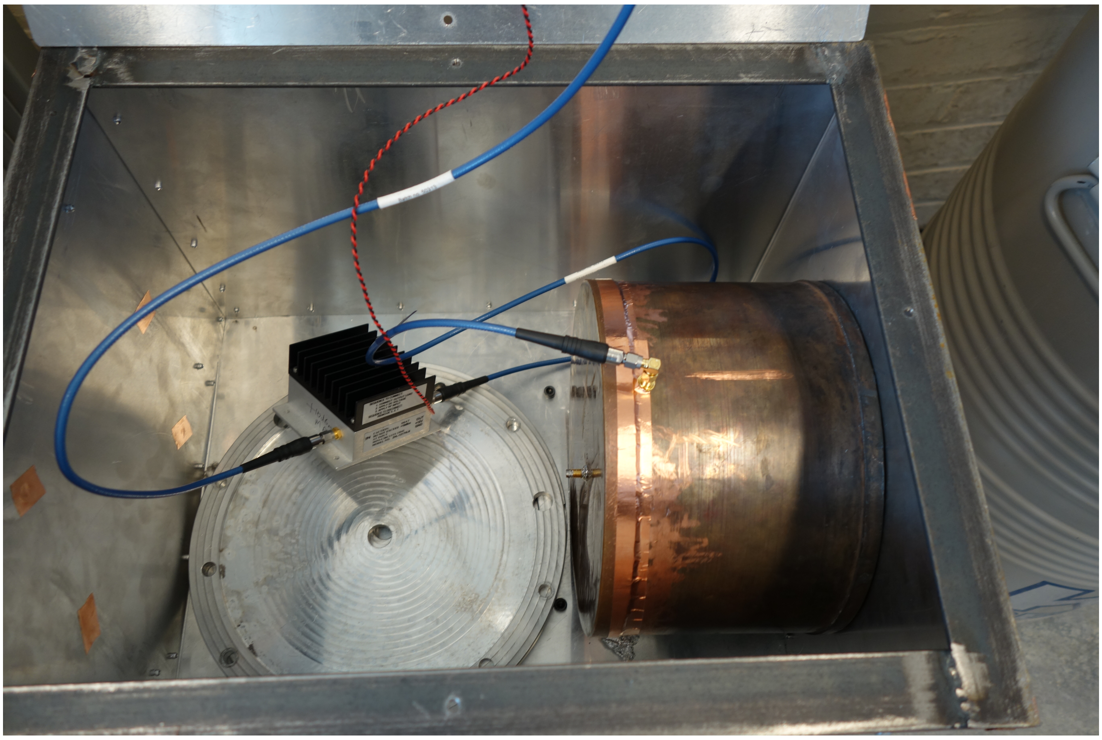

Figure B.6: Photograph of the inside of the emitter Faraday cage used in the CASCADE experiment.

Figure B.7: Photograph of the detector side of the CASCADE experiment.

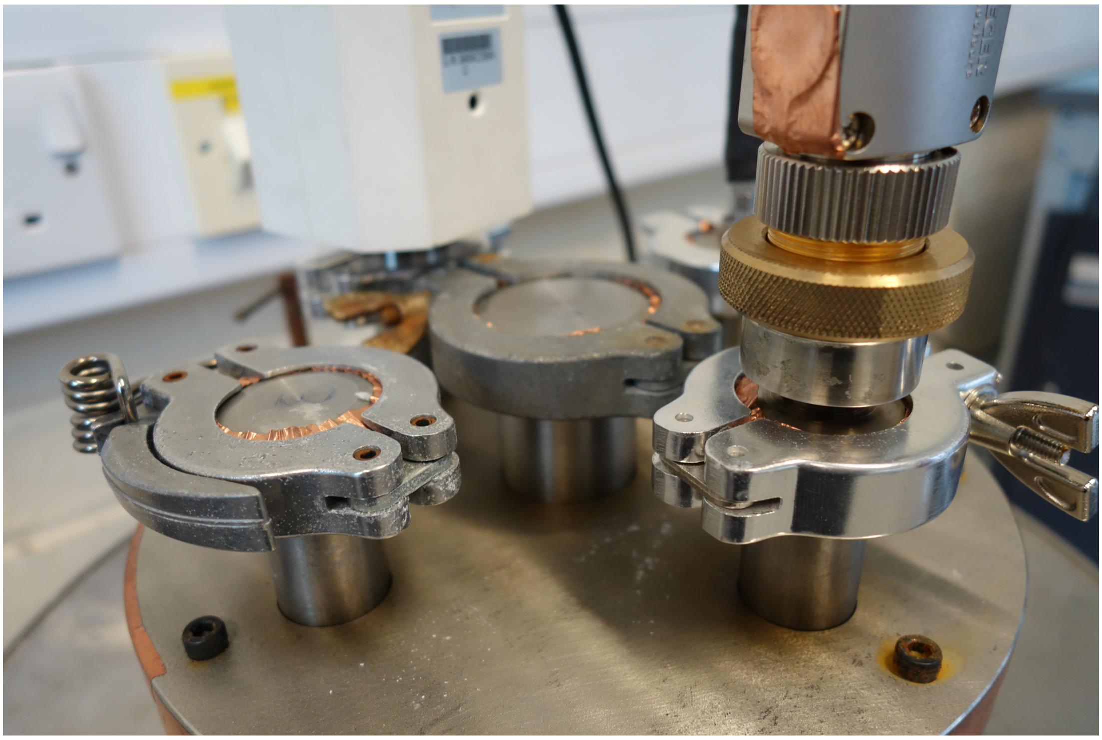

Figure B.8: Photograph of the vacuum box feed-throughs and instrumentation from the CASCADE experiment.

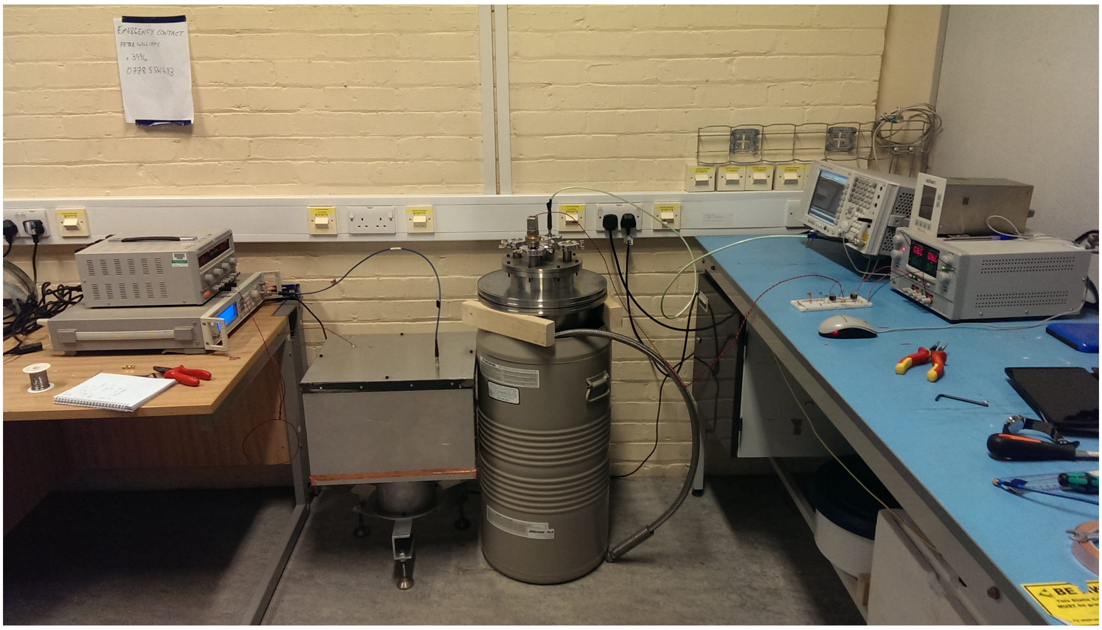

Figure B.9: Photograph of the full CASCADE experiment.

Appendix C

CASCADE Cryogenic Measurements

The original conception of CASCADE was as a multi-phase experiment. The work which is presented inside this thesis is concerned with the first phase which was envisaged as a proof-of-principle experiment. The primary objective was to show that off-the-shelf components can be used at room and liquid nitrogen temperatures to produce a LSW experiment which is sensitive to new HSP parameter space. The room temperature measurement was described in Chapter 5; the low temperature measurement experienced some complications but since it comprised a significant amount of work it will be discussed in this appendix.

The cooling of the detector of the experiment will have effects on several of the components. The cavity will have an increased Q-factor as cooling the metal increases its conductivity, allowing the electrons to move more easily to oppose the electric field inside the cavity. The amplifiers are designed to operate at low temperature and benefit from increased amplification and reduced electrical noise.

To test the increase in the Q-factor of the cavity, it was submerged in liquid nitrogen and allowed to cool until the resonant frequency was stable. The cavity was then probed with the S11 measurement from a network analyser and the Q was found to be 13000.

The amplifiers were also tested at low temperature and the results are shown in Fig C.1. As expected the amplifiers showed improved performance with an increase from 39 dB to 41 dB each.

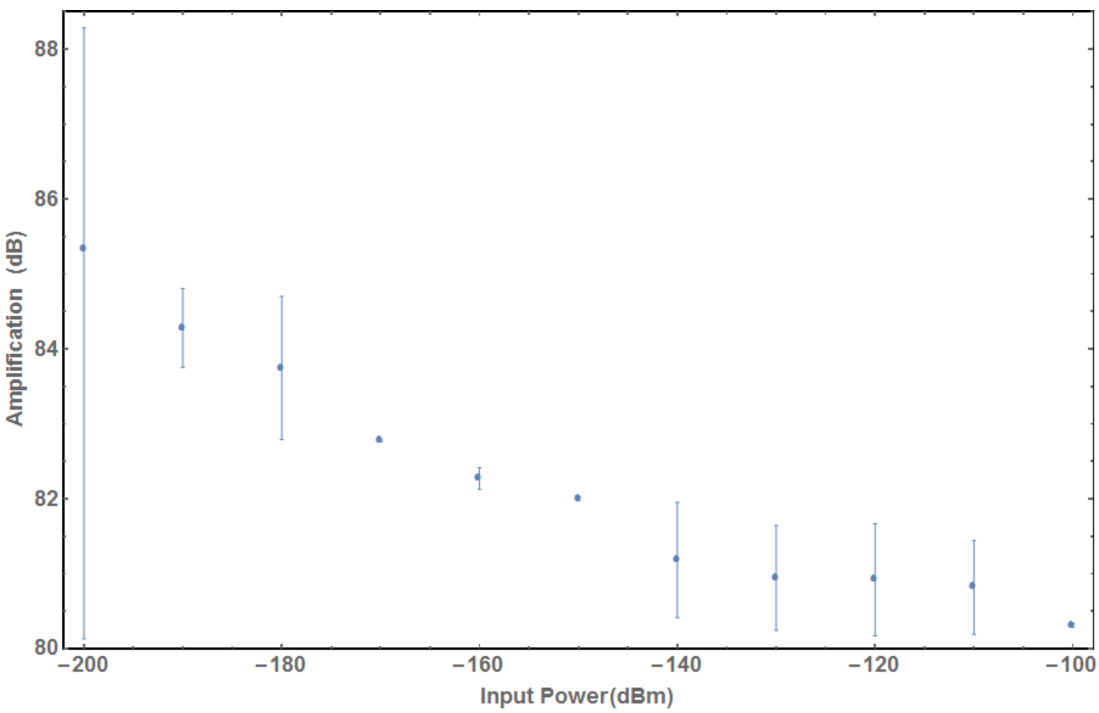

Figure C.1: Amplification with varying input power for the detector side amplifiers used in the CASCADE experiment at 77 K. The error bars show the full range of results from multiple measurements.

Since the detector was housed in a vacuum box, the detector was put under a weak vacuum to minimise the risk of liquid gasses affecting the results. The vacuum flange had been custom made but it lacked a groove to correctly seat a silicon seal. This meant that gas would slowly leach into the chamber over time. To ensure that the vacuum would last long enough for measurements to be performed, the vacuum chamber was pumped down and then monitored for 165 hours. The results can be seen in Fig C.2.

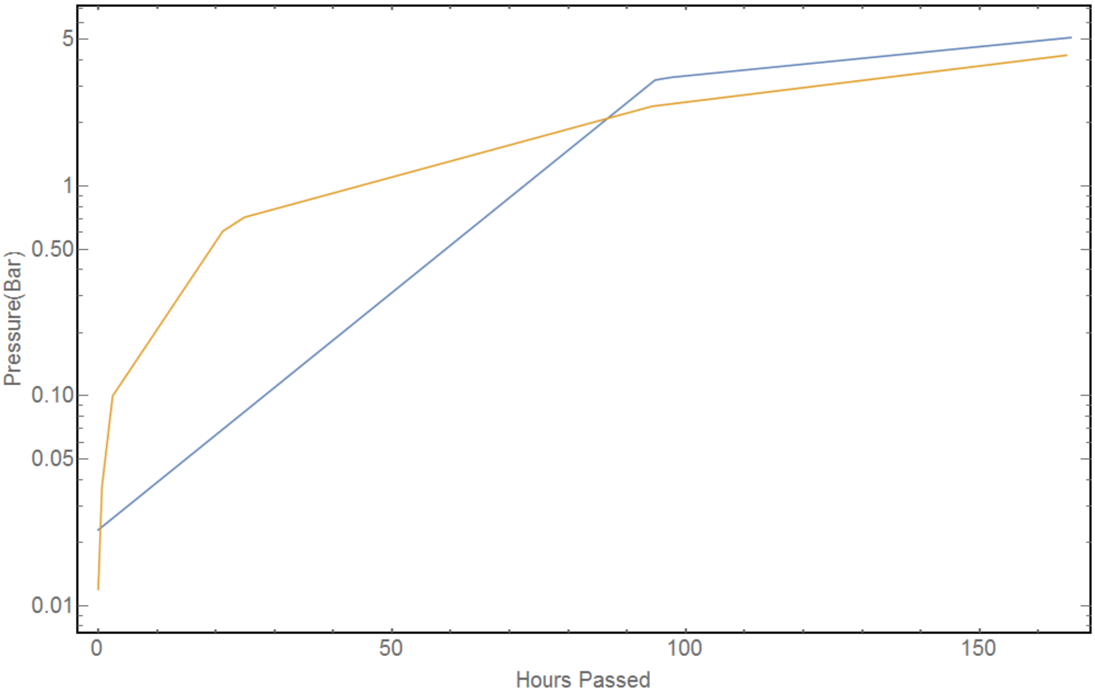

Figure C.2: Pressure inside the vacuum chamber of the CASCADE experiment. The lines show the results from two separate pump down and observation cycles.

On 22/04/2015 the detector was cooled down. It was anticipated that this would lead to a decrease in the thermal noise of the system in addition to an increase in the Q value. During the cool-down process an audible 'bang' was heard and once the set-up was cooled and the cavities were calibrated for the initial measurement, the EXA showed the signal from the emitter. Since the equipment was cool it wasn't possible to make any adjustments to the detector to eliminate the signal, so the resolution bandwidth of the signal analyser was increased from 0.5 mHz to 1 mHz so that the peak was indistinguishable from the noise. Having increased the noise in the measurement, this meant that no meaningful exclusion could be made.

After the experiment had been allowed to warm up, the experiment was deconstructed. When the cavity was inspected the cause of both the noise and the signal was found. The cavity shielding box had popped open and the lid had a visible bend to it as can be seen in Fig C.3. The reason for the rupture of the shielding box was thought to be caused by a pressure differential between the vacuum chamber and the shielding box. On closer inspection it was also found that the opening of the lid had also caused the shielding-box feed-through and one of the co-axial cables to break as can be seen in Fig C.4. Due to these reasons, a cryogenic measurement was not possible in phase 1 of the CASCADE experiment, however with a stronger shielding box measurements should be possible in future phases.

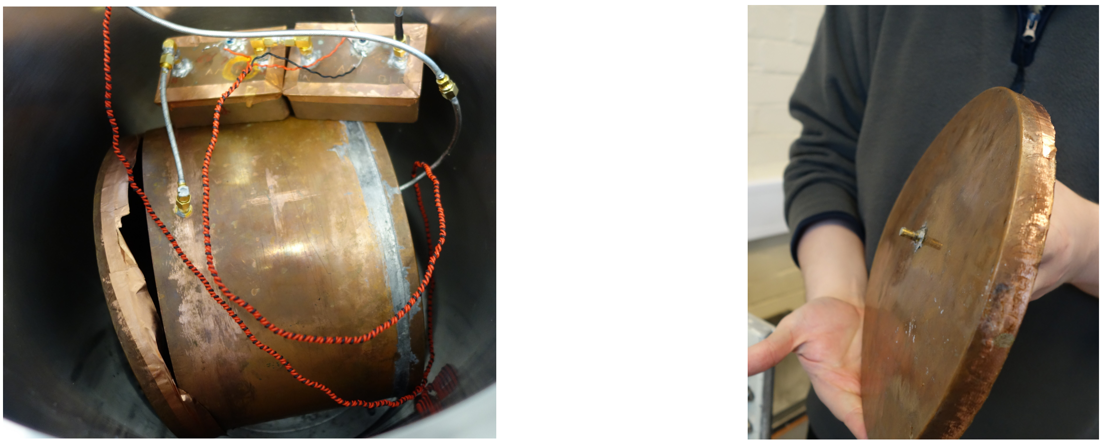

Figure C.3: *Left*: The shielding box as found after the cryogenic run. The lid has clearly come away from the body of the box and is therefore ineffective.
Right: A close up of the lid. It can be be seen that the lid has been bent.

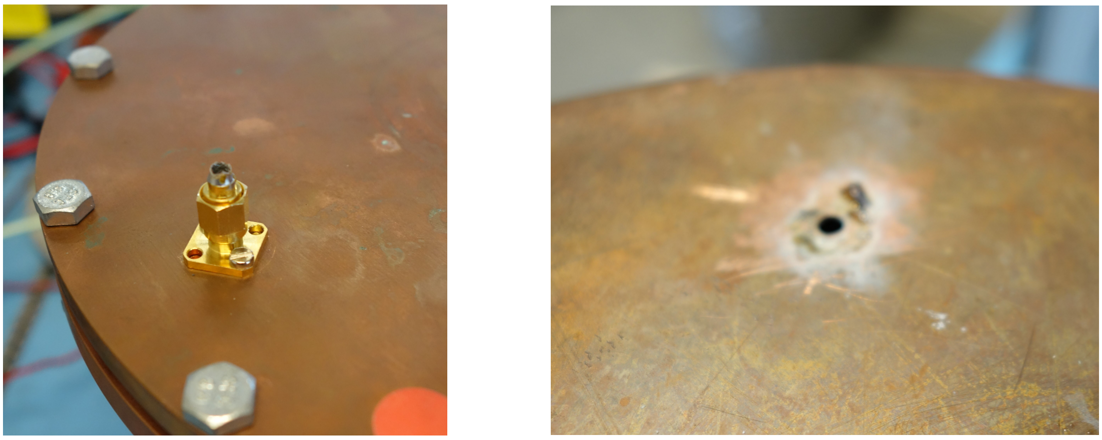

Figure C.4: *Left*: After the CASCADE cryogenic run the second cavity port was found to have snapped at the SMA connection.
Right: After the CASCADE cryogenic run the soldering for the shielding box feed-through for the second port had separated from the copper.

References

[1] Serguei Chatrchyan et al. Observation of a new boson at a mass of 125 GeV with the CMS experiment at the LHC. *Phys. Lett.*, B716:30–61, 2012. 1, 6

[2] Georges Aad et al. Observation of a new particle in the search for the Standard Model Higgs boson with the ATLAS detector at the LHC. *Phys. Lett.*, B716:1–29, 2012. 1, 6

[3] R. D. Peccei and Helen R. Quinn. CP Conservation in the Presence of Instantons. *Phys. Rev. Lett.*, 38:1440–1443, 1977. 1, 12

[4] Steven Weinberg. A New Light Boson? *Phys. Rev. Lett.*, 40:223–226, 1978. 1

[5] Frank Wilczek. Problem of Strong p and t Invariance in the Presence of Instantons. *Phys. Rev. Lett.*, 40:279–282, 1978. 1

[6] Murray Gell-Mann. A Schematic Model of Baryons and Mesons. *Phys. Lett.*, 8:214–215, 1964. 5

[7] G. Zweig. An SU(3) model for strong interaction symmetry and its breaking. Version 2. Technical report, 1964. 5

[8] F. Englert and R. Brout. Broken Symmetry and the Mass of Gauge Vector Mesons. *Phys. Rev. Lett.*, 13:321–323, 1964. 5

[9] G. S. Guralnik, C. R. Hagen, and T. W. B. Kibble. Global Conservation Laws and Massless Particles. *Phys. Rev. Lett.*, 13:585–587, 1964. 5

[10] Peter W. Higgs. Broken Symmetries and the Masses of Gauge Bosons. *Phys. Rev. Lett.*, 13:508–509, 1964. 5

[11] S. L. Glashow, J. Iliopoulos, and L. Maiani. Weak Interactions with Lepton-Hadron Symmetry. *Phys. Rev.*, D2:1285–1292, 1970. 5

[12] Makoto Kobayashi and Toshihide Maskawa. CP Violation in the Renormalizable Theory of Weak Interaction. *Prog. Theor. Phys.*, 49:652–657, 1973. 5

[13] Martin Breidenbach, Jerome I. Friedman, Henry W. Kendall, Elliott D. Bloom, D. H. Coward, H. C. DeStaebler, J. Drees, Luke W. Mo, and Richard E. Taylor. Observed Behavior of Highly Inelastic electron-Proton Scattering. *Phys. Rev. Lett.*, 23:935–939, 1969. 5

[14] Elliott D. Bloom et al. High-Energy Inelastic e p Scattering at 6-Degrees and 10-Degrees. *Phys. Rev. Lett.*, 23:930–934, 1969. 5

[15] J. E. Augustin et al. Discovery of a Narrow Resonance in e+ e- Annihilation. *Phys. Rev. Lett.*, 33:1406–1408, 1974. [Adv. Exp. Phys.5,141(1976)]. 5

[16] J. J. Aubert et al. Experimental Observation of a Heavy Particle J. *Phys. Rev. Lett.*, 33:1404–1406, 1974. 5

[17] S. W. Herb et al. Observation of a Dimuon Resonance at 9.5-GeV in 400-GeV Proton-Nucleus Collisions. *Phys. Rev. Lett.*, 39:252–255, 1977. 5

[18] F. Abe et al. Observation of top quark production in $\bar{p}p$ collisions. *Phys. Rev. Lett.*, 74:2626–2631, 1995. 5

[19] S. Abachi et al. Search for high mass top quark production in $p\bar{p}$ collisions at $\sqrt{s} = 1.8$ TeV. *Phys. Rev. Lett.*, 74:2422–2426, 1995. 5

[20] D. P. Barber et al. Discovery of Three Jet Events and a Test of Quantum Chromodynamics at PETRA Energies. *Phys. Rev. Lett.*, 43:830, 1979. 5

[21] G. Arnison et al. Experimental Observation of Isolated Large Transverse Energy Electrons with Associated Missing Energy at s**(1/2) = 540-GeV. *Phys. Lett.*, B122:103–116, 1983. [,611(1983)]. 5

[22] G. Arnison et al. Experimental Observation of Lepton Pairs of Invariant Mass Around 95-GeV/c**2 at the CERN SPS Collider. *Phys. Lett.*, B126:398–410, 1983. 5

[23] Wikimedia Commons. Standard model of elementary particles, 2014. 6

[24] K. A. Olive et al. Review of Particle Physics. *Chin. Phys.*, C38:090001, 2014. 8, 10, 14, 15, 18

[25] P. A. R. Ade et al. Planck 2015 results. XIII. Cosmological parameters. 2015. 8

[26] Riccardo Catena and Piero Ullio. A novel determination of the local dark matter density. *JCAP*, 1008:004, 2010. 8, 11

[27] Gianfranco Bertone, Dan Hooper, and Joseph Silk. Particle dark matter: Evidence, candidates and constraints. *Phys. Rept.*, 405:279–390, 2005. 8

[28] A. D. Sakharov. Violation of CP Invariance, c Asymmetry, and Baryon Asymmetry of the Universe. *Pisma Zh. Eksp. Teor. Fiz.*, 5:32–35, 1967. [Usp. Fiz. Nauk161,61(1991)]. 9

[29] V. A. Rubakov and M. E. Shaposhnikov. Electroweak baryon number non-conservation in the early universe and in high-energy collisions. *Usp. Fiz. Nauk*, 166:493–537, 1996. [Phys. Usp.39,461(1996)]. 9

[30] Gerard 't Hooft. Symmetry Breaking Through Bell-Jackiw Anomalies. *Phys. Rev. Lett.*, 37:8–11, 1976. 9

[31] C. S. Wu, E. Ambler, R. W. Hayward, D. D. Hoppes, and R. P. Hudson. Experimental Test of Parity Conservation in Beta Decay. *Phys. Rev.*, 105:1413–1414, 1957. 9

[32] Makoto Kobayashi and Toshihide Maskawa. CP Violation in the Renormalizable Theory of Weak Interaction. *Prog. Theor. Phys.*, 49:652–657, 1973. 9

[33] Laurent Canetti, Marco Drewes, and Mikhail Shaposhnikov. Matter and Antimatter in the Universe. *New J. Phys.*, 14:095012, 2012. 9

[34] C. A. Baker et al. An Improved experimental limit on the electric dipole moment of the neutron. *Phys. Rev. Lett.*, 97:131801, 2006. 10, 13

[35] Maxim Pospelov and Adam Ritz. Electric dipole moments as probes of new physics. *Annals Phys.*, 318:119–169, 2005. 10

[36] S. Schael et al. Precision electroweak measurements on the Z resonance. *Phys. Rept.*, 427:257–454, 2006. 10

[37] Beranger Dumont, Genevieve Belanger, Sylvain Fichet, Sabine Kraml, and Thomas Schwetz. Mixed sneutrino dark matter in light of the 2011 XENON and LHC results. *JCAP*, 1209:013, 2012. 10

[38] M. Yamashita, T. Doke, J. Kikuchi, and S. Suzuki. Double phase (liquid / gas) xenon scintillation detector for WIMPs direct search. *Astropart. Phys.*, 20:79–84, 2003. 11

[39] D. S. Akerib et al. Exclusion limits on the WIMP-nucleon cross section from the first run of the Cryogenic Dark Matter Search in the Soudan Underground Laboratory. *Phys. Rev.*, D72:052009, 2005. 11

[40] Julien Lavalle and Stefano Magni. Making sense of the local Galactic escape speed estimates in direct dark matter searches. *Phys. Rev.*, D91(2):023510, 2015. 11

[41] John R. Ellis, Keith A. Olive, and Christopher Savage. Hadronic Uncertainties in the Elastic Scattering of Supersymmetric Dark Matter. *Phys. Rev.*, D77:065026, 2008. 11

[42] Joerg Jaeckel and Michael Spannowsky. Probing MeV to 90 GeV axion-like particles with LEP and LHC. *Phys. Lett.*, B753:482–487, 2016. 12

[43] R. J. Crewther, P. Di Vecchia, G. Veneziano, and Edward Witten. Chiral Estimate of the Electric Dipole Moment of the Neutron in Quantum Chromo-

dynamics. *Phys. Lett.*, B88:123, 1979. [Erratum: Phys. Lett.B91,487(1980)]. 13

[44] Mikhail A. Shifman, A. I. Vainshtein, and Valentin I. Zakharov. Can Confinement Ensure Natural CP Invariance of Strong Interactions? *Nucl. Phys.*, B166:493–506, 1980. 14

[45] Michael Dine, Willy Fischler, and Mark Srednicki. A Simple Solution to the Strong CP Problem with a Harmless Axion. *Phys. Lett.*, B104:199–202, 1981. 14

[46] Frank Wilczek. Axions and Family Symmetry Breaking. *Phys. Rev. Lett.*, 49:1549–1552, 1982. 14

[47] Y. Chikashige, Rabindra N. Mohapatra, and R. D. Peccei. Are There Real Goldstone Bosons Associated with Broken Lepton Number? *Phys. Lett.*, B98:265–268, 1981. 14

[48] Joerg Jaeckel and Andreas Ringwald. The Low-Energy Frontier of Particle Physics. *Ann. Rev. Nucl. Part. Sci.*, 60:405–437, 2010. 15, 16

[49] Daniel Feldman, Zuowei Liu, and Pran Nath. The Stueckelberg Z-prime Extension with Kinetic Mixing and Milli-Charged Dark Matter From the Hidden Sector. *Phys. Rev.*, D75:115001, 2007. 16

[50] R. R. Caldwell, Rahul Dave, and Paul J. Steinhardt. Cosmological imprint of an energy component with general equation of state. *Phys. Rev. Lett.*, 80:1582–1585, 1998. 16

[51] Jason H. Steffen, Amol Upadhye, Al Baumbaugh, Aaron S. Chou, Peter O. Mazur, Ray Tomlin, Amanda Weltman, and William Wester. Laboratory constraints on chameleon dark energy and power-law fields. *Phys. Rev. Lett.*, 105:261803, 2010. 16

[52] Justin Khoury and Amanda Weltman. Chameleon cosmology. *Phys. Rev.*, D69:044026, 2004. 17

[53] M. Ahlers, H. Gies, J. Jaeckel, J. Redondo, and A. Ringwald. Light from the hidden sector. *Phys. Rev.*, D76:115005, 2007. 17, 56, 57

[54] Joerg Jaeckel. Probing Minicharged Particles with Tests of Coulomb's Law. *Phys. Rev. Lett.*, 103:080402, 2009. 17

[55] Jo Bovy and Scott Tremaine. On the local dark matter density. *Astrophys. J.*, 756:89, 2012. 18

[56] J. Hoskins et al. A search for non-virialized axionic dark matter. *Phys. Rev.*, D84:121302, 2011. 19

[57] ADMX RF Cavity. `http://depts.washington.edu/admx/cavity.shtml`. Accessed: 2016-02-29. 19

[58] Stephen J. Asztalos et al. Experimental constraints on the axion dark matter halo density. *Astrophys. J.*, 571:L27–L30, 2002. 19

[59] Darko Veberic et al. Search for dark matter in the hidden-photon sector with a large spherical mirror. *PoS*, ICRC2015:1191, 2015. 19

[60] T. Mizumoto et al. Experimental search for solar hidden photons in the eV energy range using kinetic mixing with photons. *JCAP*, 1307:013, 2013. 19

[61] J. Ruz, J. K. Vogel, and M. J. Pivovaroff. Recent Constraints on Axion-photon and Axion-electron Coupling with the CAST Experiment. *Phys. Procedia*, 61:153–156, 2015. 19

[62] E. Armengaud et al. Conceptual Design of the International Axion Observatory (IAXO). *JINST*, 9:T05002, 2014. 19

[63] Robin Bhre et al. Any light particle search II Technical Design Report. *JINST*, 8:T09001, 2013. 20

[64] M. Betz, F. Caspers, M. Gasior, M. Thumm, and S. W. Rieger. First results of the CERN Resonant Weakly Interacting sub-eV Particle Search (CROWS). *Phys. Rev.*, D88(7):075014, 2013. 20, 58

[65] Stephen R. Parker, John G. Hartnett, Rhys G. Povey, and Michael E. Tobar. Cryogenic resonant microwave cavity searches for hidden sector photons. *Phys. Rev.*, D88:112004, 2013. 20

[66] A. J Martin et al. Preliminary results from the Yale microwave cavity experiment. In *Axions, WIMPs and WISPs. Proceedings, 7th Patras Workshop, PATRAS 2011, Mykonos, Greece, June 27-July 1, 2011*, pages 51–55, 2011. 21, 58

[67] John David Jackson. *Classical Electrodynamics*. Wiley, 1998. 22, 24

[68] JD Joannopoulos et al. *Photonic Crystals: Molding the Flow of Light (Second Edition)*. Princeton University Press, 2 edition, 2008. 22, 33, 36, 38, 40, 42, 44, 45, 47, 99

[69] L. B. Okun. LIMITS OF ELECTRODYNAMICS: PARAPHOTONS? *Sov. Phys. JETP*, 56:502, 1982. [Zh. Eksp. Teor. Fiz.83,892(1982)]. 51, 57

[70] P. Sikivie. Experimental Tests of the Invisible Axion. *Phys. Rev. Lett.*, 51:1415–1417, 1983. [Erratum: Phys. Rev. Lett.52,695(1984)]. 51

[71] F. Hoogeveen and T. Ziegenhagen. Production and detection of light bosons using optical resonators. *Nucl. Phys.*, B358:3–26, 1991. 57

[72] Javier Redondo and Georg Raffelt. Solar constraints on hidden photons re-visited. *JCAP*, 1308:034, 2013. 58

[73] Haipeng An, Maxim Pospelov, and Josef Pradler. New stellar constraints on dark photons. *Phys. Lett.*, B725:190–195, 2013. 58

[74] Joerg Jaeckel and Andreas Ringwald. A Cavity Experiment to Search for Hidden Sector Photons. *Phys. Lett.*, B659:509–514, 2008. 60, 61

[75] Peter W. Graham, Jeremy Mardon, Surjeet Rajendran, and Yue Zhao. Parametrically enhanced hidden photon search. *Phys. Rev.*, D90(7):075017, 2014. 65, 67

[76] P Corlett et al. A superconducting rf vertical test facility at daresbury laboratory. *Proc. EPAC08, Genoa*, 2008. 69

[77] John G. Hartnett, Joerg Jaeckel, Rhys G. Povey, and Michael E. Tobar. Resonant regeneration in the sub-quantum regime A demonstration of fractional quantum interference. *Phys. Lett.*, B698:346–352, 2011. 71

[78] RS Components Ltdrs pro straight panel mount sma connector, jack, solder termination. http://docs-europe.electrocomponents.com/webdocs/13e8/0900766b813e88ae.pdf. Accessed: 2016-02-13. 78

[79] MW Hosking et al. The dielectric constant of liquid nitrogen over the frequency range 0.5 to 10.4 ghz. *Superconductor Science and Technology*, 6(7):549, 1993. 80

[80] Agilent Technologiesn9010a exa signal analyser. http://www.keysight.com/en/pdx-x201715-pn-N9010A/exa-signal-analyzer-10-hz-to-44-ghz?nid=-32508.1150246&cc=GB&lc=eng&pm=ov&state=0. Accessed: 2016-02-19. 81

[81] Agilent Technologies89600 vsa software. http://literature.cdn.keysight.com/litweb/pdf/5990-6405EN.pdf?id=2000790. Accessed: 2016-02-19. 81

[82] Miteqafs3 datasheet. https://www.miteq.com/docs/MITEQ-AFS_CR.PDF. Accessed: 2016-02-17. 81

[83] Mini Circuitszhl-1217hln. http://194.75.38.69/pdfs/ZHL-1217HLN.pdf. Accessed: 2016-02-17. 81, 84

[84] Rhodes and Schwarzrf signal generator sm300. https://cdn.rohde-schwarz.com/pws/dl_downloads/dl_common_library/dl_brochures_and_datasheets/pdf_1/SM300_dat_en.pdf. Accessed: 2016-02-29. 84

[85] Arduino. https://www.arduino.cc/. Accessed: 2016-03-07. 87

[86] Steven G. Johnson and J. D. Joannopoulos. Block-iterative frequency-domain methods for maxwell's equations in a planewave basis. *Opt. Express*, 8(3):173–190, 2001. 99, 101, 102, 105

[87] Ardavan F. Oskooi et al. Meep: A flexible free-software package for electromagnetic simulations by the FDTD method. *Computer Physics Communications*, 181(3):687 – 702, 2010. 101, 103, 104, 105, 106, 107, 110

[88] Jerzy Krupka and othersr. Complex permittivity of some ultralow loss dielectric crystals at cryogenic temperatures. *Measurement Science and Technology*, 10(5):387, 1999. 106

[89] Ian Bailey Duncan Lindsay. Investigation into photonic band-gap structures as a lsw experiment for hsp and alp detection. 2015. 106

[90] G. Hinshaw et al. Nine-Year Wilkinson Microwave Anisotropy Probe (WMAP) Observations: Cosmological Parameter Results. *Astrophys. J. Suppl.*, 208:19, 2013.

[91] Douglas Clowe, Marusa Bradac, Anthony H. Gonzalez, Maxim Markevitch, Scott W. Randall, Christine Jones, and Dennis Zaritsky. A direct empirical proof of the existence of dark matter. *Astrophys. J.*, 648:L109–L113, 2006.

[92] J.M. Pendlebury et al. Revised experimental upper limit on the electric dipole moment of the neutron. *Phys. Rev.*, D92(9):092003, 2015.